Lamb wave evaluation of concrete plates

Tofeldt, Oskar

2017

Document Version:
Publisher's PDF, also known as Version of record

Lamb wave evaluation of concrete plates

Oskar Tofeldt

LUND
UNIVERSITY

DOCTORAL DISSERTATION
by due permission of the Faculty of Engineering, Lund University, Sweden.

To be defended at the Faculty of Engineering (LTH),
E-building, room E:B, Ole Römers väg 3, Lund,
on September 28, 2017, at 10.00 a.m.

Faculty opponent
Dr. Odile Abraham
Geophysics and Non Destructive Evaluation Laboratory,
IFSTTAR, The French institute of science and technology for transport,
development and networks.

Organization: LUND UNIVERSITY Faculty of Engineering Division of Engineering Geology Box 118, SE-22100 Lund, Sweden	**Document name:** DOCTORAL THESIS
	Date of issue: 2017-09-01
Author: Oskar Tofeldt	**Sponsoring organizations:** The Development Fund of the Swedish Construction Industry (SBUF) through Peab and The Swedish Radiation Safety Authority (SSM).

Title: Lamb wave evaluation of concrete plates

Abstract:
This thesis is about the application of Lamb waves for non-destructive evaluation of plate-like concrete structures under one-sided access test condition using a portable equipment consisting of an accelerometer and impact hammer. With this type of equipment and based on array signal processing, the impact-echo (IE) method can be extended with measurements of surface waves; this extension allows an evaluation with Lamb waves. For both the conventional impact-echo method as well as evaluations based on Lamb waves, results in the literature report a systematically underestimated plate thickness. This error is investigated and reproduced in a numerical study and further verified in a measurement. A main source of uncertainty is related to the estimation of a longitudinal wave velocity from first arrivals. To reduce this uncertainty, a new approach for estimation of Poisson's ratio is proposed. The new approach is based on the amplitude polarization of the S1-ZGV Lamb mode: a through-thickness representative estimate of Poisson's ratio is thereby obtained leading to an overall improved estimation of the Lamb wave plate parameters.

A new technique based on 2D arrays is also presented. In an example, the technique is used to map (image) the variation of phase velocity for the A0 Lamb mode in the lateral plane of the plate; that is, the technique is in this case used to assess the material and plate thickness homogeneity. Compared to ultrasonic reflection imaging methods, no limitation to a specific set of operating frequencies (transducers) exists since the 2D array technique is based on a full wave field dataset with wide frequency bandwidth. Variation of material properties transversally through the thickness may also exist. For improved understanding about zero-group velocity (ZGV) modes under this type of material condition, two cases with continuously varying acoustic bulk wave velocities are investigated. Results show that a zero-group velocity mode exists with the similar robustness and detectability for both cases: non-destructive applications based on zero-group velocity modes are possible also for these two material variation cases.

Key words: Lamb waves; guided waves; impact-echo; concrete; non-destructive evaluation.

Classification system and/or index terms (if any):

Supplementary bibliographical information:	**Language:** English
ISSN and key title: ISRN LUTVDG/(TVTG-1038)/1-144/(2017)	**ISBN:** 978-91-7753-379-5 (Print), 978-91-7753-380-1 (Electronic)

Recipient's notes	**Number of pages:** 144	**Price:** 110 SEK
	Security classification:	

Signature  Date 2017-09-01

LUND UNIVERSITY

Lamb wave evaluation of concrete plates

Oskar Tofeldt
oskar.tofeldt@tg.lth.se

Doctoral Thesis
2017

Division of Engineering geology, Lund University
Box 118, SE-221 00 Lund, Sweden

ISBN 978-91-7753-379-5 (Print)
ISBN 978-91-7753-380-1 (PDF)

ISRN LUTVDG/(TVTG-1038)/1-144/(2017)

List of papers

This thesis is composed by the following papers:

Paper I O. Baggens and N. Ryden. 2015.
Systematic errors in Impact-Echo thickness estimation due to near field effects. NDT & E International, 69:16-27.
DOI: 10.1016/j.ndteint.2014.09.003.

Paper II O. Baggens and N. Ryden. 2015.
Poisson's ratio from polarization of acoustic zero-group velocity Lamb mode. The Journal of the Acoustical Society of America, 138(1):EL88-EL92.
DOI: 10.1121/1.4923015.

Paper III O. Tofeldt and N. Ryden. 2017.
Lamb wave phase velocity imaging of concrete plates with 2D-arrays. Under review, Journal of Nondestructive Evaluation.

Paper IV O. Tofeldt and N. Ryden. 2017.
Zero-group velocity modes in plates with continuous material variation through the thickness. The Journal of the Acoustical Society of America, 141(5):3302-3311.
DOI: 10.1121/1.4983296

Authors' contributions

All simulations were performed by Tofeldt (previously Baggens) with advice from Ryden. The measurement in Paper 1 was planned and performed by Ryden. The measurements in Paper 2 and Paper 3 were planned and performed by Tofeldt (Baggens) with advice from Ryden. Data from all simulations and measurements were processed and analyzed by Tofeldt (Baggens) with guidance by Ryden. Tofeldt (Baggens) prepared the figures, wrote and submitted all papers and acted as corresponding author. Ryden supported with advice, feedback and comments during the work with the papers.

Related publications

O. Baggens and N. Ryden. 2015.
Near field effects and estimation of Poisson's ratio in impact-echo thickness testing. 41st annual Review of Progress in Quantitative Non-Destructive Evaluation, QNDE Boise 2014. AIP Conference Proceedings 1650, 1415 (2015)
DOI: 10.1063/1.4914757.

O. Baggens and N. Ryden. 2015.
Lamb Wave Plate Parameters from Combined Impact-Echo and Surface Wave Measurement. International Symposium in Non-Destructive Testing in Civil Engineering, NDT-CE Berlin 2015.
http://www.ndt.net/article/ndtce2015/papers/103_baggens_oskar.pdf

O. Baggens. 2015.
Non-destructive evaluation of plate-like concrete structures: elastic properties and thickness. Licentiate thesis, Lund University, Sweden.
ISBN: 978-91-7623-259-0 (print), 978-91-7623-260-6 (electronic/pdf).

Abstract

This thesis is about the application of Lamb waves for non-destructive evaluation of plate-like concrete structures under one-sided access test condition using a portable equipment consisting of an accelerometer and impact hammer. With this type of equipment and based on array signal processing, the impact-echo (IE) method can be extended with measurements of surface waves; this extension allows an evaluation with Lamb waves. For both the conventional impact-echo method as well as evaluations based on Lamb waves, results in the literature report a systematically underestimated plate thickness. This error is investigated and reproduced in a numerical study and further verified in a measurement. A main source of uncertainty is related to the estimation of a longitudinal wave velocity from first arrivals. To reduce this uncertainty, a new approach for estimation of Poisson's ratio is proposed. The new approach is based on the amplitude polarization of the S1-ZGV Lamb mode: a through-thickness representative estimate of Poisson's ratio is thereby obtained leading to an overall improved estimation of the Lamb wave plate parameters.

A new technique based on 2D arrays is also presented. In an example, the technique is used to map (image) the variation of phase velocity for the A0 Lamb mode in the lateral plane of the plate; that is, the technique is in this case used to assess the material and plate thickness homogeneity. Compared to ultrasonic reflection imaging methods, no limitation to a specific set of operating frequencies (transducers) exists since the 2D array technique is based on a full wave field dataset with wide frequency bandwidth. Variation of material properties transversally through the thickness may also exist. For improved understanding about zero-group velocity (ZGV) modes under this type of material condition, two cases with continuously varying acoustic bulk wave velocities are investigated. Results show that a zero-group velocity mode exists with the similar robustness and detectability for both cases: non-destructive applications based on zero-group velocity modes are possible also for these two material variation cases.

Populärvetenskaplig sammafattning

Betong är ett av världens vanligaste byggnadsmaterial. Det används ofta i konstruktioner som broar, hamnar, tunnlar och kraftverk. Att kunna undersöka och bedöma tillståndet hos dessa typer av konstruktioner, ungefär som en hälsokontroll, är viktigt för säker drift och användning. Detta gäller speciellt när konstruktionerna blir äldre. Samtidigt bör inte undersökningarna orsaka skador på konstruktionerna. Det är därför viktigt med undersökningsmetoder baserade på oförstörande provning eftersom oförstörande provning inte orsakar skador vid undersökning av konstruktioner.

Oförstörande provning kan även användas för kvalitetskontroll vid nyproduktion, men också för att underlätta och planera underhåll. Därmed är oförstörande provning viktig för att uppnå effektivt resursutnyttjande och ur ett hållbart-utvecklings perspektiv. Den här avhandlingen handlar om förbättring och vidareutveckling av en metod för oförstörande provning som används för att utvärdera mekaniska egenskaper i betongkonstruktioner. De nya förbättringarna kan även användas vid oförstörande provning av andra material än betong.

Ett materials mekaniska egenskaper beskriver hur materialet beter sig under belastning. Mekaniska egenskaperna kan utvärderas genom att analysera vibrationer i form av mekaniska vågor, en typ av ljudvågor. Ljudvågorna kan ha olika längd, så kallad våglängd. Våglängden har betydelse då betongkonstruktioner består av cement, grus, sten och armeringsjärn. Korta ljudvågor kan studsa kors och tvärs på grund av gruset, stenarna och armeringsjärnen. Det gör analysen svårare. Dessutom tystnar kortare ljudvågor efter en kortare sträcka jämfört med långa ljudvågor vilket minskar räckvidden. Dessa svårigheter uppkommer till exempel vid undersökning av stora betongkonstruktioner som broar och kraftverk. Arbetet i den här avhandlingen fokuserar därför på en metod där våglängden enkelt kan anpassas efter behov.

Ljudvågor i en konstruktion kan enkelt skapas genom att slå på betong-

en med en hammare. Ljudvågorna kan sedan mätas med en accelerometer. Accelerometern kan ses som en typ av mikrofon. Arbetet i avhandlingen fokuserar på hur de inspelade ljudvågorna från accelerometern kan analyseras på bästa sätt. Bland annat mäts hur snabbt ljudvågorna färdas i konstruktionen. Hastigheten ger information om de mekaniska egenskaperna då hastigheten är beroende av materialet. Eftersom många konstruktioner har platt-liknande form är extra fokus riktat mot ljudvågor i betongplattor. I plattor måste ljudvågorna samsas på ett begränsat utrymme. Detta gör att ljudvågorna tillsammans får en särskild struktur och utseende som beror både på de mekaniska egenskaperna och tjockleken hos plattan. Tillsammans med ljudhastighetkan ger det en förbättrad utvärdering av plattans mekaniska egenskaper och tjocklek.

I början av avhandlingen studeras även tillförlitligheten i befintliga metoder som använder hammare och accelerometer. I befintliga metoder förekommer ett systematiskt fel som generar osäkerhet i uppmätta egenskaper och tjocklek. Detta systematiska fel utreds och en alternativ lösning och ny utvärderingsmetod som minskar det systematiska felet föreslås. I avhandlingen presenteras även förslag på vidareutveckling och förbättringar av hur ljudvågor kan spelas in och utvärderas över en större volym och yta än vad som tidigare gjorts. Det samlade resultatet möjliggör en förbättrad utvärdering av de mekaniska egenskaper och tjocklek i plattliknande betongkonstruktioner. Resultaten bidrar också till en djupare förståelse för ljudvågors beteende och uppträdande i plattor. Detta utgör en grund för fortsatt utveckling av metoder inom oförstörande provning för konstruktioner i såväl betong som andra material.

Preface

The work of this thesis, which represent the work within a PhD project, has been carried out at the Division of Engineering Geology at Lund University. The financial support from The Development Fund of the Swedish Construction Industry (SBUF) through Peab and The Swedish Radiation Safety Authority (SSM) is gratefully acknowledged.

The background to the PhD project can be traced back to the so-called CONSAFESYS project, organized by Scanscot Technology, about non-destructive condition assessment of nuclear reactor containments. The CONSAFESYS project involved practical testing on the decommissioned nuclear power plant Barsebäck in Sweden. At Barsebäck, both impact-echo and combined impact-echo and surface wave measurements have been performed with successful results, but sometimes also with less successful results. The experiences gained from these results called for further studies and resulted in the start of this PhD project at which I was recruited as student. The focus within this PhD project has therefore been directed towards techniques for the application of non-destructive evaluation of thick (>1 m) plate-like concrete structures. However, in the beginning of the PhD project it was realized that practical testing on a 40 years old power plant (Barsebäck) represent an extremely difficult task, especially in work with development of new processing techniques. For this reason, the field cases in PhD project used for the practical measurements were instead located to structures outside the nuclear power plant with the aim of obtaining less complicated test environments.

In November 2014, I participated in a field campaign within CONSAFESYS and performed measurements on Barsebäck. The initial data analysis further verified the difficulty in interpreting results, and focus in the PhD project was therefore continued to be directed towards the development of fundamental understanding of Lamb wave evaluation for plate-like concrete structures. It can be mentioned that staff from BAM (Bundesanstalt für Materialforschung und -prüfung), Berlin, also participated and conducted measurements. Although not presented in this thesis, their results further verified the difficulty of seismic and ultrasonic measurements on nuclear

containment walls. Clearly, this highlights the complexity of evaluations of thick and heavily reinforce concrete walls such as reactor containments. From the positive view, this means that there are more interesting work still to be done for techniques based on Lamb waves as well as ultrasonics.

During the course of this work, Nils Ryden has been my main supervisor. My foremost appreciation is directed to him for the excellent guidance, support and help I have received consistently throughout the years working with this thesis. Thank you!

I would also like to thank my assisting supervisors: Björn Thunell at Scanscot Technology and Gerhard Barmen at Lund University. During the work with Paper I, the help and feedback from Prof. John Popovics as well as Prof. Michael Lowe is gratefully acknowledged. The staff at Peab in Trollhättan is acknowledged for generously providing access to the test site used in Paper III. I am also thankful towards Christian Nielsen who did a master thesis (under Nils Ryden's and my supervision) about semi-analytical finite element modelling; his work and experiences provided great help in the development of the model used for the theoretical study in Paper IV. The feedback and interest from the reference group associated with the PhD project is also appreciated.

I would also like to express my appreciation to my fellow PhD students and the staff at the Division of Engineering Geology. After moving to Trollhättan, I have also worked part time at the research environment Production Technology West (PTW) at University West, Trollhättan. Besides from getting another interesting and valuable perspective on applications of non-destructive evaluation, this has also been very nice since I have had the opportunity to work with my PhD thesis from the office of PTW as well. Thank you all at PTW!

A major part of the work with this thesis has also been performed from the office at home (first Norrköping, then later on Trollhättan), and I would like to thank our dog, Tesla, for being the most awesome companion and colleague; especially for the nice breaks in the forest in which huge amount of energy was recovered - thus allowing problems to be solved when returning back to the computer... Thanks also to my family for support and encouragement during my years of studying. Last, but at no means the least, I want to thank my wife, Linda, for help with the "Populärvetenskaplig sammanfattning" and especially for having great patience with me (almost) never getting this work finished... Linda, you are the best!

Oskar Tofeldt
Trollhättan, August 2017

Contents

Chapter 1

Introduction

This thesis concerns the application of Lamb waves for non-destructive evaluation of plate-like concrete structures. The focus is directed towards evaluation techniques based on full wave field datasets with wide-band frequency content measured with a light portable equipment consisting of an impact hammer, an accelerometer and a data acquisition card.

1.1 Background

Concrete is a commonly used construction material and plays an important role in roads, bridges, houses, power plants, etc. Many of these structures are getting older and begin to reach the end of their expected lifetime in operation. For this reason, there is an increasing need for techniques capable of verifying structural status and integrity to ensure safety in operation; ideally, if possible, the usage of techniques based on non-destructive evaluation (NDE) is favourable. Thus, in this process, techniques based on non-destructive evaluation represent a key part (Bungey et al., 2006). Also, in view of higher demands for sustainable use of resources, the value of such techniques become even more important since obtained data can facilitate maintenance as well as provide information that can be used in quality assurance systems (Maser, 2003; Deacon et al., 1997). A general definition of non-destructive evaluation is the task of evaluating some sort of property without introducing any permanent damage on the studied object (Shull, 2002). Although non-destructive evaluation techniques can appear in a number of different forms, the general principle of all techniques is essentially the same; indirect measured field quantities such as temperature, acceleration or pressure are, by means of physical principles, models and assumptions, translated to a form that provide increased knowledge concerning the initial question that motivated the evaluation. In other words, non-destructive

evaluation is fundamentally about how observed manifestations of various physical principles can be utilized for improved knowledge about an object without altering its function.

For investigations linked to the evaluation of mechanical properties and geometry, stress waves provide an important framework. From a general viewpoint, stress waves in solids may be interpreted as a phenomenon similar to sound. Thus, by the analysis of the recorded sound from a structure, information can be obtained. Based on stress waves and for evaluation of concrete structures, the impact-echo (IE) method is an established and well-known technique (Sansalone and Streett, 1997). In the impact-echo method, the transient vibration from an impact by for instance a hammer or steel ball is studied. By evaluating the reverberating transient vibration response, information about the structure is gained. Whereas early studies interpreted the impact-echo method as a technique similar to ultrasonic pulse echo, more recent studies link the impact-echo method for evaluation of plate-like concrete structures to Lamb waves (Gibson and Popovics, 2005). Since Lamb waves are guided waves in elastic and isotropic plates (Auld, 1990), this means that the vibration response by a transient impact (such as that used in the impact-echo method) creates a stress wave field of very general characteristics; many structures can be approximated as plate-like, and for this reason, Lamb waves are used in a large number different applications. The main topic of this thesis concerns the application of Lamb waves for evaluation of plate-like concrete structures.

1.2 Motivation of work

The impact-echo method is today an established technique for non-destructive evaluation of plate-like concrete structures. This type of evaluation is usually limited to 1D point-wise measurements and the study of one single discrete frequency (mode). However, a transient impact creates a full wavefield with wide-band frequency containing Lamb waves, and the evaluation can thereby be extended with array based measurements to include more features (carriers of information) leading to an improved result. Literature shows a potential of such extended techniques and further developments within this subject are therefore of value.

Concrete is a heterogeneous material in which scattering and attenuation represent major challenges for ultrasonic testing. For this reason, development of techniques based on Lamb waves is important since such techniques are less influenced by scattering and attenuation due to lower operating frequency (longer wavelength). In addition, the wide band frequency content of a transient impact implies flexibility in terms of operating frequency. These

two aspects are of importance in the evaluation of thick concrete structures. With the increasing demand for techniques applicable for evaluation of thick concrete structures in e.g. power plants, this serve as a motivation for this thesis and its focus on Lamb waves.

1.3 Aim, objective and limitations

The aim of this thesis is to contribute to a further development of techniques based on Lamb waves for non-destructive evaluation of plate-like concrete structures under one-sided access condition. The general scope of work is limited to material characterization of acoustic/seismic wave velocities (elastic constants) and evaluation of plate thickness; i.e. the work does *not* focus on the task of finding defects/anomalies such as cracks or delaminations.

Although the field cases in this study consider plates with thickness up to 0.5 m, the work is focused on and dedicated to be applicable also for thick (>1 m) concrete structures such as those typically used in power plant constructions; given the low (compared to ultrasonic approaches) and flexible operating frequency of Lamb waves in concrete structures, it is expected that the developments presented in this thesis are valid also for thicker (>0.5 m) plate-like concrete structures.

By first studying and investigating current existing techniques for Lamb wave evaluation of plate-like concrete structures, potential areas for further improvements are identified. With this as starting point and Lamb waves as the theoretical foundation, developments are proposed through the study of data obtained from both numerical models and practical measurements. The presented work is limited to the evaluation of plate-like concrete structures for which Lamb waves is an applicable assumption; that is, structures such as piles are not considered. From the practical perspective, the condition of one-sided access is considered throughout the thesis. The equipment is limited to an impact hammer, an accelerometer and a data acquisition card; this limitation is intentionally selected to ensure the development of techniques that is realizable with a simple and portable measurement equipment. Only a few field cases are considered in the practical measurements; naturally, for further developments it is important to study the applicability of the presented techniques and results at more field cases.

1.4 Contributions of thesis

Paper I provides a study of the reliability of estimated plate thickness from the conventional impact-echo method and a combined impact-echo and sur-

face wave technique (Lamb wave evaluation); this study identifies a systematic error. Based on these findings, a new approach for estimation of Poisson's ratio is proposed in Paper II; this approach also highlights the potential of using multicomponent measurements. A benefit of this new approach is that a through-thickness representative estimate of Poisson's ratio is obtained. In Paper III, the analysis of Lamb waves is extended to 2D arrays, thus allowing mapping (imaging) of potential material or thickness variation in the lateral plane of the plate. In the theoretical study given in Paper IV, results that contribute to improved understanding of zero-group velocity modes in plates with material variation transversally through the thickness is presented.

1.5 Thesis outline

A literature review is given in Chapter 2. Some short notes on elastic wave theory, modelling and measurements are given in Chapter 3, 4 and 5, respectively. Results are presented in Chapter 6. Summarizing conclusions and recommendations for further work based on the experiences gained during the work with this thesis are given in Chapter 7 and 8, respectively. The bibliography containing the references in the thesis is presented in Chapter 9 and the papers are included in the Appendices

Chapter 2

Related research

2.1 General note

This chapter provides a literature review about non-destructive evaluation techniques based on elastic waves. Given the limitations of this thesis, the presentation is focused on evaluation of plate-like concrete structures under one-sided access condition. That is, although some techniques are applicable for other structural shapes as well (e.g. beams and columns), the focus is intentionally directed towards the techniques operating in plate-like applications.

2.2 Ultrasonic techniques

Techniques based on ultrasonic wave propagation can be used for non-destructive evaluation of concrete structures. The first measurements of ultrasonic pulse velocity in laboratory specimens were reported around the 1940-1950s (Bungey et al., 2006), and practical measurements from constructions sites are starting to be reported from the 1960s (Malhotra and Carino, 2004). Typically, such measurements are based on two ultrasonic transducers operating in a pitch-catch configuration to obtain the time-of-flight for the ultrasonic pulse. After the introduction of dry-point transducer (Shevaldykin et al., 2002), developments of reflection imaging techniques by means of ultrasonic echo and synthetic apertures can be noticed (Schickert et al., 2003). Such techniques are used for the creation of a reflection image in which internal objects and anomalies, such as defects, appear as points or regions with deviating colour. Consequently, techniques based on ultrasonics, and synthetic apertures in particular, are now popular for testing of concrete structures with recent developments illustrated by wireless trans-

ducer systems (Wiggenhauser et al., 2016) for large concrete structures and advanced post-processing algorithms (Müller et al., 2012) adopted from the field of geophysics. However, since concrete is a composite material of cement and aggregates, wave scattering represents a significant challenge that may restrict the possibilities for evaluation. Furthermore, high attenuation of the ultrasonic pulse do also represent a major challenge. As a result, scattering and attenuation may ultimately lead to a case in which the creation of a reflection image with desired resolution and coverage is no longer realizable (Almansouri et al., 2017). For high frequencies or large concrete structures that also may include vast amount of reinforcement bars and potentially coarse aggregates, this may be a particular problem since the amount of attenuation and scattering is related to the number of wavelengths along the propagation path of the ultrasonic pulse.

2.3 Impact-echo method

An alternative methodology, less influenced by scattering and attenuation, is to use elastic waves in a lower frequency regime compared to ultrasonics; i.e. to use a longer spatial wavelength. Naturally, compared to ultrasonic imaging techniques, this implies a decreased spatial resolution. However, on the other hand, this decreased resolution also implies a corresponding increase in the range of coverage. For evaluation of plate-like concrete structures with elastic waves operating in a lower frequency regime compared to ultrasonic approaches, the impact-echo (IE) method is a common and established technique (Sansalone and Streett, 1997; Sansalone, 1997). The method is also standardized by according to ASTM C 1383. The impact-echo method is based on the measurement of the dynamic response of the tested structure subjected to a transient impact. Ideally, this response contains a distinct frequency peak corresponding to a dominating reverberating resonant mode; the frequency of this mode is dependent on the material properties and geometry. In other words, the procedure of the impact-echo measurement corresponds to a general resonance evaluation. In its most simple form, the evaluation with the impact-echo method is based on monitoring the relative variation of the frequency response for the resonant mode at different locations of the tested structures. A variation in frequency serves as an indicator of varying material properties; faults and anomalies can thereby be detected. Examples of improvements supporting such evaluations are automatic data acquisition (Schubert and Köhler, 2008) as well as air-coupled transient source generation (Dai et al., 2013) and detection (Zhu and Popovics, 2007). Such developments facilitate the creation of an image showing the relative variation of the response along a surface (Schubert and Köhler, 2008; Zhu and Popovics, 2007).

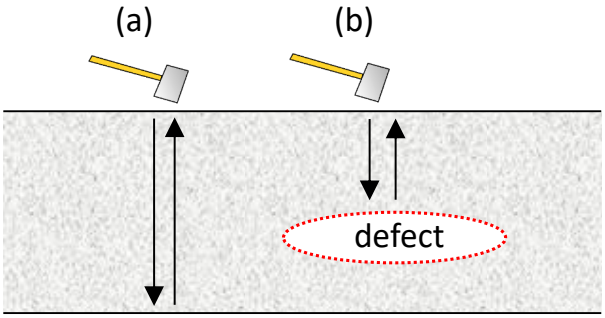

Figure 2.1: Principle of the traditional and empirical conceptual model for impact-echo testing. Figure created after Schubert and Köhler (2008). (a) Homogeneous case without anomaly. (b) Non-homogeneous case due to a flaw: a change in "travel time" and thus frequency is observed.

In the impact-echo literature, the method is traditionally explained with an empirical conceptual model (Sansalone and Streett, 1997) which is illustrated in Figure 2.1. Figure 2.1 shows the travelling path of a mechanical wave generated by an impact at the top surface. If the plate contains no flaw (Figure 2.1(a)), the wave will reverberate and create a resonance between the top and bottom plate surface. If a flaw such as a delamination is present (Figure 2.1(b)), the travel path changes, which in turn also changes the frequency of the resonance. The frequency of the resonance is for this empirical conceptual model suggested to be governed by the expression

$$F = \frac{\beta V_P}{2h} \tag{2.1}$$

with the longitudinal wave velocity V_P, the *effective* plate thickness h and the geometrical correctional factor β. Eq. 2.1 provides an estimate of the thickness h for the studied object once F, β, and V_P are known. Typically, β is assumed depending of the object geometry and for concrete plates the value is usually suggested to be equal to 0.96 (Sansalone, 1997). Early studies using the impact-echo method and this equation for estimation of thickness report accuracies within 3 % (Sansalone and Streett, 1997). However, studies with more significant deviations exist (Popovics et al., 2006, 2008; Maser, 2003). In these studies the plate thickness is underestimated in 18 of 19 locations with a mean error of -8 %. Traditionally, such deviation in results has been explained to be associated with an improper selection of value for the β factor.

As may be noticed, the empirical conceptual model of impact-echo is very similar to the model used to described ultrasonic pulse echo measurements.

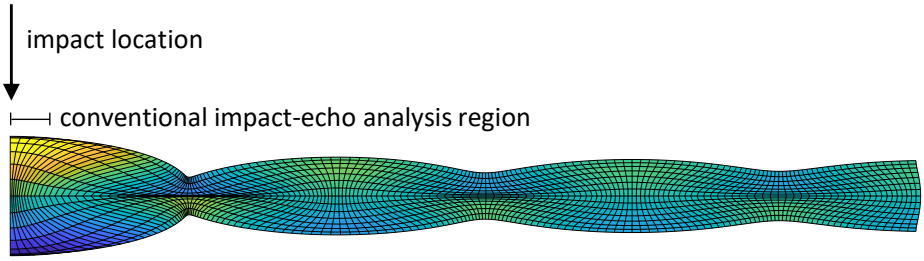

Figure 2.2: Illustration of the first symmetric (S1) zero-group velocity (ZGV) mode corresponding to the resonance mode used in impact-echo measurements on plates. Figure created after Gibson and Popovics (2005). Note the difference in spatial distribution of the mode compared to the empirical conceptual model defined by "ray paths" in Figure 2.1.

However, since the resonance mode used in impact-echo testing of plates is linked to the zero-group velocity (ZGV) point of the first symmetric Lamb mode (S1) (Gibson and Popovics, 2005), this empirical interpretation is somewhat ambiguous. This is further evident by Figure 2.2, which shows the mode shape of the S1-ZGV mode, i.e. the mode shape corresponding to resonance mode employed in impact-echo testing of plates; a major difference between the spatial distribution of this mode shape and the ray pattern (Figure 2.1) given by the classical empirical conceptual model is obvious. As explained and practically demonstrated by Abraham et al. (2011) on a plate with varying amount of reinforcement as well as tendon ducts with varying amount and type of filling, this means that the impact-echo method should be interpreted as a measurement of a resonance frequency which is dependent on the local stiffness of the plate.

Gibson and Popovics (2005) also demonstrate that the theoretically exact β factor is a function of Poisson's ratio. Although not explicitly stated, the results from Gibson and Popovics (2005) implies that for a proper evaluation of the plate properties such as the thickness parameter, Lamb wave theory must be used. In Lamb wave theory, a laterally infinite plate is defined by three independent parameters: the shear wave speed V_S, Poisson's ratio ν and thickness h (Auld, 1990). As a result, the exact thickness h of an unknown plate can only be determined with Eq. 2.1 if the longitudinal wave velocity V_P and Poisson's ration ν are known. Even though the Lamb wave interpretation of impact-echo nowadays is widely accepted, it is still not unusual to encounter the empirical conceptual model (see e.g. (Liu et al., 2017; Garbacz et al., 2017) in recent (2017) published papers. Thus, the misconception stating that the impact-echo method represents an evaluation technique with discrete and pointwise sensitivity (see Figure 2.1) rather than

an evaluation technique influenced by a major volume (see Figure 2.2) may unfortunately still exist in some cases.

From a general perspective, the link between the impact-echo method and Lamb waves means that the resonance mode ideally should be interpreted as a zero-group velocity (ZGV) Lamb mode rather than a particular mode only limited to concrete plates. In fact, ZGV Lamb modes represent a general wave phenomena (Kausel, 2012; Prada et al., 2008) with some interesting applications given by: evaluation of acoustic bulk wave velocities and Poisson's ratio in metal plates with laser-based measurements (Clorennec et al., 2007), thin-layer thickness (Cès et al., 2011), hollow cylinders (Cès et al., 2012), interfacial bond stiffness (Mezil et al., 2015), and potentially air-coupled measurements (Holland and Chimenti, 2003; Zhu and Popovics, 2007).

2.4 Impact-echo and surface waves

With Lamb wave theory as base combined with the important link provided by Gibson and Popovics (2005), an extension of the basic impact-echo measurement is well motivated and sensible. Since an impact-echo measurement, which corresponds to a very general transient excitation, creates elastic waves with a wide frequency bandwidth, a natural extension is to combine the impact-echo frequency estimate (i.e. the estimate of the S1-ZGV Lamb mode frequency) with a measurement of propagating surface waves. Examples of such combined techniques are given by Kim et al. (2006); Ryden and Park (2006); Barnes and Trottier (2009); Shokouhi (2009) and Popovics et al. (2008). Although variations exist between these techniques, the main idea is still the same: by use of relations that govern wave propagation and Lamb wave theory, the Lamb wave plate parameters shear wave velocity V_S, Poisson's ratio ν and thickness h are obtained. Compared to the traditional impact-echo method, these techniques allow the estimation of the Lamb wave plate parameters (V_S, ν and h) under one-sided access test condition without the requirement of calibration cores or assumed β values. However, this comes to the price of that they all are dependent on at least three independent input quantities in order to allow the determination of the Lamb wave plate parameters; i.e. three pieces of information are required to solve a system of three variables. Naturally, there exist different approaches for how these three parameters can be obtained; this represent the topic of the following section.

2.5 Obtaining the Lamb wave plate parameters

As mentioned previously, three independent parameters define an isotropic and laterally infinite plate in Lamb wave theory: shear wave speed V_S, Poisson's ratio ν and thickness h (Auld, 1990). That is, to characterize a plate in a non-destructive evaluation based on Lamb wave theory, at least three quantities must be measured. This section will discuss and present some different ideas and techniques which can be used to solve this non-destructive evaluation task of obtaining the Lamb wave plate parameters.

Poisson's ratio

Poisson's ratio can be determined by measuring the longitudinal wave velocity and the Rayleigh wave velocity (Wu et al., 1995): the ratio between these two velocities is only dependent on Poisson's ratio. This technique is analogue to the technique in which Poisson's ratio is determined from the ratio between the longitudinal wave velocity and shear wave velocity (Auld, 1990). It is clear that for a reliable estimation of Poisson's ratio from such techniques, accurately estimated wave velocities are necessary. Furthermore, another aspect to consider is that for a representative estimation of Poisson's ratio, the two velocities should ideally be measured over the same material volume; this may impose a challenge when two wave modes of potentially different frequency (wavelength) and mode shape (sensed volume) is utilized.

Poisson's ratio can also be estimated from the ratio between the frequencies of the S1-ZGV Lamb mode and the A2-ZGV Lamb mode (Clorennec et al., 2007); the A2-ZGV Lamb mode corresponds to the ZGV point of the second anti-symmetric (A2) Lamb mode. This approach is demonstrated successfully for several thin homogenous metal plates (Clorennec et al., 2007), but only a few measurements are reported for concrete plates (Gibson, 2004; Baggens and Ryden, 2015b). The ratio between the S1-ZGV Lamb mode frequency and the Rayleigh wave velocity can also be used to determine Poisson's ratio, but this approach is limited by the requirement of a known plate thickness (Medina and Bayón, 2010).

Alternatively the amplitude ratio between the surface in-plane and surface normal components of the Rayleigh wave can be used to estimate Poisson's ratio (Bayon et al., 2005). This amplitude ratio may be interpreted as the amplitude polarization of the mode. However, to the author's best knowledge, this approach has not been demonstrated on concrete plates. Inspired by this approach, Baggens and Ryden (2015d) (Paper II) proposed and demonstrated that the amplitude polarization of the S1-ZGV Lamb mode can be used for estimation of Poisson's ratio. Compared to approaches based on data from multiple modes such as the longitudinal wave and the

Rayleigh wave, this approach provides a through-thickness representative value for Poisson's ratio since the S1-ZGV Lamb mode is present through the entire thickness of the plate.

Longitudinal wave velocity

The longitudinal wave velocity is usually estimated from the time taken by the first arriving wave from a transient impact to travel between two or multiple points separated by a known distance along the surface. A possible source of uncertainty in this type of analysis is the identification of a correct first arrival time. Unfortunately, identifying an accurate time point for the first arriving wave is not a trivial task; typically, the displacement magnitude of the first arriving wave is very small. Despite this challenge of finding the first arriving wave, a commonly used procedure is to identify the first value above a certain threshold, and assume that this observed wave corresponds to a pure longitudinal wave. An alternative approach, which may facilitate the identification of the first arriving wave, is to study the trend of the measured signal instead of using a threshold level (Popovics et al., 1998).

Additional uncertainty in measurements of the longitudinal wave velocity may occur if the material properties vary through the thickness. In such cases, the measured longitudinal wave velocity along the surface will be different from the longitudinal wave velocity measured through the plate. That is, a measurement along the surface will not provide a through-thickness representative estimation, which in turn may lead to uncertainties in the evaluation of the Lamb wave plate parameters. Gibson (2004) observed a systematic variation of this kind in which an increased velocity was observed in measurements through the thickness of the plate compared with velocities obtained from measurements along the surface. To account for such variations in velocity, Popovics et al. (2006) proposed a correction factor to compensate for the slower longitudinal wave velocity along the surface.

As an indirect alternative to a measurement based on the first arriving wave, the longitudinal wave velocity may be calculated from the Rayleigh wave velocity (Kim et al., 2006). However, this approach is dependent on the assumption of an already known value of Poisson's ratio.

Rayleigh wave velocity

A simple technique for estimation of the Rayleigh wave velocity is to study the cross correlation of two signals separated by a known distance (Wu et al., 1995). However, this technique may suffer from dispersion effects (Shin et al., 2007), and for this reason, the use of a continuous wavelet

transform has been proposed. Another proposed approach for estimation of a Rayleigh wave velocity is the spectral analysis of surface waves method, SASW (Heisey et al., 1982). More recent approaches based on multichannel datsets (Ryden and Park, 2006; Barnes and Trottier, 2009) propose that the Rayleigh wave velocity can be estimated from the asymptotic trend of the fundamental Lamb modes in frequency-phase velocity domain (Park et al., 1999). Such analysis is sometimes referred to as multichannel analysis of surface waves (MASW) and is usually based on Fourier transforms in both time and space domain (Alleyne and Cawley, 1991).

S1-ZGV Lamb mode frequency

Robust estimation of the S1-ZGV Lamb mode frequency is important to ensure reliability in evaluated Lamb wave plate parameters. In Lamb wave theory, plates are characterized by laterally infinite dimensions (Auld, 1990). Naturally, this condition is rarely found in practical testing of concrete plates. Nevertheless, ZGV Lamb modes are still defined also for bounded plates (Cees et al., 2011), but reflections from surface waves and other structural modes may impose additional complexity to the interpretation of the measured frequency spectrum. Thus, to assist the identification of a correct S1-ZGV Lamb mode frequencey, time frequency analysis has been proposed (Abraham et al., 2000; Algernon and Wiggenhauser, 2007).

For the cases of combined impact-echo and surface wave measurements (e.g. MASW), the spatial distribution of the S1-ZGV mode shape may also be employed for improved detectability of frequency. For instance, by summation of the signals in vicinity to the impact source, the identification of the S1-ZGV Lamb mode frequency can be facilitated (Ryden and Park, 2006; Ryden, 2016). Another similar approach is based on a multiplication of amplitude spectrums from signals measured close to the impact source (Medina and Garrido, 2007). For both these approaches, the influence from propagating waves and scattering is reduced since the summation and multiplication amplifies the frequency of the S1-ZGV Lamb mode due to its spatially coherent characteristic.

2.6 Uncertainties and challenges

Empirical conceptual model

Although several improvements have been proposed for the impact-echo method, among them the very important link to Lamb wave theory by Gibson and Popovics (2005), it can be observed that the empirical conceptual

Test location		Estimated thickness (mm) and relative error (%)			
No	Thickness (mm)	Impact-echo (ASTM C1383)		Impact-echo and surface wave analysis (Lamb wave analysis)	
1	256	-		252	(-2%)
2	263	-		244	(-7%)
3	246	243	(-1%)	242	(-2%)
4	261	195	(-25%)	237	(-9%)
5	337	293	(-13%)	309	(-8%)
6	281	268	(-5%)	254	(-10%)
7	239	224	(-6%)	223	(-7%)

Table 2.1: Estimated thickness from impact-echo and combined impact-echo and surface wave analysis (MASW). Table created from data presented by Popovics et al. (2008).

model still is used as theoretical framework in some cases; this may be one reason to that the impact-echo method is sometimes compared and discussed as a member within the family of ultrasonic pulse echo techniques. To the author's opinion, this is somewhat sad since this interpretation may prevent the evaluation from taking full advantage of the possible information available in the excited Lamb wave field. Furthermore, and also to the author's opinion, this interpretation may also contribute to confusion in discussions about sensitivity for defects and the capability of detecting reinforcement bars etc.

Underestimated plate thickness

In the literature, a systematic error in terms of underestimated plate thickness from impact-echo measurements are observed, see Section 2.3 and Table 2.1. As example, in the results presented in Table 2.1, a systematic error is also observed for the combined impact-echo and surface wave analysis (MASW/Lamb wave analysis/right column). Baggens and Ryden (2015a) (Paper I) reproduced this systematic error in numerical simulations and also observed the error in a practical measurement with both a multichannel analysis of surface waves (MASW) and a conventional impact-echo set-up. A possible source to this systematic error is near-field effects caused by cylindrical spreading of waves from a point source and interference of localized wave modes created due to the point source excitation. Within the field of geophysics, near-field effects are observed and studied for half-spaces (Zywicki and Rix, 2005; Roesset et al., 1990; Roesset, 1998; Bodet et al., 2009). However, for the case of non-destructive testing of plates, only a few studies have recognized the influence from the near-field of a point source (Ditri

et al., 1994). In the context of impact-echo thickness testing of plates, near-field effects have traditionally not been taken into account (Baggens and Ryden, 2015a) (Paper I). Baggens and Ryden (2015a) (Paper I) demonstrated that the longitudinal wave velocity estimated from the first arriving wave represent the main cause of the underestimated thickness. By instead using alternative approaches for estimation of Poisson's ratio that are independent on the longitudinal wave velocity estimated from first arrivals, this systematic error may be reduced (Baggens and Ryden, 2015d) (Paper II).

Evaluation domain

In the conventional impact-echo method, the data is interpreted and evaluated at a pointwise level. As mentioned in Section 2.3, by repeating this evaluation at multiple locations, either through an automated or manual process, variations in the response can be investigated. However, since a transient impact source is used that creates a full wave field propagating outwards from the source location, the pointwise evaluation is somewhat limited. A step in the direction of extending the evaluation domain and incorporating more information carriers within the full wave field is taken by the combined techniques described in Section 2.4. Yet, these combined techniques are typically limited to evaluation domains such as lines. With inspiration from near-surface geophysical applications (Boiero et al., 2012) and testing of metal plates (Harley and Moura, 2013), a natural extension of testing of plate-like concrete structures is to consider data collected and evaluated from a two-dimensional surface. An example of such evaluation applicable for concrete applications is demonstrated and proposed in Paper III. Compared to the impact-echo method evaluated at multiple discrete points, this approach enables the possibility to study the variation of *propagating* waves over a wide frequency bandwidth for a two-dimensional surface.

Imaging

For non-destructive imaging analysis of concrete structures with elastic waves, techniques based on ultrasonic pulse echo and synthetic apertures represent a predominant group (Pla-Rucki and Eberhard, 1995; Schickert et al., 2003; Wiggenhauser et al., 2016; Schickert and Krause, 2010). Within this field, some recent developments include application of data processing algorithms initially proposed in the field of geophysics (Müller et al., 2012; Grohmann et al., 2016, 2017). Although some ultrasonic imaging applications report the usage of frequencies as low as 25 kHz (Grohmann et al., 2016), the common range of ultrasonic test frequency is typically 50-200 kHz (Schickert and

Krause, 2010). For frequencies below this ultrasonic domain, imaging of results from impact-echo data is proposed in the literature for both B-scans (Schubert et al., 2004) as well as C-scans (Zhu and Popovics, 2007; Ohtsu and Watanabe, 2002). Some references also reports about the possibility of utilizing synthetic apertures focusing techniques on data from impact-echo measurements to enable reflection imaging transversally through the plate (Schubert and Köhler, 2008; Ganguli et al., 2012). However, to the best of the author's knowledge, no example of technique for imaging analysis with *propagating* Lamb modes and below ultrasonic frequency applied on plate-like concrete structures exists in the literature. With aim of removing this gap, a 2D arrays technique for Lamb wave phase velocity imaging of plate-like concrete structures is proposed in Paper III.

Material gradients

For testing of plate-like concrete structures with elastic waves, a condition of isotropy based on constant material properties through the plate thickness is usually assumed (e.g. the assumption of Lamb wave propagation). However, in a number of practical studies concerning concrete structures, the case of inhomogeneity due to varying material properties is being reported Abraham et al. (2012); Boyd and Ferraro (2005); Popovics et al. (2006, 1998); Popovics (2005); Qixian and Bungey (1996); Turgut and Kucuk (2006); Hu et al. (2006). It is suggested that such material variations may be caused by uneven settlement of aggregates during casting, uneven moisture distribution, material degradation or corrosion of internal steel reinforcement Neville and Brooks (2010). To better understand the influence from potential material variation through the plate thickness in techniques based on zero-group velocity modes (such as the impact-echo method), Tofeldt and Ryden (2017) (Paper IV) investigated the behaviour of the lowest symmetric zero-group velocity mode for two plates with continuously varying acoustic bulk wave velocities. They concluded that ZGV modes, similar to the S1-ZGV mode, exist and are detected with same robustness as for the isotropic case. However, depending on the magnitude of the material variation, the evaluation of representative plate properties may in practice be challenging due to additional complexity of the wave field.

Chapter 3

Elastic wave theory

3.1 Infinite spaces

Two different type of mechanical waves can exist in a three-dimensional infinite space: the longitudinal wave and the transversal wave (Auld, 1990). These two types of waves are also referred to as P-waves and S-waves, where the capital P and S represent **p**rimary or **p**ressure and **s**econdary or shear, respectively. The longitudinal wave velocity V_L in a three-dimensional infinite space is calculated according to:

$$V_L = \sqrt{\frac{E(1-v)}{\rho(1+v)(1-2v)}} \tag{3.1}$$

where E, v, ρ are the Young's modulus, Poisson's ratio and density, respectively. The transversal wave velocity V_T in a three-dimensional infinite space is calculated according to:

$$V_T = \sqrt{\frac{E}{2\rho(1+v)}} \tag{3.2}$$

The ratio between the longitudinal wave velocity and the transversal wave velocity is only dependent of Poisson's ratio and is sometimes referred to as κ and consequently given by:

$$\kappa = \frac{V_L}{V_T} = \sqrt{\frac{2(1-v)}{1-2v}} \tag{3.3}$$

The ratio κ is an important quantity, which provides a fundamental link between the acoustic bulk wave velocities V_L and V_T. The particle movements of plane longitudinal and transversal waves are shown in Figure 3.1.

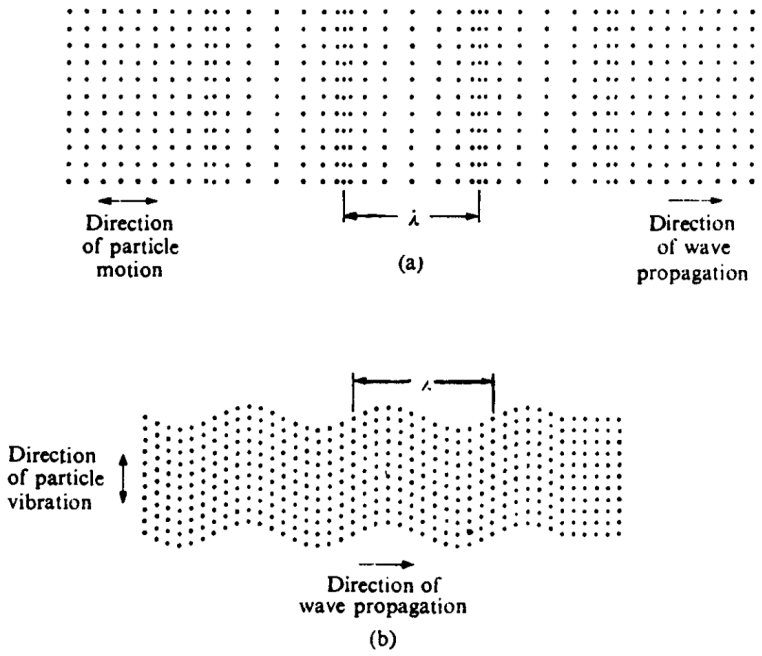

Figure 3.1: Illustration of particle motion for: (a) Longitudinal wave, (b) Transversal wave. Figure from Graff (1975).

3.2 Half-spaces

A body which is infinite below a certain plane and non-existent above this plane is typically referred to as a half-space. The probably most common example of such semi-infinite body is the earth, which is almost infinite in the lateral/horizontal direction and depth, i.e. it is only limited by the earth surface if we assume a flat earth and ignore the curvature. However, structures which are similar to half-spaces can be found in many places. Typically, it is the wavelength in comparison with the dimensions of the object that determines if an object can be assumed as infinite or not, rather than the specific dimensions of the object.

The free surface of the half-space makes it possible for surface waves to exist. Surface waves, which are often called Rayleigh waves, are created from a combination (superposition) of longitudinal and transversal waves. An example of a surface wave or Rayleigh wave is shown in Figure 3.2. Figure 3.2 shows that the displacement magnitude of the movement dominates close to the surface; hence the name surface wave.

The velocity of the Rayleigh wave cannot be determined in the same straightforward fashion as for the longitudinal and transversal wave. To determine the exact velocity, the so-called Rayleigh equation must be solved (Vik-

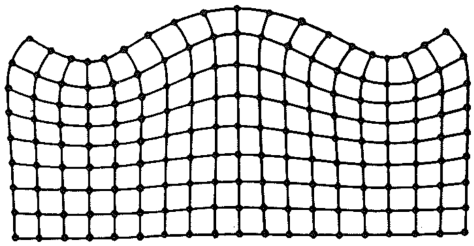

Figure 3.2: Rayleigh wave mode shape. Figure from Viktorov (1967).

torov, 1967). However, an approximation of the Rayleigh wave velocity can for example be determined from the relation given by (Achenbach, 1973):

$$\frac{V_R}{V_T} \approx \frac{0.862 + 1.14\nu}{1 + \nu} \tag{3.4}$$

3.3 Lamb waves

We have seen that two type of waves exist in an isotropic infinite body, and when a free surface exists (i.e. a half-space), Rayleigh waves can also exist. In the case of a plate, which has two free surfaces, additionally complexity is added to the wave propagation theory. This theory of wave propagation in linear elastic and laterally infinite plate is commonly referred to as Lamb wave theory.

The two free surfaces of the plate is equivalent to a traction free boundary condition, which means that the stress combined from longitudinal and transversal waves must equal zero at these surfaces. The boundary condition implicates that only certain combinations of longitudinal and transversal waves within the plate can exist at a given frequency. This means that only certain combinations of angular frequencies ω and lateral wave numbers k are possible. The valid combinations of frequencies ω and lateral wave numbers k, so-called ω-k pairs, define the dispersion characteristics of the plate, and can be obtained by solving the Lamb wave equation (Viktorov, 1967):

$$\frac{\tan(\beta h/2)}{\tan(\alpha h/2)} = -\left[\frac{4\alpha\beta k^2}{(k^2 - \beta^2)^2}\right]^{\pm 1} \tag{3.5}$$

where

$$\alpha^2 = \omega^2/V_L^2 - k^2$$
$$\beta^2 = \omega^2/V_T^2 - k^2$$

V_L and V_T are the longitudinal and transversal wave velocities, respectively, and h represents the plate thickness. The Lamb modes are divided into two

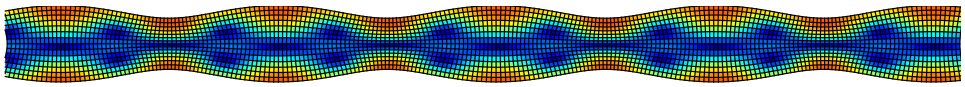

Figure 3.3: Example of symmetric Lamb mode.

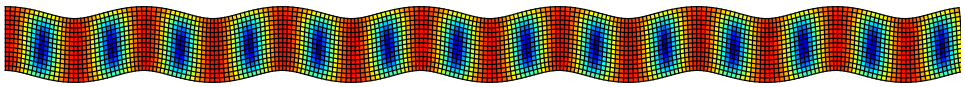

Figure 3.4: Example of anti-symmetric Lamb mode.

main families: symmetric and anti-symmetric modes. The positive sign of the exponent on the right side of Eq. (3.5) defines symmetric modes, whereas the negative sign defines anti-symmetric modes. Examples of a symmetric and an anti-symmetric Lamb mode are shown in Figure 3.3 and Figure 3.4, respectively.

The valid ω-k pairs define the dispersive characteristics of the plate. The dispersion of Lamb waves contain important information which can for example be used to determine the elastic plate properties and thickness. The dispersion relations for a plate can be illustrated in many ways. One example is to plot the ω-k pairs for each Lamb mode directly, see Figure 3.5. Another possibility is to present the dispersion curves in the frequency-phase velocity domain, see Figure 3.6. The Rayleigh wave velocity can, for example, be determined by studying the convergence of the phase velocities for the A0 and the S0 modes, see Figure 3.6. The S1-ZGV point, which is the point of the minimum frequency of the S1-mode, is another quantity which can be determined. The frequency of this point corresponds to the reverberating resonance used in traditional impact-echo measurements (Gibson and Popovics, 2005).

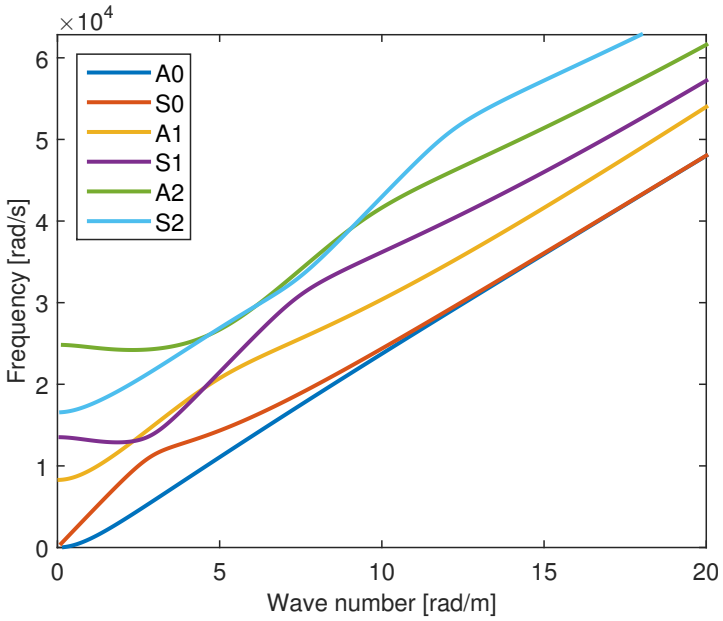

Figure 3.5: Dispersion curves (wave number-frequency plot) for a plate with Young's modulus 40 GPa, Poisson's ratio 0.2, density 2400 kg/m^3, and thickness 1 m.

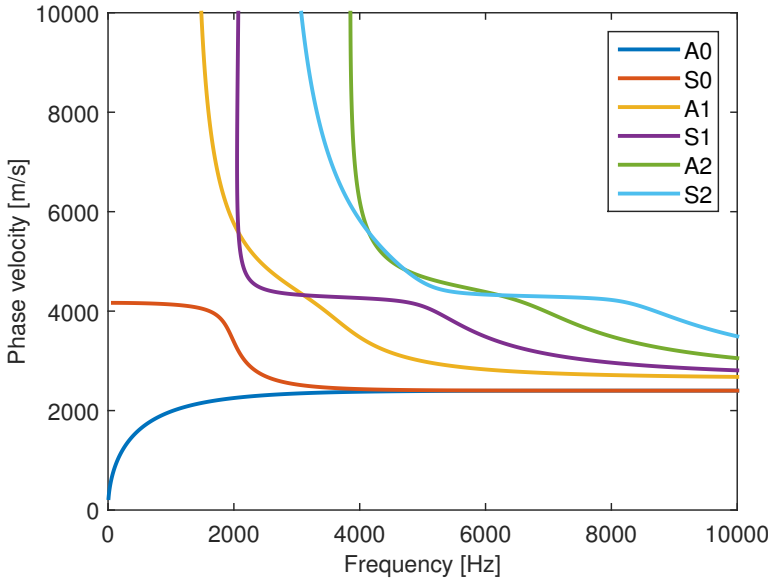

Figure 3.6: Dispersion curves (frequency-phase velocity plot) for a plate with Young's modulus 40 GPa, Poisson's ratio 0.2, density 2400 kg/m^3, and thickness 1 m.

Chapter 4

Numerical modelling

4.1 Calculation of dispersion curves

Although Eq. 3.5 is written in a compact and explicit form, the solution of this equation is not trivial, and must typically be performed with numerical approaches. For the cases of plate with continuous material variations, as in Paper IV, no simple and closed form expression as Eq. 3.5 exists. As approach for handling these cases, a semi-analytical finite element (SAFE) technique is adopted in Paper IV. This approach is based on the methodology presented by (Predoi et al., 2007; Bartoli et al., 2006; Treyssède and Laguerre, 2013) and implemented in the commercial FE code COMSOL (COMSOL Inc., 2016) and MATLAB.

4.2 Response due to point source excitation

The finite element software COMSOL (COMSOL Inc., 2016) and the computational software MATLAB are used to perform simulations of wave propagation in elastic plates. The following presentation will focus on the implementation of a finite element model which simulates the response of a plate subjected to transient impacts. This implementation is mainly based on the modelling techniques presented by Castaings et al. (2004); Hosten and Castaings (2006); Ryden and Castaings (2009). This approach for modelling is selected since it allows control over the mesh size and the absorbing region. Since the computation is performed in frequency domain, an uncoupled problem is obtained; this problem can efficiently be solved in parallel thus allowing a potential speed-up.

As an example model in this presentation, an axially symmetric plate model

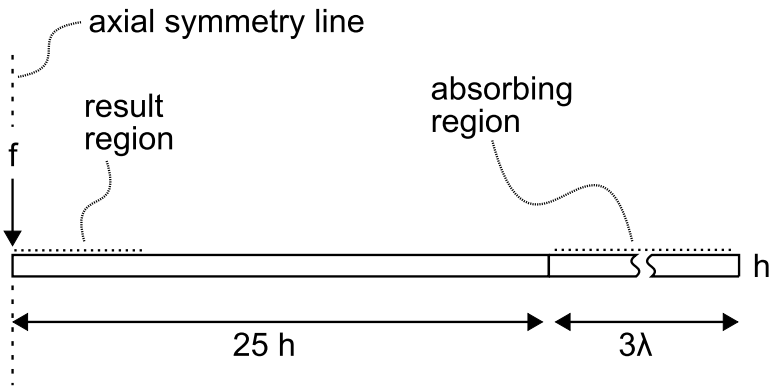

Figure 4.1: Sketch of plate model.

is shown in Figure 4.1. This type of model corresponds to the model type used in Paper I, Paper II and Paper IV. A load is applied at the axial symmetry axis to simulate the point load. The plate is divided into two main regions: result region and absorbing region. The response is extracted from the result region whereas the absorbing region is used to simulate infinite boundaries of the plate. The absorbing region is created by a gradually (cubically) increasing damping ratio (Castaings et al., 2004; Ke et al., 2009).

The model is solved in frequency domain using an element mesh and absorbing region which are adjusted to the frequency. At low frequencies a coarse mesh is used, as opposed to the case of high frequencies where a fine mesh is used (Ryden and Castaings, 2009). The absorbing region is adjusted according to frequency; a longer absorbing region is used for low frequencies and the opposite. The response of the plate in terms of complex amplitudes, i.e. the so-called frequency response function, is extracted from the result region of the plate, see Figure 4.1. The absolute amplitude of an example frequency response function is plotted in Figure 4.2.

Force excitation pulses, are applied at the axial symmetric axis to simulate a point load (see Figure 4.1). These pulses are defined using a Gaussian monopulse. An example of a force excitation pulse is shown in Figure 4.3. The dynamic response to the point load excitation in time domain are obtained from the inverse discrete Fourier transforms of the frequency response functions multiplied with the frequency spectrum of the pulses (Castaings et al., 2004). An example of dataset in time domain is shown in Figure 4.4. As a graphical illustration of the modelling process, an overview of the simulation technique is shown in Figure 4.5.

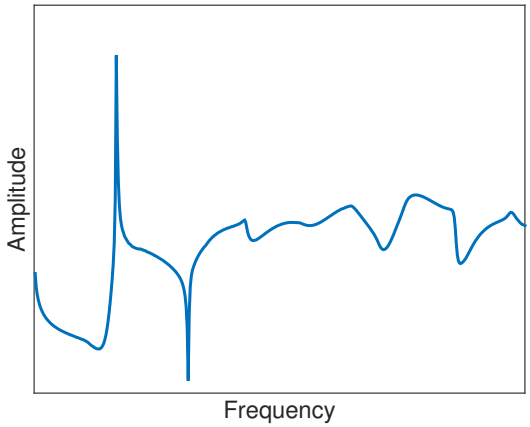

Figure 4.2: Example of the absolute value of frequency response function.

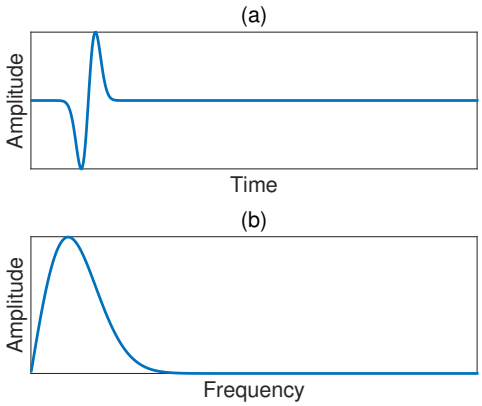

Figure 4.3: Example of force excitation pulse in (a) Time domain, (b) Frequency domain.

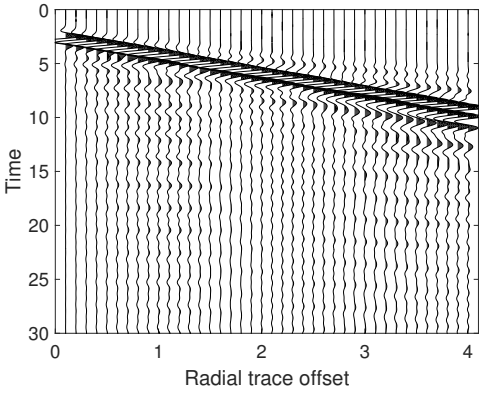

Figure 4.4: Example of dynamic response in time domain.

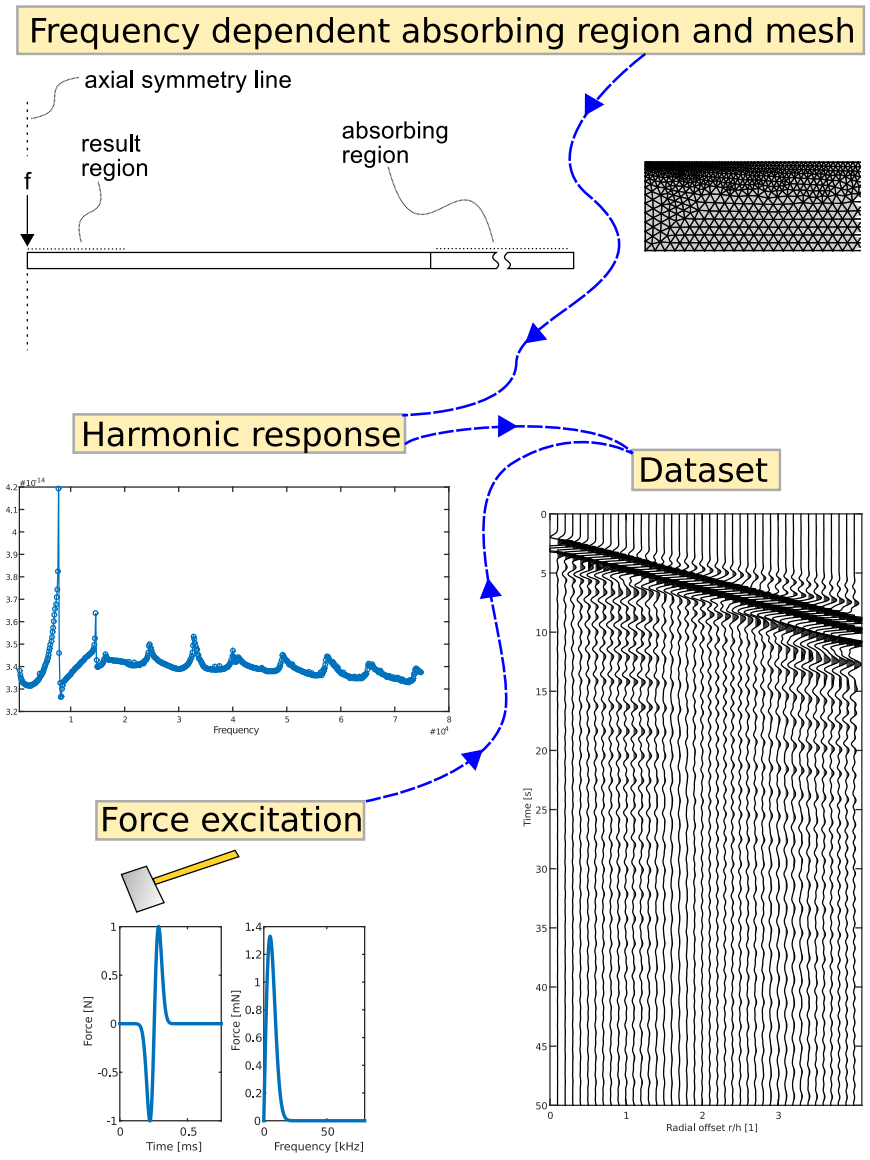

Figure 4.5: Overview of modelling technique.

Chapter 5

Measurement equipment

Practical measurements in this thesis are performed with an equipment consisting of an impact hammer as source and an accelerometer as receiver. The practical measurements are executed by performing several hammer impacts at increasing offset distance from the accelerometer which is kept at a fixed position throughout the measurement. By connecting the impact hammer and accelerometer to a data acquisition card, the structural response in terms of acceleration as well as the time history of the impact-force from the hammer is recorded. The recorded data are stored and saved in a laptop computer. Since the impact hammer also works as a triggering device, the reciprocity theorem for linear elastic system allows the creation of a time-synchronized multichannel dataset. This type of multichannel/ array based dataset is typical for a combined impact-echo and surface wave analysis, but the type of dataset is also observed in many other non-destructive applications as well as geophysical measurements. A sketch illustrating the practical measurement techniques and procedure is shown in Figure 5.1.

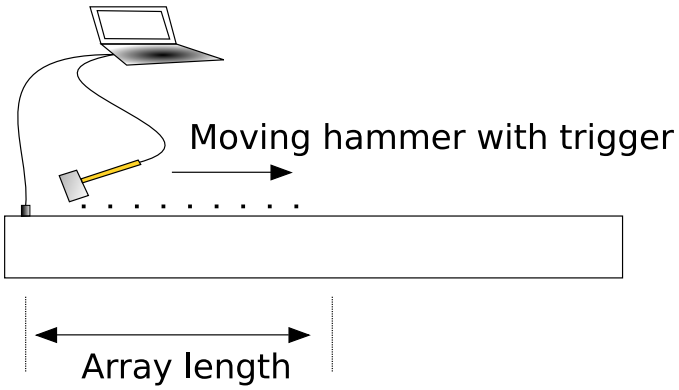

Figure 5.1: Sketch of measurement technique.

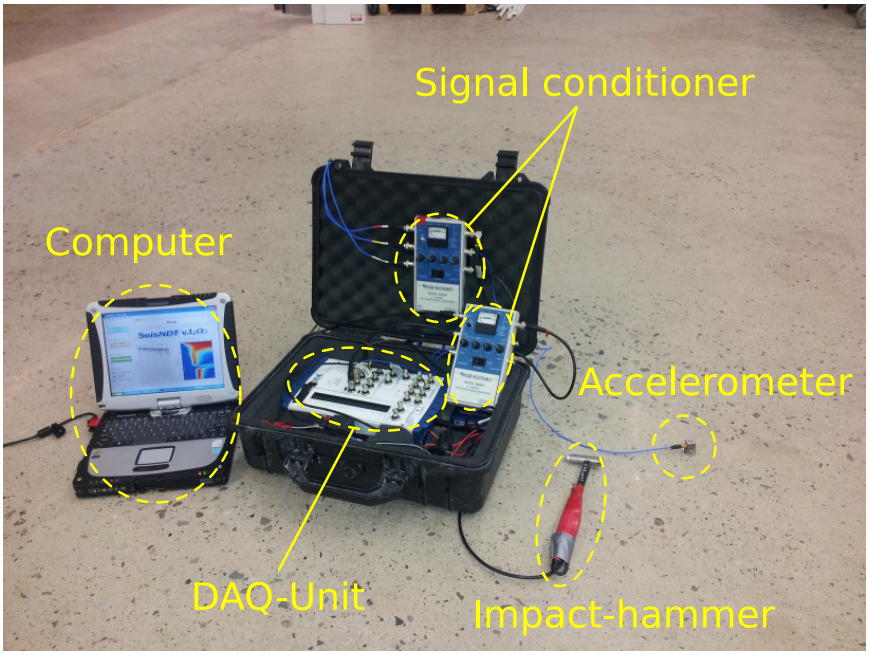

Figure 5.2: Measurement equipment: impact-hammer (PCB model 086C03), accelerometer (PCB model 339A30), signal conditioner (PCB model 480b21), DAQ-unit (NI USB-6251 BNC), and computer (Panasonic Toughbook).

An overview of the used measurement equipment is shown in Figure 5.2. Figure 5.3 shows an example of a three component accelerometer. As can be noticed, the measurement equipment represent a very portable and flexible system in which every individual part of equipment easily can be changed or replaced. For example, it is common to select impactor with respect to the object that is studied. If a thick structure is considered it is suitable to use a heavier impactor which can generate sufficient low frequencies in the impact pulse. On the contrary, if a thin structure is considered, it is suitable to use a lighter impactor which can generate sufficient high frequencies in the impact. An example of different impactors is shown in Figure 5.4.

Figure 5.3: Three component accelerometer (PCB model 339A30).

Figure 5.4: Impact hammers, from left: home-made impactor (screw/bolt) with piezoelectric crystal, hammer PCB model 086C03, hammer PCB model 086D05.

Chapter 6

Results

6.1 1D array measurements and analysis

Non-destructive techniques based on mechanical waves generated by transient impacts can be used to evaluate the thickness of plate-like concrete structures. Paper I provides increased knowledge about the reliability and uncertainties in such type of evaluations under the condition of one-sided access, i.e. the case in which only one side of the plate surface is accessible. More specifically, the investigation is focused on a combined technique based on multi-channel analysis of surface waves (MASW) and Impact-Echo (IE), see Paper I; this technique is denoted MASW/IE. In the current case, the MASW/IE technique uses the first thickness resonance of a plate (S1-ZGV) as well as the propagating surface wave field to enable a Lamb wave analysis. In addition, results are also compared with the conventional Impact-Echo (IE) method based on a simplified and interpretation of the wave behaviour, see Section 2.3.

The resonant vibration mode linked to the S1-ZGV Lamb mode as well as surface waves can be utilized to determine an unknown thickness as well as the elastic properties of a plate-like structure. Thus, Lamb wave theory plays an important role in impact-based evaluations of plate-like concrete structures and should therefore be taken into account for best possible results. In Lamb wave theory, a plate is defined by three independent parameters such as acoustic wave velocity, Poisson's ratio and thickness; in the following section and in Paper I, this represents an important basis used for non-destructive evaluation. As presented in Chapter 2, a systematic error in terms of underestimated plate thickness is reported in the literature. To study this error in more detail, the basis of the Lamb wave evaluation must be investigated; fundamentally, estimation of the elastic properties (acoustic wave velocity and Poisson's ratio) and thickness using Lamb waves is equiv-

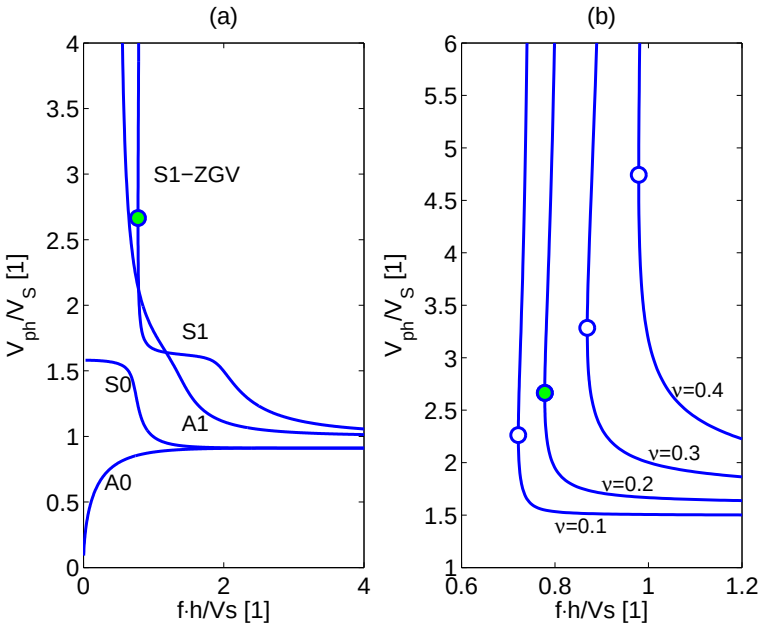

Figure 6.1: (a) Lamb wave dispersion curves (A0, S0, A1, and S1 mode) for a plate with $\nu = 0.2$. (b) Expanded view around the S1-ZGV point for different values of Poisson's ratio ν.

alent to determine the right set of Lamb wave dispersion curves associated with a plate. Here, note that since the Lamb wave plate parameters are coupled through the Lamb wave equation, the error in estimated thickness typically implies an error in an estimated elastic properties as well.

For plates in general, the dispersive nature of Lamb waves can be illustrated in many ways: one possibility is to present dispersion curves in the frequency-phase velocity domain. Here, the dispersion curves provide an important theoretical basis that facilitates the interpretation of how an unknown thickness for plate-like concrete structures can be estimated with Lamb waves. Figure 6.1 (a) shows a selection of the dispersion curves (Lamb modes A0, S0, A1, and S1) for a plate with Poisson's ratio $\nu = 0.2$. The axes are normalized with the thickness h and the transversal wave speed V_S. This normalization makes the curves only dependent on the Poisson's ratio ν, i.e. they are valid for all plates with $\nu = 0.2$. The S1-ZGV point, which represents the first through thickness resonance of a linear elastic isotropic plate, is also illustrated.

Figure 6.1 (b) shows an expanded view of the S1-ZGV point for different values of Poisson's ratio ν. Again, the normalized axes makes the location of the S1-ZGV point to be only dependent on ν. This implies that the value of fh/V_S, i.e. the normalized frequency and location on the x-axis, is constant

for the S1-ZGV point at a fixed value of ν. Thus, the normalized frequency fh/V_S provides a direct way to determine the plate thickness once V_S, ν, and f are known. However, in practice, the plate parameters V_S, ν and h are in most cases not directly accessible, and as a result, they must be determined indirectly using other parameters. In the investigated MASW/IE technique in Paper I, this is solved by a measurement of the longitudinal wave velocity V_P, the Rayleigh wave velocity V_R, and the frequency of the zero-group velocity (ZGV) point of the first symmetric (S1) Lamb mode f_{S1-ZGV}. These three quantities provide the necessary information to determine V_S, ν and h, and naturally, the accuracy of the obtained parameter estimates is therefore dependent on the accuracy of these input values (V_P, V_R and f_{S1-ZGV}) in the evaluation.

A detailed numerical finite element simulation mimicking the MASW/IE and IE measurement is performed to enable an investigation of the input values in the evaluation (i.e. V_P, V_R and f_{S1-ZGV}). A description of the simulation technique is given in Section 4.2. The simulation corresponds to the calculation of the dynamic response of a plate excited with a transient point load. Results from such simulation are shown in Figure 6.2(a) which displays the time history (y-axis) of the vibration response as function of radial offset position (thickness normalized) from the point source (x-axis). For both the combined MASW/IE and conventional IE technique, the longitudinal wave velocity V_P is generally estimated from the velocity of the first arriving wave. This velocity is often referred to as the first arrival velocity. An expanded view close to the impact source, see Figure 6.2(b), reveals that there exists a zone where the velocity of the first arriving (white dots marked First arrivals) wave cannot be directly linked to the theoretical longitudinal wave velocity (solid white line marked V_P). This zone, in which the high amplitude of the Rayleigh wave hides the longitudinal wave, results in an underestimated velocity, which in turn, leads to an uncertain estimation of Poisson's ratio and an underestimated thickness. The magnitude of the underestimated thickness is dependent on Poisson's ratio, pulse frequency content, and the distance between the measurement and the impact source.

For the MASW/IE technique, the velocity of the first arrival wave is calculated by adjusting a slope to the points corresponding to first arrivals seen in Figure 6.2(b) using linear regression. For the conventional IE technique, the first arrival velocity is also calculated by adjusting a slope, but with the difference that only two signals (traces) are used; this corresponds to the procedure described by the standardization of the IE technique (ASTM C 1383). Figure 6.3(a) and Figure 6.3(b) show the variation of estimated first arrival velocity for the combined MASW/IE technique and the conventional IE technique, respectively. Both Figure 6.3(a) and Figure 6.3(b) show that the estimated first arrival velocity is clearly affected by the near field: this leads to uncertainty in the estimation of plate thickness.

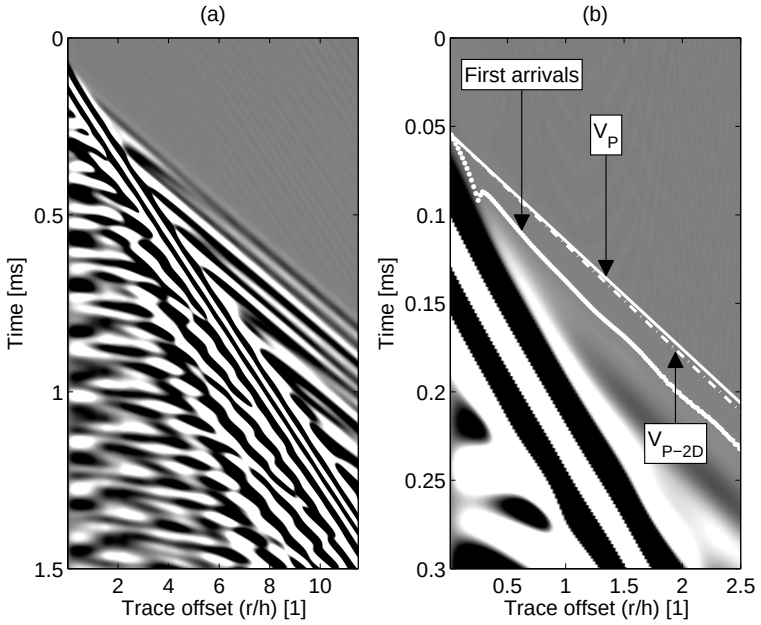

Figure 6.2: (a) Detailed finite element simulation of impact-echo and surface wave test. (b) Expanded view close to impact source showing traces/signals within a radial distance of $2.5 \cdot r/h$. First arrivals are marked with dots. Straight lines marked V_P and V_{P-2D} correspond to theoretical velocities of the longitudinal wave and low frequency component of the fundamental symmetric (S0) Lamb mode, respectively. The straight lines are aligned with the time point of the first picked arrival wave at $r/h = 0$.

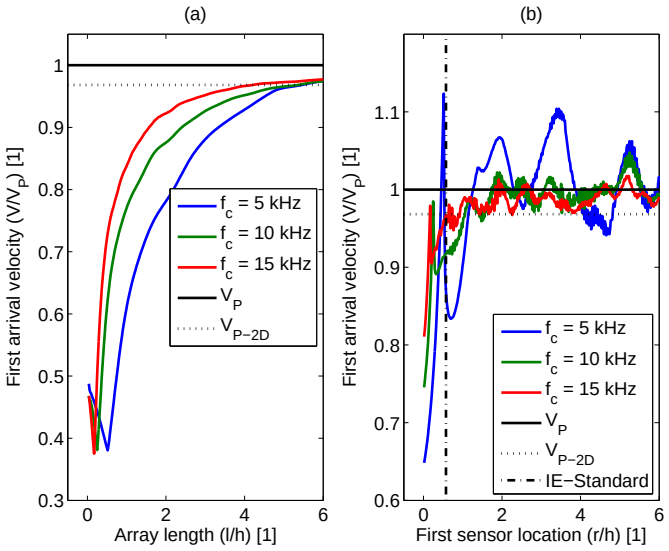

Figure 6.3: Variation of P-wave velocity estimated from first arrival in simulated data for (a) Combined MASW/IE technique (b) conventional IE technique.

To explore at which extent the observed variations in estimated first arrival velocity presented in Figure 6.3 can be observed in a real field case, an analysis of data recorded from a real measurement on a concrete cement plate cast on a granular base is performed. The variation of estimated first arrival velocity for the combined MASW/IE technique and the conventional IE technique is shown in Figure 6.4, respectively. From the results of this measurement, it can be observed that the longitudinal wave velocity estimated from the first arrivals increases with the array length (Figure 6.4(a)) or the location of the sensors (Figure 6.4(b)). This is in line with the general trend displayed by the results from the simulated case shown in Figure 6.3. Consequently, results from both simulations and measurements verify the inherently difficult and questionable task of estimating the longitudinal wave velocity V_P from the first arrivals of dispersive Lamb waves. That is, by following the recommendations in the standard ASTM C 1383 or the practice used in many applications, uncertainties in the estimated longitudinal wave velocity may arise depending on the plate properties and the impact source frequency content.

Except for the longitudinal wave velocity V_P, the Rayleigh wave velocity V_R and the frequency of the zero-group velocity (ZGV) point of the first symmetric (S1) Lamb mode f_{S1-ZGV} are also used in the evaluation of the Lamb wave plate parameters V_S, ν and h. Results from simulations and measurements show that the Rayleigh wave is also affected by near field

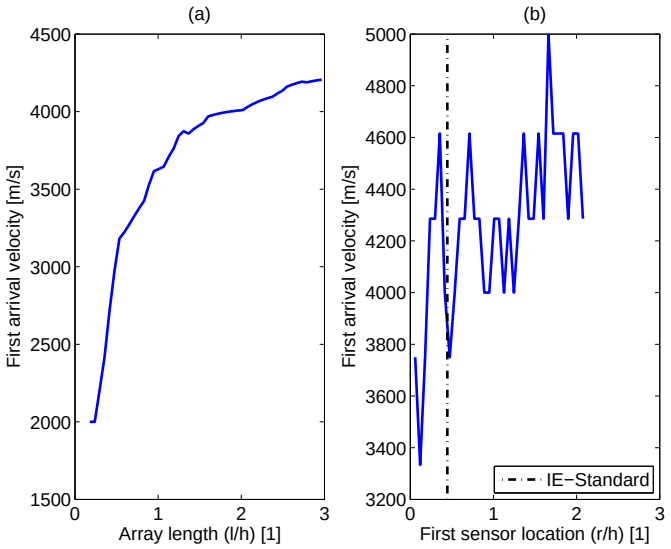

Figure 6.4: Variation of P-wave velocity estimated from first arrival in measurement data for (a) Combined MASW/IE technique (b) conventional IE technique.

effects; close to the impact source, a lower value of the estimated Rayleigh wave velocity is observed. However, the influence from this error is lower than the influence of the error from the estimation of the longitudinal wave using first arrivals. Moreover, simulations and measurements show that the S1-ZGV frequency in general is estimated with good accuracy with a non-significant dependency on the array length.

In total, the combined errors from the estimated longitudinal wave velocity and the Rayleigh wave velocity create a systematic error which underestimates the thickness in evaluations based on the MASW/IE and IE techniques with about 5-15 % depending on the Poisson's ratio, measurement set-up and source pulse. The major cause of this error is related to the interpretation of the first arrival velocity as a pure longitudinal wave velocity. Typically, for the MASW/IE technique, the underestimated longitudinal wave velocity causes an underestimated Poisson's ratio (estimated from the longitudinal wave velocity and the Rayleigh wave velocity) which in turn leads to an underestimated plate thickness. For the IE technique, the underestimated longitudinal wave velocity leads to an underestimated plate thickness through the evaluation of Eq. 2.1. Here, note that the alternative interpretation of the first arrival longitudinal wave velocity as the low frequency component of the fundamental symmetric (S0) Lamb mode (V_{P-2D} in Figure 6.2(b)) does not reduce this error.

Fortunately, the longitudinal wave velocity is not a requirement to enable

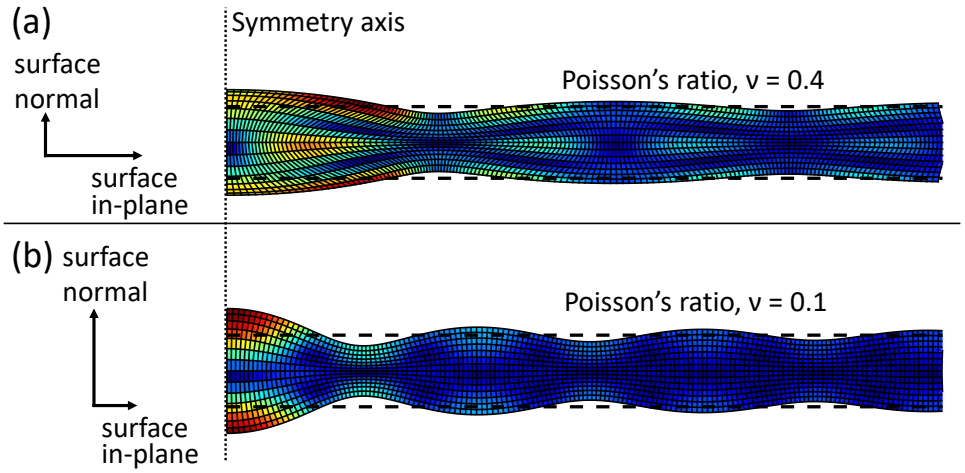

Figure 6.5: Mode shape, with cylindrical spreading due to a point load, of first symmetric zero-group velocity Lamb mode (S1-ZGV): (a) $\nu = 0.4$, (b) $\nu = 0.2$. The arrows exemplify the relative magnitude of the movement, i.e. they are not plotted in exact scale. Color scale corresponds to magnitude of displacement (i.e. both surface normal and surface in-plane component)

an estimation of the Lamb wave plate parameters (e.g. V_S, ν and h); the longitudinal wave velocity is just one alternative selection of an indirect parameter used as input in the evaluation of Poisson's ratio ν. Naturally, it is of interest to explore alternative approaches for estimation of Poisson's ratio ν which are not dependent on an evaluation of a longitudinal wave velocity from first arrival velocity. This represents the motivation for the work presented in Paper II, in which an alternative and new approach for estimation of Poisson's ratio is proposed. This approach is based on the amplitude polarization of the first symmetric zero-group velocity Lamb mode (S1-ZGV). Here, the amplitude polarization is interpreted as the ratio defined by the magnitude of the surface normal component divided by the magnitude of the surface in-plane component. This means that the approach does not require an estimation of the longitudinal wave velocity, e.g. from first arrivals as in Paper I; the longitudinal wave velocity is used to estimate Poisson's ratio together with the Rayleigh wave velocity.

The main idea of the approach is illustrated in Figure 6.5. Figure 6.5 shows the mode shape of the first symmetric zero-group velocity Lamb mode (S1-ZGV) for two values of Poisson's ratio ($\nu = 0.4$ and $\nu = 0.1$). The effect from cylindrical spreading, due to a point source excitation, is also taken into account in Figure 6.5, i.e. the spatial periodicity is defined by a Hankel function instead of an exponential function. For high Poisson's ratio, the

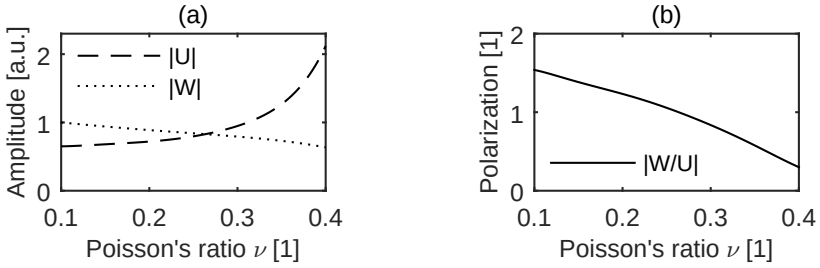

Figure 6.6: (a) Magnitude values of the surface in-plane component U and the surface normal component W of the S1-ZGV mode at the plate surface as function of Poisson's ratio ν. (b) Polarization $|U/W|$ of S1-ZGV mode as function of Poisson's ratio ν.

movement of the S1-ZGV mode shape *at the plate surface* is dominated by the surface in-plane component, see Figure 6.5 (a), whereas for low Poisson's ratio, the movement *at the plate surface* is dominated by the surface normal component, see Figure 6.5 (b). This phenomena is further illustrated in Figure 6.6(a) in which the magnitude of the surface in-plane component U and the surface normal component W is calculated for the S1-ZGV mode *at the plate surface*. The ratio defined by $|U/W|$, i.e. the amplitude polarization of the S1-ZGV mode shape, is only dependent on Poisson's ratio, see Figure 6.6(b). Once this ratio, i.e. the amplitude polarization of the S1-ZGV mode, is determined, the relationship displayed in Figure 6.6(b) provides an estimate of Poisson's ratio. In contrast to the approach based on a longitudinal wave velocity and Rayeleigh wave velocity (see Paper I), an advantage of using the polarization of the S1-ZGV Lamb mode is that a through-thickness representative estimation of Poisson's ratio is obtained, since the utilized Lamb mode (S1-ZGV) exists through the entire thickness of the plate.

The polarization based approach is tested in a practical measurement on a concrete wall in a bridge. A photograph of the bridge is shown in Figure 6.7(a). Figure 6.7(b) and Figure 6.7(c) show the test location on the wall and a close-up view of the accelerometer, respectively. Results from the evaluation of the measurement data collected from the bridge wall are shown in Figure 6.8. Figure 6.8(a) shows the absolute amplitude of the measured S1-ZGV Lamb mode (markers). A best match between the extracted mode shape (markers) and the theoretical mode shape (lines) is determined. In this case, the polarization $|W/U|$ is estimated to 1.09, and thereby, an estimate of Poisson's ratio $\nu = 0.24$ is obtained using the relationship presented in Figure 6.6(b).

In this field case, no exact value of ν is accessible directly for comparison. Nevertheless, the estimation of ν can be verified indirectly to a certain extent

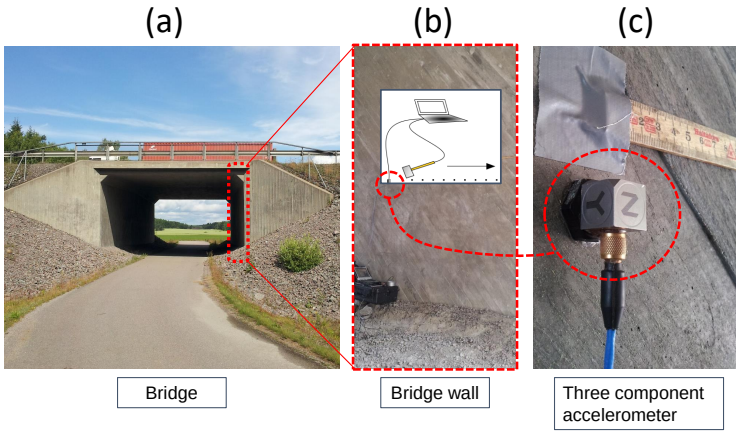

Figure 6.7: Photographs from a practical test of polarization approach. (a) Bridge test object. (b) Bridge wall. (c) Expanded view of accelerometer mounted on the bridge wall.

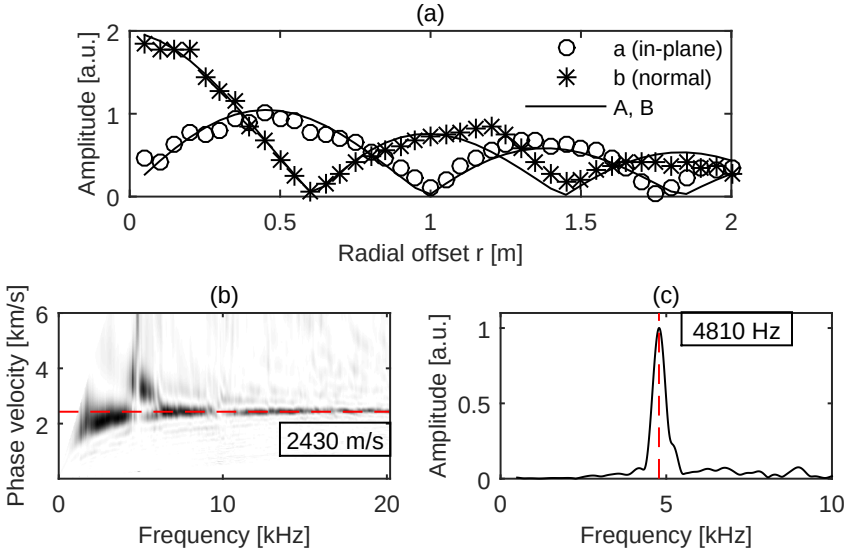

Figure 6.8: Evaluation of measurement data from practical test of the polarization approach. (a) Circle and asterisks markers: measured absolute values of the magnitude of the S1-ZGV Lamb mode. Solid lines: best fitted mode shaped to measurement data points. (b) Measurement data displayed in frequency-phase velocity domain. Red dashed line at 2340 m/s indicate estimated Rayleigh wave velocity. (c) Frequency spectrum of signal collected in vicinity of the accelerometer. Frequency peak at 4810 Hz corresponds to the S1-ZGV frequency.

from the nominal thickness of the bridge wall $h = 0.450$m. Estimation of the Rayleigh wave velocity (2430 m/s) from the raw signals displayed in frequency-phase velocity domain (Fig. 6.8(b)), the S1-ZGV frequency (4810 Hz) from the frequency spectrum of the signal nearest the impact point (Fig. 6.8(c)), and Poisson's ratio (0.24) theoretically corresponds to a thickness of 0.447 m, which is within 1% error of the nominal thickness (0.450 m). For comparison, the approach based on the longitudinal wave velocity yield an estimated thickness of 0.425 m (i.e. within 6% error of the nominal thickness). In this comparison, the same Rayleigh wave velocity (2430 m/s) and S1-ZGV frequency (4810 Hz) are used; the difference in estimated thickness between the two approaches is related to the value of Poisson's ratio $\nu = 0.18$ when the longitudinal wave velocity (4295 m/s) is estimated from first arrivals (not shown). In other words, in this field case the approach based on the polarization of the S1-ZGV Lamb mode provides an increased accuracy of the estimated nominal thickness in comparison with the traditional approach using the longitudinal wave velocity estimated from first arrivals.

6.2 2D array measurement and analysis

The work in both Paper I and Paper II is based on the study of data recorded with multiple impacts with equidistant spacing performed along a line; such data provides estimates that are representative for the region along the line. However, for improved knowledge and resolution of obtained estimates from evaluation techniques in the lateral plane of plates, it is of interest to not restrict the analyses to only a few points or a line in just one direction. However, there is no explicit requirement that prohibit the use of other layouts for data collections. For instance, layouts in form of grids are observed within the field of geophysics in studies of surface waves as well as in the general field of guided wave testing. Naturally, from the assumption of cylindrical spreading from a point source excitation, it is evident that the wave field is possible to study in all directions from the source location. This represent the motivation for the work in Paper III, in which a Lamb wave analysis technique for concrete plates with 2D-arrays is proposed. Since this technique uses data collected over a surface, a study of potential material variation and thickness along the lateral plane of the plate is possible. Compared to ultrasonic reflection imaging methods, this technique is not limited to a specific operating frequency (transducer) since it is based on a full wave field dataset with wide frequency bandwidth. Thus, the technique represent an important complement to current ultrasonic reflection imaging methods.

The 2D-array technique is demonstrated on a newly cast concrete slab that represent the ground floor and foundation in a future school. The nominal

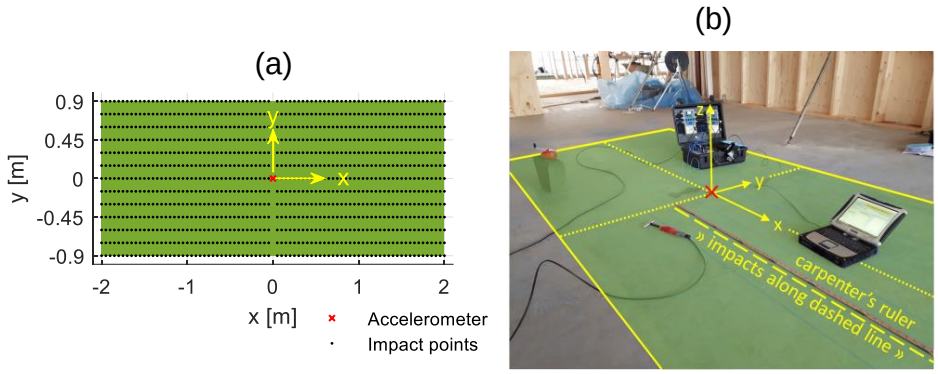

Figure 6.9: (a) Sketch of measurement domain with coordinate system. Black dots show locations of impacts and red-cross shows the location of the accelerometer, which is kept fixed throughout the measurement. (b) Photograph from measurement with illustration of surface domain in which data is collected.

thickness of the slab is 0.12 m. The measurement is carried out in a location with low influence from reflections caused by free slab edges. Also, since the plate is newly cast, a test condition without anomalies such as defects is anticipated; thus, this ideally implies uniform material properties and plate thickness. The selection of this location for the measurement is motivated with the aim of creating a controlled and reliable test environment without introducing excessive uncertainties from potential anomalies. Measurement data is collected within a rectangular domain with length 4 m and width 1.8 m, see Figure 6.9(a). Figure 6.9(a) shows the measurement domain with green colour and the associated coordinate system. Within this rectangular measurement domain, 1040 impacts are performed with locations according to the black dots. Throughout the measurement, the accelerometer is kept fixed at the centre of the rectangular domain (red cross). A photograph from the measurement is shown in Figure 6.9(b) along with illustration of the measurement domain and associated coordinate system. A practical aspect related to the measurement is also shown in Figure 6.9(b) by means of the highlighted dashed line and carpenter's ruler; the measurement is carried out by performing impacts along the dashed line, and then, moving the carpenter's ruler to a new location and repeating the process. Thus, the measurement may be interpreted as a series of measurements similar to that for instance used in multichannel analysis of surface waves (MASW, see Paper I). In the measurement, the impact hammer also works as a triggering

device. As a result, reciprocity can be used to create a dataset corresponding to a full wave field recorded with 1040 time-synchronized *synthetic* sensors located at the position of the impact points. Then, by creating subset of these 1040 sensors through smaller groups, spatial sensor arrays are created. Here, focus are directed to group of sensors extracted from limited two-dimensional surface regions of rectangular and circular shape. In the following, these group of sensors are referred to 2D-arrays; this naming is used to emphasize their relation to two-dimensional (2D) surface shapes.

Through the characteristics of cylindrical spreading and the assumption of relatively constant material and plate thickness within a limited surface region, data from 2D-arrays (group of sensors) can be studied with almost the same technique as arrays defined by sensors along a line. Practically, this is carried out by analysing the data in the radial offset domain. In the radial offset domain, the $x - y$ coordinate of each sensor is converted to a spatial radial coordinate r that measures the distance from the sensor to the source location (acquired from reciprocity) in the centre of the measurement domain (red cross in Figure 6.9). That is, the radial offset domain represents a polar domain defined by a radial axis directed outwards from the location of the source (red cross in Figure 6.9).

An example of a 2D-array defined by a rectangular shape is shown with blue diamond markers in Figure 6.10(a). This rectangular 2D-array is defined by the slope of 25° and the width of 0.3 m. In total, this 2D-array contains 85 sensor. The data collected by these 85 sensors are further studied in the radial offset domain. The surface-in plane acceleration response (parallel to the radial axis) for the 85 sensors within the rectangular 2D-array are shown in Figure 6.10(b). This seismic plot shows the time history of each recorded signal. The displayed signals are sorted according to their location along the radial axis r. With aim of suppressing high frequency noise, a low-pass filter is applied in time domain to reduce the frequency content above 30 kHz. In similarity to the data presented in Figure 6.2(a), it is possible to observe the first arrival longitudinal wave, surface waves as well as the stationary S1-ZGV Lamb mode. That is, data from this 2D-array displayed in radial offset domain exhibit the same general full wave field characteristic as data obtained from arrays in the form of lines.

The use of a seismic plot is an efficient tool that provides an overview of measurement data in both time and space. Thus, both velocity (slope in Figure 6.10(b)) and frequency (periodicity in Figure 6.10(b)) may be estimated. However, since the recorded wave field consists of multi-modal and dispersive Lamb waves present simultaneously over a wide frequency range, reliable estimations of velocity and frequency may be challenging to acquire from the data in this representation. For this reason, it is useful to study the data in frequency domain. For an estimation of the spectral content

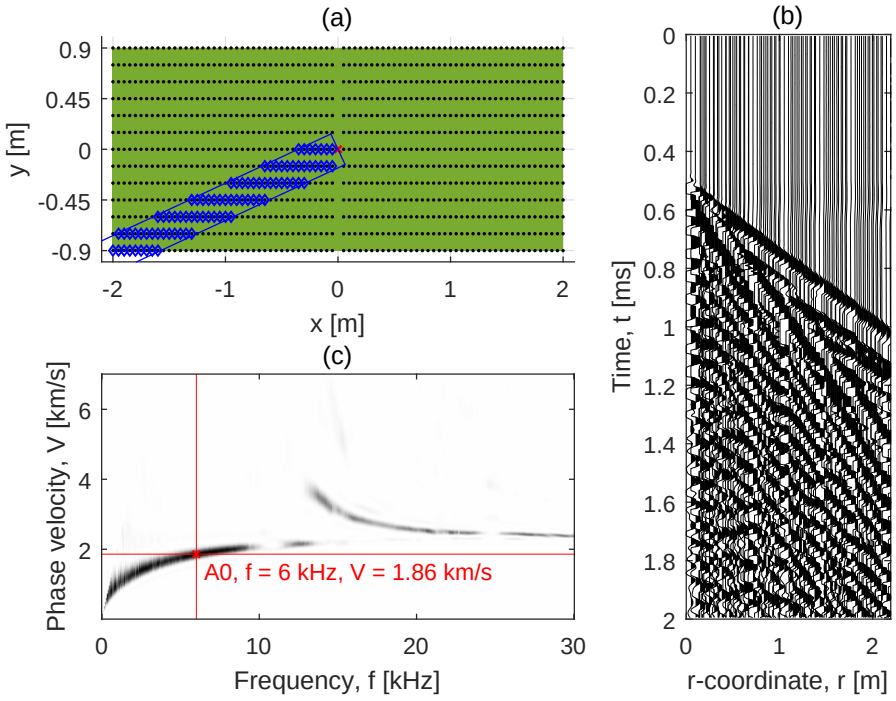

Figure 6.10: (a) Green rectangle: measurement domain. Black dots: sensors. Red cross: Source location. Rectangular 2D-array shown with blue diamond markers. (b) Low-pass filtered time domain data of surface in-plane (parallel to radial axis) acceleration response. (c) Frequency-phase velocity correlation image. Red cross shows the estimated phase velocity for A0 Lamb mode at 6 kHz.

of the recorded data from the 2D-array displayed in Figure 6.10(a), a two-dimensional Fourier transform is used to create an image that shows the spectral correlation for a range of frequency-phase velocity combinations. Such correlation image is shown in Figure 6.10(c). In Figure 6.10(c) the well-known pattern of the fundamental Lamb modes A0 and S0 is observed clearly (for instance, compare with Figure 3.6). This result ensures validity and strengthens the usefulness of 2D-arrays for Lamb wave evaluations performed in radial offset domain. Here, note that the processing that results in Figure 6.10(c) is essentially the same as that used in Paper I and Paper II; the difference is that a transformation of data into the radial offset domain must be performed at first.

Spectral estimations such as the one shown in Figure 6.10(c) can be used for analysis of the dispersive properties of the plate; this provides an indirect estimation of the material properties and thickness of the plate. For the 2D-array displayed with blue diamond markers in Figure 6.10(a), the estimated spectral content shown in the correlation image (Figure 6.10(c)) is representative for the surface region covered by the 2D-array. More specifically, the estimation represent a type of spatial average since the 2D-array can be interpreted as a spatial averaging operator dependent on the 2D-array surface size and shape. Nevertheless, since estimates as function of the region covered by the 2D-array are obtained, this can be utilized for monitoring of potential variation of material properties and thickness in the lateral plane of the plate. Accordingly, by estimating the dispersive properties at different locations of a plate, the homogeneity of a plate can be assessed.

Since the recorded data contains a full wave field response with a wide frequency bandwidth, an assessment of homogeneity may be focused on the full frequency range of the dispersive wave field. However, such analysis usually requires extensive work and may for this reason not be sensible for an initial assessment concerning homogeneity of a measurement object. Owing to this, it is reasonable to select one or a few modes at a narrow band of frequencies for the initial analysis of homogeneity. As example here, the A0 Lamb mode at the frequency 6 kHz is selected for further investigations. This mode is selected since its mode shape is present through the entire thickness of the plate. For this mode, the phase velocity is dependent on the material properties through the complete cross-sectional thickness. Moreover, the phase velocity is also dependent on the plate thickness. For the 2D-array shown in Figure 6.10(a), the estimated phase velocity for the A0 Lamb mode at 6 kHz is 1.86 km/s; this estimate is highlighted with a marking by the red cross in Figure 6.10(c). The wavelength of the A0 Lamb mode at 6 kHz is approximately $\lambda = V/f \approx 0.3$ m; by considering the wavelength λ in comparison with the nominal thickness (0.12 m) for the plate, it can be noticed that the mode is not expected to be sensitive for local material inhomogeneities such as reinforcement bars.

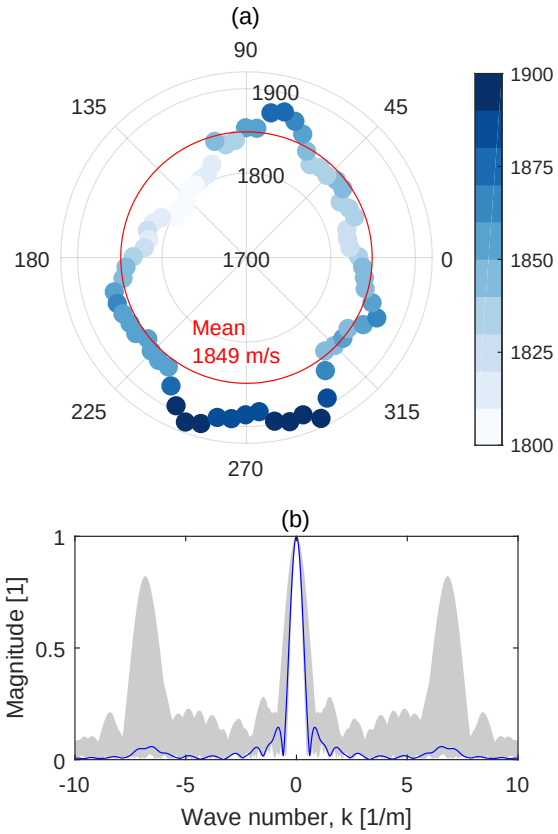

Figure 6.11: (a) Estimated phase velocity for the A0 Lamb mode at 6 kHz as function of polar angle for rectangular array shown in Figure 6.10(a). (b) Grey shading: envelope of normalized absolute value of the Fourier transform of the array window functions in frequency (wave number). Blue line represents the rectangular 2D-array in Figure 6.10(a).

Through a stepwise rotation of the 2D-array in Figure 6.10(a) around the measurement domain and at each step performing an estimation of the phase velocity as in Figure 6.10(c), the variation of phase velocity as function of polar angle can be mapped. For the A0 Lamb mode at 6 kHz, the result from such evaluation is shown in Figure 6.11(a). Results in Figure 6.11(a) show that an almost consistent phase velocity with little relative variation for the A0 Lamb mode at 6 kHz is observed. This verifies a homogeneous plate with essentially constant material and thickness within the studied measurement domain; this is expected since a newly cast plate is investigated. A slight difference in processing between line arrays and 2D-arrays exists. Usually, a uniform sampling in space domain is used for line arrays. However, for 2D-arrays this is usually not the case; typically a non-uniform sampling (sensor

spacing) is used. This aspect slightly changes the numerical implementation of the discrete Fourier transform that creates the frequency-phase velocity correlation image (e.g. Figure 6.10(c)). Furthermore, to ensure reliability of the obtained results, the influence from sampling should also be considered. This can be realized by studying the Fourier transform of the spatial window corresponding to the array. Figure 6.11(b) shows the Fourier transforms of the spatial array windows. The study of these curves is of value since sampling in space domain (here, by means of the spatial 2D-array) corresponds to a convolution in frequency domain between the array, represented by a boxcar window function, and the true spectrum.

A rectangular 2D-array is not the only alternative for mapping of variation in dispersive properties. Another possibility is to use circular 2D-arrays. Such example is shown in Figure 6.12(a) by means of a circular 2D array with the radius of 0.45 m. Instead of a rotation, the 2D-array is swept within a rectangular grid space given by 40 points along the x axis and 20 points along the y axis. At each grid point, an estimation of the phase velocity for the A0 Lamb mode at 6 kHz is performed following the same technique as previously. The result from this mapping of phase velocity is shown in Figure 6.12(c) as a two-dimensional image plot. In Figure 6.12(c), each pixel corresponds to the location of a grid point in which an estimation of phase velocity is performed. Although the colour is assigned individually for each pixel, note that this colour (estimation) should not be interpreted as a pointwise estimate of the phase velocity; the estimated phase velocity is representative for the complete surface covered by the 2D-array, i.e. the estimate may be interpreted as a spatial average within the 2D-array surface.

In similarity with Figure 6.11(a), Figure 6.12(c) shows an almost consistent phase velocity for the A0 Lamb mode at 6 kHz. This result further verifies that a condition of homogeneous material and plate thickness is present within the measurement domain. Moreover, Figure 6.12(c) also demonstrates that mapped variation of phase velocity can be illustrated in a two-dimensional image plot and thereby serve as one example of a tool for assessment of homogeneity. From a general perspective, results also demonstrates the possibility of performing a new (for plate-like concrete structures) type of imaging analysis based on propagating Lamb waves from a full wave field dataset with wide frequency bandwidth. Since only a light and portable equipment is required and that the measurement can be performed in fairly short amount of time, it is expected that this technique is an interesting and valuable complement to existing imaging techniques based on e.g. ultrasonic pulse echo and synthetic apertures.

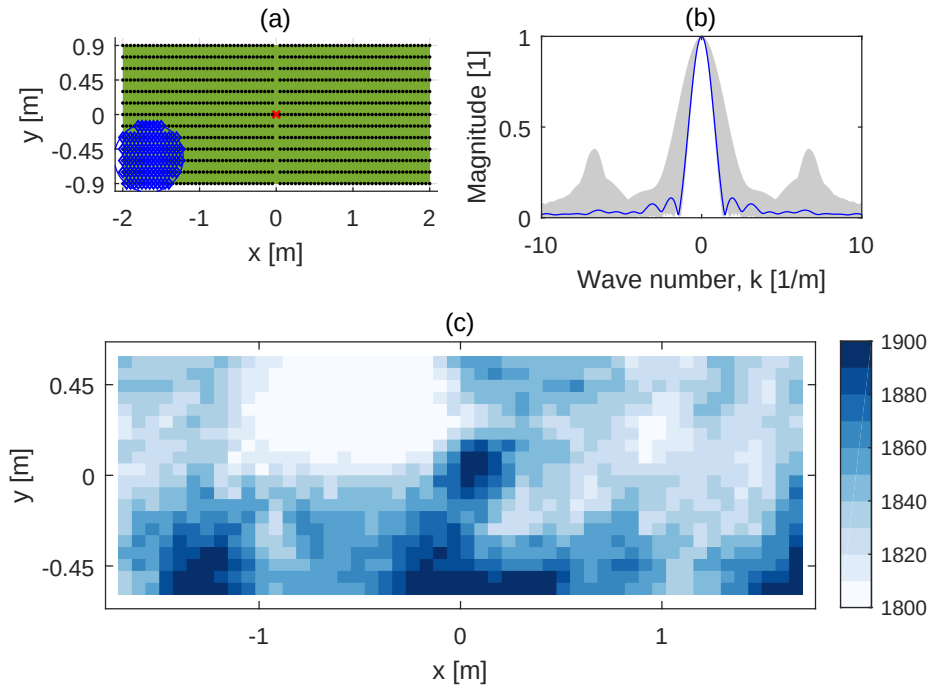

Figure 6.12: (a) Green rectangle: measurement domain. Black dots: sensors. Red cross: source location. Circular 2D-array shown with blue diamond markers. (b) Grey shading: envelope of normalized absolute value of the Fourier transform of the array window functions in frequency (wave number) domain. Blue line represents the circular 2D-array in top left sub-figure. (c) Estimated phase velocity for the A0 Lamb mode at 6 kHz as function of centre coordinate of circular 2D-array. Note that the pixels should not be interpreted as pointwise estimations due to the averaging effect from the 2D-array; the estimate is approximately representative to the region covered by the array.

6.3 Theoretical study inhomogeneous plates

In Paper I and Paper II, the presented work is based on the assumption of a homogeneous material in all directions for the complete domain of investigation; this assumption is implied from to the use of Lamb wave theory. The assumed condition of homogeneity is somewhat loosened in Paper III since a constant material and plate thickness is assumed only within a limited domain (the 2D-array); that is, homogeneity in the lateral plane of the plate is not assumed. However, as mentioned in Chapter 2, variations of the material properties *through* the thickness are observed for some concrete structures. Typically, such variations may manifest itself as a continuous variation of the acoustic bulk wave velocities. Such variations are in general not considered in testing of plate-like concrete structures with ZGV Lamb modes. This serves as the motivation for the work presented in Paper IV, in which the behaviour of the lowest (first) ZGV modes in two synthetic cases are investigated. In particular, important aspects of the investigation are whether a ZGV mode will appear, and if so, can it be detected with same robustness as for a homogeneous case, and also, how can the frequency of the ZGV mode be interpreted in relation to the material properties of the plate? To answer these questions, a semi-analytical finite element (SAFE) simulation as well as a conventional finite element simulation are performed.

The two cases, referred to as case 1 and case 2, are defined by two plates with inhomogeneous and non-symmetric continuous variation of the acoustic bulk wave velocities. Both cases are modifications of an isotropic reference case, which is represented by a linear elastic isotropic plate. Then, by the usage of two scaling functions, one for each case, the cases 1 and 2 are created by adjusting the acoustic bulk wave velocities (longitudinal wave velocity V_L and transversal wave velocity V_T) according to a scaling function with spatially varying amplitude along the plate thickness coordinate z. The scaling functions for cases 1 and 2 are shown in Figure 6.13(a) and Figure 6.13(b), respectively. The corresponding variations in the longitudinal and transversal wave velocities as function of the thickness coordinate for cases 1 and 2 are shown in Figure 6.13(c) and Figure 6.13(d), respectively.

It should be noted that cases 1 and 2 represent one selection among many potential candidate material variation cases; in fact, an infinite number of material variation cases exist, and naturally it is necessary to limit these cases. Cases 1 and 2 are selected to enable a study of ZGV modes in plates with a continuous inclusion of material with either high or low acoustic bulk wave velocities. It is anticipated that many concrete structures with one simple anomaly fall within the boundary limits formed by the definitions of cases 1 and 2 since these represent a fairly strong change in the acoustic velocities. Thus, it is expected that observed qualitative and quantitative re-

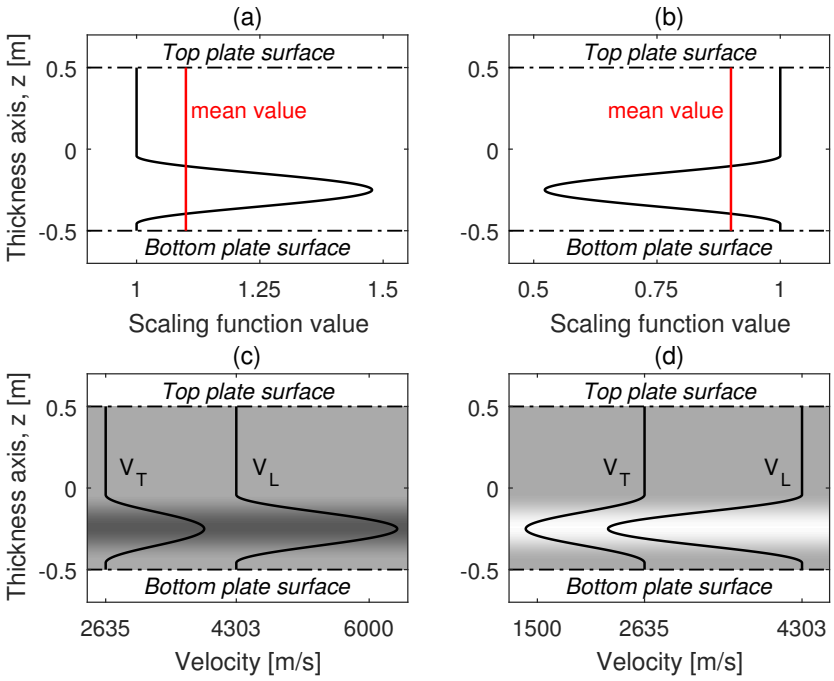

Figure 6.13: Scaling function for (a) case 1 and (b) case 2. The cases are characterised by a continuous variation of acoustic bulk wave velocities for. Cases 1 and 2 are show in (c) and (d), respectively. Cases 1 (c) and 2 (d) are created from a homogeneous isotropic reference case defined by a longitudinal wave velocity $V_L = 4303\,\mathrm{m/s}$, a transversal wave velocity $V_T = 2635\,\mathrm{m/s}$ (Poisson's ratio $\nu = 0.2$), and density $\rho = 2400\,\mathrm{kg/m^3}$ and the scaling functions in (a) and (b); by adjusting the acoustic bulk wave velocities (V_L and V_T) according to the scaling functions, cases 1 (c) and 2 (d) are created.

sults can be considered as valuable and relevant for other plate-like concrete structures as well.

The dispersion relations (curves) for cases 1 and 2 are calculated using a semi-analytical finite element (SAFE) model. Figure 6.14(a) and Figure 6.14(b) show the dispersion curves for the four lowest modes, denoted M1-M4, for the cases 1 and 2, respectively. For both cases, Figure 6.14 shows that the overall pattern exhibited by the M1-M4 modes is similar to the pattern exhibited by the A0, S0, A1, and S1 Lamb modes for the isotropic reference plate (dotted black lines). In similarity with the S1 dispersion curve for the isotropic reference case, Figure 6.14 shows that the M4 mode exhibit minimum points at a nonzero wave number. These minimum points represent modes at which the group velocity vanishes according to $V_g = df/dk = 0$; i.e., ZGV modes are observed also for cases 1 and 2. In the following, these modes (points) are referred to as M4-ZGV. However, although similarities exist between the M4-ZGV mode and the S1-ZGV, the cases 1 and 2 represent a condition with a complex relation between mode frequency and acoustic material velocity. In contrast to the isotropic case (Lamb waves), no simple relation between mode frequency and acoustic velocity exists. This condition of additional complexity compared to the isotropic case may lead to uncertainties in practical applications. For example, if an isotropic Lamb wave model is assumed under the actual condition of case 1 or 2, then the estimated acoustic material velocity or plate thickness from the M4-ZGV mode will be difficult to interpret since it is not representative to a mean value or other similar established quantitative measure.

To further study the M4-ZGV mode, the excitability is calculated. Figure 6.15(a) and Figure 6.15(b) show the excitability for the M1-M4 mode for cases 1 and 2, respectively. Figure 6.15(a) and (b) show that the M4 curve for both cases 1 and 2 exhibit high values of excitability around the M4-ZGV mode frequency. This is similar with the behaviour observed for S1 Lamb mode of the isotropic reference case. This means that high displacement amplitudes, in the form of a local resonance of the plate, are to be expected at the top plate surface even in for cases 1 and 2 by means of the M4-ZGV modes. The robustness and detectability of the M4-ZGV mode frequency is further studied in a simulation of a combined impact-echo and surface wave measurement; that is, this simulation corresponds to the applications in for example Paper I and Paper II. Results from this simulated application are shown in Figure 6.16(a) and (c), which shows the acceleration response as function of time at different radial offset distances to the hammer impact for cases 1 and 2, respectively. The time domain datasets are transformed to wave number frequency domain using a two-dimensional discrete Fourier transform. Figure 6.16(b) and (d) show the simulated response in presented in wave number frequency domain for the cases 1 and

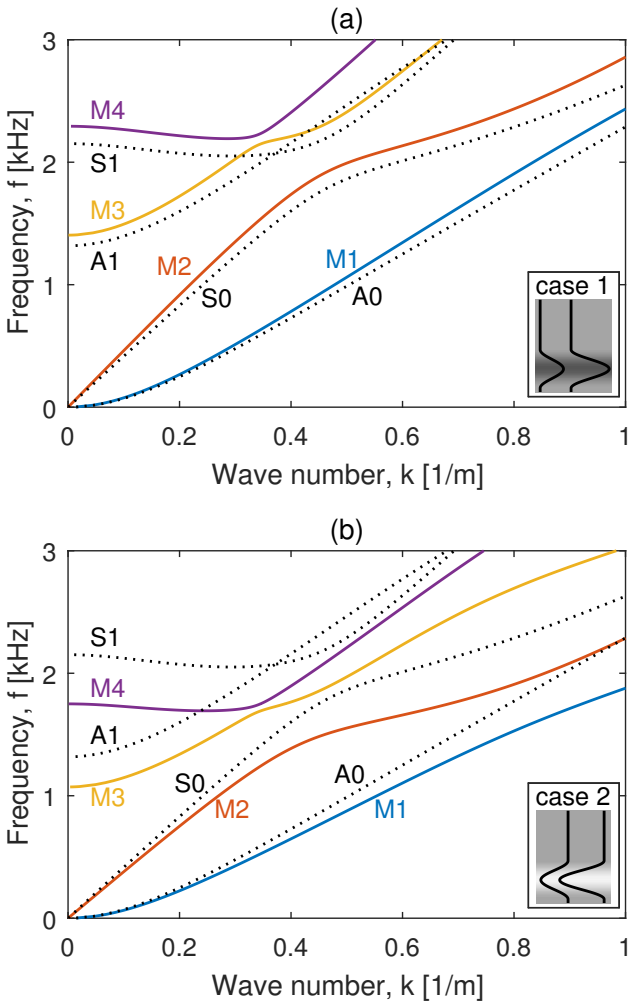

Figure 6.14: Dispersion curves for the four lowest modes M1-M4 for (a) case 1 and (b) case 2. The four lowest modes (A0, S0, A1, S1) for the isotropic reference case is shown with black dotted lines.

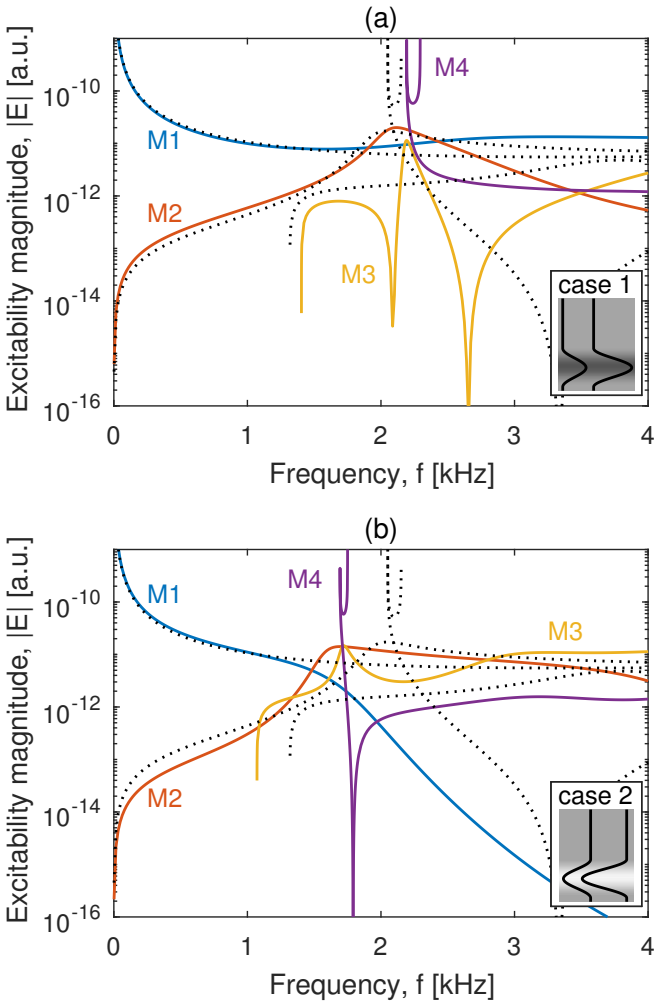

Figure 6.15: Excitability for (a) case 1 and (b) case 2. Solid lines in colour (M1-M4) represent the four lowest modes for cases 1 and 2. Dotted black lines show isotropic reference case. Here, excitability is interpreted as the displacement magnitude at the top surface of the plate in the surface normal direction, caused by a unit point load applied at the same point and direction. The excitability is calculated according to $E = i\omega|U|^2/(4P)$, where ω is the angular frequency, U is the surface normal displacement at the top surface of the plate, and P is the one-period time and cross-section-averaged Poynting vector component in the propagation direction of the mode.

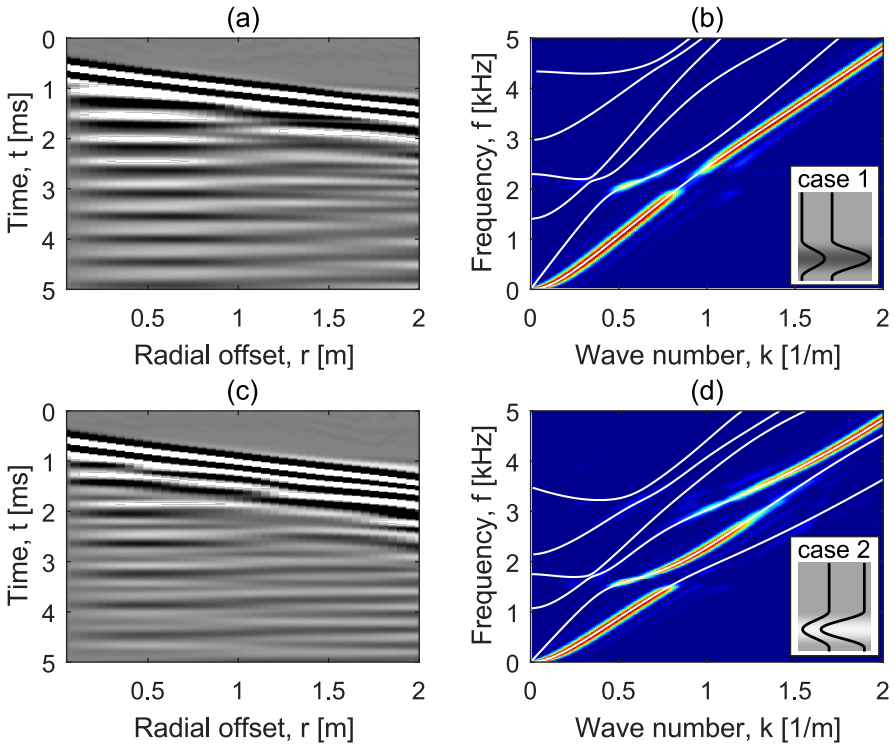

Figure 6.16: Simulated datasets for (a) case 1 and (c) case 2. Estimation of wave number-frequency content for (b) case 1 and (d) case 2 calculated using a 2D discrete Fourier transform. Superimposed dispersion curves from the SAFE analysis are shown as solid white lines.

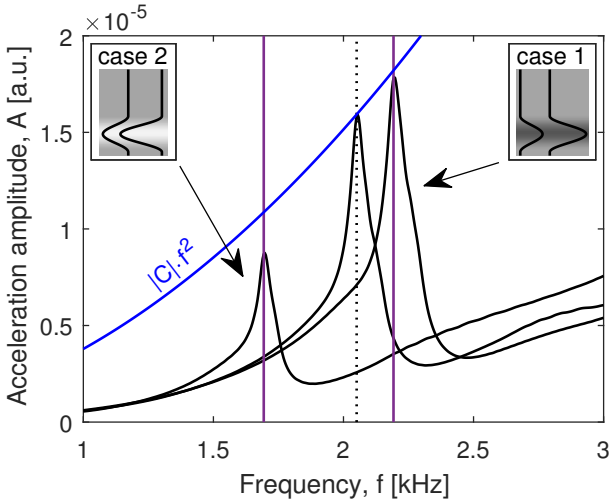

Figure 6.17: Discrete Fourier transform of summed acceleration response signals within 1 m distance from the impact source for case 1, case 2, and the isotropic reference case. Observed left and right peaks correspond to the M4-ZGV mode for cases 2 and 1, respectively. Middle peak corresponds to the S1-ZGV Lamb mode. The vertical lines indicate the predicted ZGV frequencies from the SAFE analysis; a good agreement is observed.

2, respectively. Figure 6.16(b) and (d) also show superimposed dispersion curves from the SAFE analysis as solid white lines. A good agreement between the dispersion curves and the dataset is observed for both cases; this serves as a verification of the correctness of the dispersion curves from the SAFE analysis. For cases 1 and 2, a differentiation of surface wave mode at high frequency is observed: the surface wave at high frequency is related to the M1 mode for case 1 and to the M3 mode for case 2, see Figure 6.16(b) and (d). This behaviour appears since the regions near the top and bottom surfaces are exposed to different mechanical properties (acoustic bulk wave velocities). If this behaviour is unknown or not considered, uncertainty and error in data evaluation may arise.

To study the detectability of the M4-ZGV mode for cases 1 and 2 in this simulated application, a discrete Fourier transform is calculated for the signals in vicinity of the impact source. Here, to facilitate identification of the M4-ZGV mode frequency by reducing the influence from propagating modes, the DFT is calculated on a summation of the signals within a radial distance of 1 m from the source. The absolute value of the spectrum from this calculation is shown in Figure 6.17. For reference, the frequencies corresponding to the M4-ZGV mode and the S1-ZGV Lamb mode from the SAFE analysis are marked with vertical lines: a good agreement can be observed for all cases. Figure 6.17 shows that the M4-ZGV mode materi-

alizes as a resonance with high amplitude at a distinct frequency, similar to the S1-ZGV Lamb mode. This is in line with the expected behaviour from the high modal excitability displayed in Figure 6.15. A slight variation in amplitude of the M4-ZGV mode between the cases is observed, which is expected to be dependent on at least two reasons. First, for a constant absolute displacement amplitude $|C|$ in frequency domain, the corresponding absolute acceleration amplitude is given by a quadratic parabola $|C|f^2$, see parabola in Figure 6.17. This makes the acceleration magnitude to increase with frequency for a constant displacement amplitude in frequency domain. Second, the top surfaces of the M4-ZGV mode for cases 1 and 2 are exposed to different material properties; this creates a slightly distorted modal shape compared to the S1-ZGV Lamb mode, and for this reason a variation in acceleration magnitude is generated between the cases. Still, the frequency of the peaks corresponding to the M4-ZGV mode is detected with the same robustness and accuracy as for the S1-ZGV Lamb mode. Nevertheless, results show that in this practical nondestructive application, ZGV modes can be used even for cases 1 and 2. It is expected that this result can be extended and generalized to other inhomogeneous plates that are within the boundary limits or similar to cases 1 and 2. Yet, since material variation typically leads to increased complexity in the relation between mode frequency and material properties, uncertainties in estimations may, depending on the magnitude of the inhomogeneity, occur.

Chapter 7

Conclusions

Near field effects lead to a systematically underestimated plate thickness in both conventional impact-echo testing and combined impact-echo and surface wave analysis of plate-like concrete structures. A main source of uncertainty is the interpretation of the first arrival wave velocity as the true longitudinal wave velocity. Alternative approaches for estimation of Poisson's ratio that are independent on the evaluation of first arrivals are therefore important. The proposed technique for estimation of Poisson's ratio based on the amplitude polarization of the S1-ZGV Lamb mode is one example of such approach. Unlike the cases when modes with different volume sensitivity are used, an estimate of Poisson's ratio representative for the complete plate cross-sectional thickness is obtained since the S1-ZGV Lamb mode is present through the entire plate thickness. For this approach applied in a practical measurement, an improved estimate of the nominal thickness is obtained compared to the case when Poisson's ratio is estimated from first arrivals.

A Lamb wave phase velocity imaging technique based on 2D arrays created from limited subdomains within the global measurement domain is presented with a measurement on a newly cast concrete plate as illustrating example. The novel aspect of this technique is the study of *propagating* waves in limited sub domains defined by the 2D arrays. Compared to conventional ultrasonic reflection imaging techniques, the 2D array technique is not limited to specific operating frequencies (transducers) since it is based on a full wave field dataset with wide-band frequency content. The technique operates at a lower frequency compared to ultrasonic approaches and is therefore expected to give a larger possible investigated volume and depth of penetration; this can be beneficial in evaluations of thick plate-like concrete structures. The 2D arrays are in this case used to map the variation of the phase velocity for the A0 Lamb mode. Results show a low variation of

the estimated phase velocity; this verifies the condition of a relatively homogeneous material and plate thickness in the measurement domain. Whereas the proposed 2D array technique is applicable for monitoring of variations in the lateral plane of a plate, results in the literature report that material variation may also exist transversally through the thickness of concrete structures. For this reason, a theoretical study is conducted to improve the understanding of non-destructive evaluation techniques based on zero-group velocity (ZGV) modes. Limited to a study of the lowest zero-group velocity mode, two cases with material variation through the plate thickness are investigated using a semi-analytical finite element (SAFE) model and a simulated non-destructive application. It is found that for both material variation cases a ZGV mode similar to the S1-ZGV for homogeneous plates exists. The detectability and robustness of this ZGV mode is found to be comparable and similar to the S1-ZGV for homogeneous plates. That it is, evaluation techniques utilizing the lowest ZGV mode are applicable also for these two material variation cases.

Chapter 8

Suggestions for further work

The measurements in this thesis (Paper I, Paper II and Paper III) are performed on a limited number of test sites and with the maximum plate thickness of 0.5 m. Given the aim and objective of this thesis, see Section 1.3, it is of importance to investigate the applicability at more test sites which preferably should be thick (>1 m) plate-like concrete structures. Such studies may also, for instance, include investigations of sensitivity for boundary effects for the amplitude polarization technique (Paper II) and exploration of mode sensitivity for defects or anomalies for the 2D array technique (Paper III).

Results in Paper I show that near-field effects and the estimation of longitudinal wave velocity from first arrivals may influence evaluations based on point-source excitation from e.g. hammer impacts. Although these results provide a step towards increased understanding of the wave-field behaviour, a full interpretation and explanation of these effects still remains an unsolved matter (according to the author). For further investigations of near-field effects it is anticipated that simulations using semi-analytical finite element models (see Paper IV) may be useful in this process. However, to the author's experience an implementation outside the FE-code of COMSOL (COMSOL Inc., 2016) would in such cases be useful for improved flexibility and control. This is related to that the implementation of a SAFE simulation in COMSOL implies a translation/transformation of the SAFE matrix expressions to a general eigenvalue equation form (Predoi et al., 2007).

The new approach for estimation of Poisson's ratio based on the amplitude polarization of the S1-ZGV Lamb mode proposed in Paper II highlights the potential of multicomponent measurements. For future work it is suggested that focus may be directed on extracting more information from such multicomponent measurements; for instance, in a related publication (Baggens and Ryden, 2015c), results show that the A2-ZGV Lamb mode can be identified by analysing the surface-in plane response. Here, it is anticipated that

an investigation (e.g. using semi-analytical finite element simulations) of the A2-ZGV Lamb mode in more detail could be useful for improved understanding. Another prospective alternative for further studies could be to investigate the phase aspect between the surface in-plane and surface normal component.

The 2D array technique presented in Paper III is demonstrated on a newly cast and ideally homogeneous plate. For further investigations it is important to study the applicability of the technique in cases with potential anomalies and defects. Moreover, the 2D arrays are based on data recorded in a rectangular grid. It is emphasized that this rectangular grid is not a condition required to enable 2D arrays. Sparse impact locations at arbitrary positions works equally well in this technique; the important matter is that the location of an impact (signal) must be known, but the exact location of the impact itself is not the critical aspect. Consequently, the 2D array technique would benefit greatly by developing a system that can locate the position of the hammer impact when the impact is performed; i.e. the opposite from the case in Paper III where the impact is performed at the pre-defined location by a marking. Another idea for further developments of 2D arrays concerns imaging in the transversal plane of the plate, e.g. see the SAFT images from synthetic impact-echo data in (Schubert and Köhler, 2008; Ganguli et al., 2012).

It is expected that developments concerning the measurement equipment used in this thesis may be possible. For instance, implementation of wireless devices is one such example. Moreover, the concept of air-coupled source generation and detection is also one alternative. Another interesting alternative is to study the possibility of using augmented reality devices. For instance, eye-glasses for augmented reality and digital image processing techniques could be one alternative approach for providing an operator with direct instructions and feedback in the practical execution of non-destructive measurements.

Chapter 9

Bibliography

O. Abraham, C. Leonard, P. Cote, and B. Piwakowski. Time frequency analysis of impact-echo signals: numerical modeling and experimental validation. *ACI Materials journal*, (97):645–657, 2000. DOI: 10.14359/9978.

O. Abraham, J. S. Popovics, and L.-M. Cottineau. Modification of the zero group velocity (impact echo) resonance frequency in the presence of voids for the inspection of tendon ducts. In *AIP Conference Proceedings*, volume 1365, pages 1365–1370, 2011. DOI: 10.1063/1.3592091.

O. Abraham, B. Piwakowski, G. Villain, and O. Durand. Non-contact, automated surface wave measurements for the mechanical characterisation of concrete. *Construction and Building Materials*, 37:904–915, 2012. ISSN 09500618. DOI: 10.1016/j.conbuildmat.2012.03.015.

J. D. Achenbach. *Wave Propagation in Elastic Solids*. North-Holland Publishing Company, 1973.

D. Algernon and H. Wiggenhauser. Impact Echo Data Analysis Based on Hilbert-Huang Transform. *Transportation Research Record*, 2028(-1):146–153, dec 2007. ISSN 0361-1981. DOI: 10.3141/2028-16.

D. Alleyne and P. Cawley. A two-dimensional Fourier transform method for the measurement of propagating multimode signals. *The Journal of the Acoustical Society of America*, 89(3):1159–1168, mar 1991. ISSN 0001-4966. DOI: 10.1121/1.400530.

H. Almansouri, C. Johnson, D. Clayton, Y. Polsky, C. Bouman, and H. Santos-Villalobos. Progress implementing a model-based iterative reconstruction algorithm for ultrasound imaging of thick concrete. *AIP Conference Proceedings*, 1806, 2017. ISSN 15517616. DOI: 10.1063/1.4974557.

ASTM C 1383. Standard Test Method for Measuring the P-Wave Speed and the Thickness of Concrete Plates Using the Impact-Echo Method, Annual Book of American Society for Testing and Materials (ASTM) Standards.

B. Auld. *Acoustic Fields and Waves in Solids, Vol. II*. Robert E. Krieger Publishing Company, Malabar, Florida, 2nd edition, 1990.

O. Baggens and N. Ryden. Systematic errors in Impact-Echo thickness estimation due to near field effects. *NDT & E International*, 69:16–27, jan 2015a. ISSN 09638695. DOI: 10.1016/j.ndteint.2014.09.003.

O. Baggens and N. Ryden. Near field effects and estimation of Poisson's ratio in impact-echo thickness testing. In *41st annual Review of Progress in Quantitative Non-Destructive Evaluation*, volume 34, pages 1415–1422, 2015b. ISBN 9780735412927. DOI: 10.1063/1.4914757.

O. Baggens and N. Ryden. Lamb Wave Plate Parameters from Combined Impact-Echo and Surface Wave Measurement. In *Non-Destructive Testing in Civil Engineering (NDT-CE 2015)*, pages 30–38, Berlin, Germany, 2015c. NDT.net. ISBN 4646222000.

O. Baggens and N. Ryden. Poisson's ratio from polarization of acoustic zero-group velocity Lamb mode. *The Journal of the Acoustical Society of America*, 138(1):EL88–EL92, jul 2015d. ISSN 0001-4966. DOI: 10.1121/1.4923015.

C. L. Barnes and J.-F. Trottier. Hybrid analysis of surface wavefield data from Portland cement and asphalt concrete plates. *NDT & E International*, 42(2):106–112, mar 2009. ISSN 09638695. DOI: 10.1016/j.ndteint.2008.10.003.

I. Bartoli, A. Marzani, F. Lanza di Scalea, and E. Viola. Modeling wave propagation in damped waveguides of arbitrary cross-section. *Journal of Sound and Vibration*, 295(3-5):685–707, 2006. ISSN 0022460X. DOI: 10.1016/j.jsv.2006.01.021.

A. Bayon, F. Gascon, and F. J. Nieves. Estimation of dynamic elastic constants from the amplitude and velocity of Rayleigh waves. *The Journal of the Acoustical Society of America*, 117(6):3469–3477, 2005. ISSN 00014966. DOI: 10.1121/1.1898663.

L. Bodet, O. Abraham, and D. Clorennec. Near-offset effects on Rayleigh-wave dispersion measurements: Physical modeling. *Journal of Applied Geophysics*, 68(1):95–103, may 2009. ISSN 09269851. DOI: 10.1016/j.jappgeo.2009.02.012.

D. Boiero, P. Bergamo, R. B. Rege, and L. V. Socco. Estimating surface-wave dispersion curves from 3D seismic acquisition schemes : Part 1 — 1D models. *Geophysics*, 76(6):G85–G93, 2012. ISSN 00168033. DOI: 10.1190/geo2011-0124.1.

A. Boyd and C. Ferraro. Effect of curing and deterioration on stress wave velocities in concrete. *Journal of materials in civil engineering*, (April): 153–158, 2005. DOI: 10.1061/(ASCE)0899-1561(2005)17:2(153).

J. Bungey, S. Millard, and M. Grantham. *Testing of Concrete in Structures*. Taylor & Francis, Abingdon, 4 edition, 2006. ISBN 978–0–415–26301–6.

M. Castaings, C. Bacon, B. Hosten, and M. V. Predoi. Finite element predictions for the dynamic response of thermo-viscoelastic material structures. *The Journal of the Acoustical Society of America*, 115(3):1125–1133, 2004. ISSN 00014966. DOI: 10.1121/1.1639332.

M. Cees, D. Clorennec, D. Royer, and C. Prada. Edge resonance and zero group velocity Lamb modes in a free elastic plate. *The Journal of the Acoustical Society of America*, 130(2):689–94, aug 2011. ISSN 1520-8524. DOI: 10.1121/1.3607417.

M. Cès, D. Clorennec, D. Royer, and C. Prada. Thin layer thickness measurements by zero group velocity Lamb mode resonances. *The Review of scientific instruments*, 82(11):114902, nov 2011. ISSN 1089-7623. DOI: 10.1063/1.3660182.

M. Cès, D. Royer, and C. Prada. Characterization of mechanical properties of a hollow cylinder with zero group velocity Lamb modes. *The Journal of the Acoustical Society of America*, 132(1):180–5, jul 2012. ISSN 1520-8524. DOI: 10.1121/1.4726033.

D. Clorennec, C. Prada, and D. Royer. Local and noncontact measurements of bulk acoustic wave velocities in thin isotropic plates and shells using zero group velocity Lamb modes. *Journal of Applied Physics*, 101(3): 034908, feb 2007. ISSN 0021-8979. DOI: 10.1063/1.2434824.

COMSOL Inc. COMSOL Multiphysics (r), 2016. URL `http://www.comsol.com`.

X. Dai, J. Zhu, and M. R. Haberman. A focused electric spark source for non-contact stress wave excitation in solids. *Journal of the Acoustical Society of America*, 134(6, 1):EL513–EL519, 2013. ISSN 0001-4966. DOI: 10.1121/1.4826913.

J. A. Deacon, C. L. Monismith, and J. T. Harvey. Pay Factors for Asphalt-Concrete Construction: Effect of Construction Quality on Agency Costs.

Technical report, Pavement Research Center, Institute of Transportation Studies, University of California, Berkeley, 1997.

J. Ditri, A. Pilarski, B. Pavlakovic, and J. Rose. Generation of guided waves in a plate by axisymmetric normal surface loading. *Review of Progress in Quantitative Nondestructive Evaluation*, 13A, 1994.

A. Ganguli, C. M. Rappaport, D. Abramo, and S. Wadia-Fascetti. Synthetic aperture imaging for flaw detection in a concrete medium. *NDT and E International*, 45(1):79–90, 2012. ISSN 09638695. DOI: 10.1016/j.ndteint.2011.09.004.

A. Garbacz, T. Piotrowski, L. Courard, and L. Kwaśniewski. On the evaluation of interface quality in concrete repair system by means of impact-echo signal analysis. *Construction and Building Materials*, 134:311–323, mar 2017. ISSN 09500618. DOI: 10.1016/j.conbuildmat.2016.12.064.

A. Gibson. *Advances in Nondestructive Testing of Concrete Pavements*. Ph.d. thesis, University of Illinois, 2004.

A. Gibson and J. S. Popovics. Lamb Wave Basis for Impact-Echo Method Analysis. *Journal of Engineering Mechanics*, 131(4):438–443, apr 2005. ISSN 0733-9399. DOI: 10.1061/(ASCE)0733-9399(2005)131:4(438).

K. F. Graff. *Wave Motion in Elastic Solids*. Dover Publications, New York, 1975. ISBN 0-486-66745-6.

M. Grohmann, E. Niederleithinger, and S. Buske. Geometry determination of a foundation slab using the ultrasonic echo technique and geophysical migration methods. *Journal of Nondestructive Evaluation*, 35(1):1–13, 2016. ISSN 15734862. DOI: 10.1007/s10921-016-0334-z.

M. Grohmann, S. Müller, E. Niederleithinger, and S. Sieber. Reverse time migration: introducing a new imaging technique for ultrasonic measurements in civil engineering. *Near Surface Geophysics*, 15(3):242–258, 2017. DOI: 10.3997/1873-0604.2017006.

J. B. Harley and J. M. F. Moura. Sparse recovery of the multimodal and dispersive characteristics of Lamb waves. *The Journal of the Acoustical Society of America*, 133(5):2732–2745, 2013. ISSN 0001-4966. DOI: 10.1121/1.4799805.

J. S. Heisey, K. H. Stokoe, and A. H. Meyer. Moduli of pavement systems from spectral analysis of surface waves. Technical report, Transportation Research Record 852, Transportation Research Board, Washington, D.C., 1982.

S. D. Holland and D. E. Chimenti. Air-coupled acoustic imaging with zero-group-velocity Lamb modes. *Applied Physics Letters*, 83(13):2704–2706, 2003. ISSN 00036951. DOI: 10.1063/1.1613046.

B. Hosten and M. Castaings. FE modeling of Lamb mode diffraction by defects in anisotropic viscoelastic plates. *NDT & E International*, 39(3): 195–204, apr 2006. ISSN 09638695. DOI: 10.1016/j.ndteint.2005.07.006.

M. Hu, Y. Lin, and C. Cheng. Method for Determining Internal P-Wave Speed and Thickness of Concrete Plates. *ACI Materials Journal*, 103(5): 327–335, 2006. ISSN 0889-325X. DOI: 10.14359/18154.

E. Kausel. Number and location of zero-group-velocity modes. *The Journal of the Acoustical Society of America*, 131(5):3601–10, may 2012. ISSN 1520-8524. DOI: 10.1121/1.3695398.

W. Ke, M. Castaings, and C. Bacon. 3D finite element simulations of an air-coupled ultrasonic NDT system. *NDT & E International*, 42(6):524–533, sep 2009. ISSN 09638695. DOI: 10.1016/j.ndteint.2009.03.002.

D. Kim, W. Seo, and K. Lee. IE-SASW method for nondestructive evaluation of concrete structure. *NDT & E International*, 39(2):143–154, mar 2006. ISSN 09638695. DOI: 10.1016/j.ndteint.2005.06.009.

P.-L. Liu, L.-C. Lin, Y.-Y. Hsu, C.-Y. Yeh, and P.-L. Yeh. Recognition of rebars and cracks based on impact-echo phase analysis. *Construction and Building Materials*, 142:1–6, jul 2017. ISSN 09500618. DOI: 10.1016/j.conbuildmat.2017.02.102.

V. Malhotra and N. Carino. *Handbook on Nondestructive Testing of Concrete*. CRC Press, Boca Raton, Florida, 2nd edition, 2004. ISBN 0-8493-1485-2.

K. R. Maser. Non-Destructive Measurement of Pavement Layer Thickness. *Final Report Caltrans No. 65A0074*, 2003.

R. Medina and A. Bayón. Elastic constants of a plate from impact-echo resonance and Rayleigh wave velocity. *Journal of Sound and Vibration*, 329(11):2114–2126, may 2010. ISSN 0022460X. DOI: 10.1016/j.jsv.2009.12.026.

R. Medina and M. Garrido. Improving impact-echo method by using cross-spectral density. *Journal of Sound and Vibration*, 304(3-5):769–778, jul 2007. ISSN 0022460X. DOI: 10.1016/j.jsv.2007.03.019.

S. Mezil, F. Bruno, S. Raetz, J. Laurent, D. Royer, and C. Prada. Investigation of interfacial stiffnesses of a tri-layer using Zero-Group Velocity Lamb modes. *The Journal of the Acoustical Society of America*, 138(5): 3202–3209, 2015. ISSN 0001-4966. DOI: 10.1121/1.4934958.

S. Müller, E. Niederleithinger, and T. Bohlen. Reverse Time Migration: A Seismic Imaging Technique Applied to Synthetic Ultrasonic Data. *International Journal of Geophysics*, 2012:1–7, 2012. ISSN 1687-885X. DOI: 10.1155/2012/128465.

A. Neville and J. Brooks. *Concrete Technology*. Prentice-Hall, Harlow, England, 2 edition, 2010. ISBN 978-0-273-73219-8.

M. Ohtsu and T. Watanabe. Stack imaging of spectral amplitudes based on impact-echo for flaw detection. *NDT and E International*, 35(3):189–196, 2002. ISSN 09638695. DOI: 10.1016/S0963-8695(01)00045-7.

C. B. Park, R. D. Miller, and J. Xia. Multichannel analysis of surface waves. *Geophysics*, 64(3):800–808, may 1999. ISSN 0016-8033. DOI: 10.1190/1.1444590.

G. F. Pla-Rucki and M. O. Eberhard. Imaging of Reinforced Concrete: State-of-the-Art Review. *Journal of Infrastructure Systems*, 1(2):134–141, 1995. ISSN 1076-0342. DOI: 10.1061/(ASCE)1076-0342(1995)1:2(134).

J. Popovics, W. Song, J. D. Achenbach, J. H. Lee, and R. F. Andre. One-sided stress wave velocity measurement in concrete. *Journal of Engineering Mechanics*, 124(12):1346–1353, dec 1998. ISSN 0733-9399. DOI: 10.1061/(ASCE)0733-9399(1998)124:12(1346).

J. Popovics, G. Cetrangolo, and N. Jackson. Experimental Investigation of Impact-Echo Method for Concrete Slab Thickness Measurement. *Journal of the Korean Society for Nondestructive Testing*, Vol 26(No 6):427–439, 2006.

J. Popovics, N. Ryden, and A. Gibson. New Developments in Nde Methods for Pavements. *Review of Quantitative Nondestructive Evaluation*, 27: 1320–1327, 2008. DOI: 10.1063/1.2902587.

S. Popovics. Effects of uneven moisture distribution on the strength of and wave velocity in concrete. *Ultrasonics*, 43(6):429–434, may 2005. ISSN 0041624X. DOI: 10.1016/j.ultras.2004.09.007.

C. Prada, D. Clorennec, and D. Royer. Local vibration of an elastic plate and zero-group velocity Lamb modes. *The Journal of the Acoustical Society of America*, 124(1):203–212, jul 2008. ISSN 1520-8524. DOI: 10.1121/1.2918543.

M. V. Predoi, M. Castaings, B. Hosten, and C. Bacon. Wave propagation along transversely periodic structures. *The Journal of the Acoustical Society of America*, 121(April):1935–1944, 2007. ISSN 00014966. DOI: 10.1121/1.2534256.

L. Qixian and J. Bungey. Using compression wave ultrasonic transducers to measure the velocity of surface waves and hence determine dynamic modulus of elasticity for concrete. *Construction and building materials*, 10(4):237–242, 1996. DOI: 10.1016/0950-0618(96)00003-7.

J. Roesset. Nondestructive dynamic testing of soils and pavements. *Tamkang Journal of Science and Engineering*, 1(2):61–80, 1998.

J. Roesset, D. Chang, K. Stokoe, and M. Aouad. Modulus and Thickness of the Pavement Surface Layer from SASW Tests. *Transportation Research Record*, (1260):53–63, 1990.

N. Ryden. Enhanced impact echo frequency peak by time domain summation of signals with different source receiver spacing. *Smart Structures and Systems*, 17(1):59–72, jan 2016. ISSN 1738-1584. DOI: 10.12989/sss.2016.17.1.059.

N. Ryden and M. Castaings. An Adaptive Frequency Domain Finite Element Model for Surface Wave Testing of Pavements. *AIP Conference Proceedings*, 1481(2009):1481–1488, 2009. DOI: 10.1063/1.3114132.

N. Ryden and C. B. Park. A combined multichannel impact echo and surface wave analysis scheme for non-destructive thickness and stiffness evaluation of concrete slabs. *AS NT, 2006 NDE Conference on Civil Engineering*, pages 247–253, 2006.

M. Sansalone. Impact-echo: the complete story. *ACI Structural Journal*, 94 (6):777–786, 1997. ISSN 08893241. DOI: 10.14359/9737.

M. Sansalone and W. Streett. *Impact-echo: Non-destructive Evaluation of Concrete and Masonry*. Bullbrier Press, 1997.

M. Schickert and M. Krause. Ultrasonic techniques for evaluation of reinforced concrete structures. In *Non-Destructive Evaluation of Reinforced Concrete Structures*, pages 490–530. Elsevier, 2010. DOI: 10.1533/9781845699604.2.490.

M. Schickert, M. Krause, and W. Müller. Ultrasonic Imaging of Concrete Elements Using Reconstruction by Synthetic Aperture Focusing Technique. *Journal of Materials in Civil Engineering*, 15(3):235–246, 2003. ISSN 0899-1561. DOI: 10.1061/(ASCE)0899-1561(2003)15:3(235).

F. Schubert and B. Köhler. Ten Lectures on Impact-Echo. *Journal of Nondestructive Evaluation*, 27(1-3):5–21, jul 2008. ISSN 0195-9298. DOI: 10.1007/s10921-008-0036-2.

F. Schubert, H. Wiggenhauser, and R. Lausch. On the accuracy of thickness measurements in impact-echo testing of finite concrete specimens–numerical and experimental results. *Ultrasonics*, 42(1-9):897–901, apr 2004. ISSN 0041-624X. DOI: 10.1016/j.ultras.2004.01.076.

V. Shevaldykin, A. Samokrutov, and V. Kozlov. Ultrasonic low-frequency transducers with dry dot contact and their applications for evaluation of concrete structures. In *2002 IEEE Ultrasonics Symposium, 2002. Proceedings.*, volume 00, pages 793–798. IEEE, 2002. ISBN 0-7803-7582-3. DOI: 10.1109/ULTSYM.2002.1193518.

S. W. Shin, C. B. Yun, J. S. Popovics, and J. H. Kim. Improved Rayleigh Wave Velocity Measurement for Nondestructive Early-Age Concrete Monitoring. *Research in Nondestructive Evaluation*, 18(1):45–68, jan 2007. ISSN 0934-9847. DOI: 10.1080/09349840601128762.

P. Shokouhi. Two-channel Impact-Echo. In *Non-Destructive Testing in Civil Engineering (NDT-CE 2009)*, Nantes, France, 2009. URL `http://ndt.net/article/ndtce2009/papers/102.pdf`.

P. J. Shull. *Nondestructive Evaluation - Theory, Techniques, and Applications*. M. Dekker, New York, 2002. ISBN 0-8247-8872-9.

O. Tofeldt and N. Ryden. Zero-group velocity modes in plates with continuous material variation through the thickness. *The Journal of the Acoustical Society of America*, 141(5):3302–3311, 2017. ISSN 0001-4966. DOI: 10.1121/1.4983296.

F. Treyssède and L. Laguerre. Numerical and analytical calculation of modal excitability for elastic wave generation in lossy waveguides. *The Journal of the Acoustical Society of America*, 133(June):3827–37, jun 2013. ISSN 1520-8524. DOI: 10.1121/1.4802651.

P. Turgut and O. F. Kucuk. Comparative relationships of direct, indirect, and semi-direct ultrasonic pulse velocity measurements in concrete. *Russian Journal of Nondestructive Testing*, 42(11):745–751, 2006. ISSN 1061-8309. DOI: 10.1134/S1061830906110064.

I. A. Viktorov. *Rayleigh and Lamb Waves Physical Theory and Applications*. Plenum Press, New York, 1967.

H. Wiggenhauser, A. Samokrutov, K. Mayer, M. Krause, S. Alekhin, and V. Elkin. Large Aperture Ultrasonic System for Testing Thick Concrete Structures. *Journal of Infrastructure Systems*, 23(1):B4016004, 2016. ISSN 1076-0342. DOI: 10.1061/(ASCE)IS.1943-555X.0000314.

T. Wu, J. Fang, G. Liu, and M. Kuo. Determination of elastic constants of a concrete specimen using transient elastic waves. *The Journal of the Acoustical Society of America*, 98(4):2142–2148, 1995.

J. Zhu and J. S. Popovics. Imaging Concrete Structures Using Air-Coupled Impact-Echo. *Journal of Engineering Mechanics*, 133(6):628–640, jun 2007. ISSN 0733-9399. DOI: 10.1061/(ASCE)0733-9399(2007)133:6(628).

D. Zywicki and G. Rix. Mitigation of near-field effects for seismic surface wave velocity estimation with cylindrical beamformers. *Journal of Geotechnical and Geoenvironmental ...*, (August):970–977, 2005. DOI: 10.1061/(ASCE)1090-0241(2005)131:8(970).

Appendices

Brief overview

A systematic error in terms of underestimated plate thickness from impact-echo and combined impact-echo and surface wave measurements is studied in Paper I. A new approach for estimation of Poisson's ratio and a new approach for Lamb wave phase velocity imaging with 2D arrays are proposed in Paper II and Paper III, respectively. A theoretical study about ZGV modes and inhomogeneous plates is studied in Paper IV.

Appendix A

Paper I

O. Baggens and N. Ryden. 2015.
Systematic errors in Impact-Echo thickness estimation due to near field effects. NDT & E International, 69:16-27.
DOI: 10.1016/j.ndteint.2014.09.003.

NDT&E International 69 (2015) 16–27

Contents lists available at ScienceDirect

NDT&E International

journal homepage: www.elsevier.com/locate/ndteint

Systematic errors in Impact-Echo thickness estimation due to near field effects

Oskar Baggens *, Nils Ryden

Division of Engineering Geology, Lund University, PO Box 118, SE-22100, Lund, Sweden

ARTICLE INFO

Article history:
Received 10 April 2014
Received in revised form
10 September 2014
Accepted 14 September 2014
Available online 22 September 2014

Keywords:
Concrete
Impact-Echo
P-wave velocity
Thickness
Near field effect

ABSTRACT

Near field effects are found to create systematic errors, within the range of about 5–15%, in thickness estimations from Impact-Echo (IE) testing. This paper studies near field effects from a point source in a combined Multichannel Analysis of Surface Waves (MASW) and Impact-Echo analysis. The near field creates deviations in the measured velocity of the P-wave and the Rayleigh-wave, which lead to an underestimated thickness. This systematic error is identified in both a numerical and a real field case. The results are also compared with the conventional Impact-Echo method.

1. Introduction

In civil engineering, efficient non-destructive quality control plays an important role in the optimization of resources for manufacturing, maintenance, and safety. For concrete construction, the thickness of plate-like structures is a parameter of particular interest [1–3]. Several techniques have emerged for determining this thickness in a non-destructive manner [4]. The Impact-Echo (IE) method is one such technique which provides a straightforward estimation of the thickness of a structure with only one accessible side.

Early studies using the IE method report thickness estimation accuracies within 3% [5]. Although recent advances show promising results for implementing non-contact scanning measurements [6], studies with more significant deviations exist [1,7,2]. In these studies the thickness is underestimated in 18 of 19 locations with a mean error of 8%. In many IE thickness testing applications, e.g. nuclear reactor containment walls or load carrying structures in bridges, a verification with a drilled core sample is often not possible. Further studies, as this paper, which can clarify and highlight difficulties and potential error sources, about IE thickness testing are therefore valuable.

The conventional IE method uses two estimated parameters: the thickness resonance frequency f_r and the P-wave velocity V_P [8]. The thickness resonance is measured from the dynamic response to a transient impact. The P-wave velocity is either measured or assumed. The thickness h is subsequently determined using the empirical relation:

$$f_r = \frac{\beta V_P}{2h} \tag{1}$$

where β is an empirical correction factor that is usually assigned the value 0.96 for concrete. In fact, the exact value of f_r corresponds to the minimum frequency of the first symmetric Lamb mode (S1) dispersion curve [9]. The group velocity is zero at this specific point (S1-ZGV) [10]. The next thickness resonance is related to the second anti-symmetric Lamb mode (A2), which is also a zero-group velocity point (A2-ZGV).

To properly evaluate plate properties such as the thickness parameter, Lamb wave theory must be used. Lamb wave theory states that a laterally infinite isotropic plate is defined by three independent parameters: the shear wave speed V_S, Poisson's ratio ν, and thickness h. Consequently, the accuracy of this type of non-destructive evaluation of plates is solely dependent on these three variables. As a result, traditional IE methods are usually complemented with some sort of surface velocity measurement to most accurately determine the thickness [11]. However, if exact values of f_r and V_P are known, an exact value of the thickness can be obtained using Eq. (1) only if a correct value of β is assumed. An alternative method of increasing accuracy is to calibrate a velocity that satisfies Eq. (1) using an exact thickness measurement from a core sample. This approach is, however, not applicable in the case of plates with one-sided access if non-destructive testing is desired.

V_P is usually estimated from the time taken by the first arriving wave to travel between two points separated by a known distance. One major source of uncertainty of the first arrival velocity is the

* Corresponding author.
E-mail address: oskar.baggens@tg.lth.se (O. Baggens).

http://dx.doi.org/10.1016/j.ndteint.2014.09.003

identification of the correct first arrival time. This uncertainty is due to the small displacement magnitude of the surface normal component of the first arriving wave. A common procedure is to identify the first value above a certain threshold, and to assume that this wave corresponds to a pure P-wave. Another approach, which may improve the identification, is to study the trend of the measured signal [12]. The velocity of the P-wave may also vary through the thickness due to a material gradient resulting from the casting of a concrete slab, if larger aggregates concentrate near the bottom of the slab [1]. Gibson showed a systematic difference between the P-wave velocity measured along the surface and through the thickness [4]. A gradient with an increasing P-wave velocity with depth has been observed by [1,13–15]. Popovics et al. proposed an additional correction factor to compensate for the slower P-wave velocity along the surface [1].

An alternative approach that eliminates difficulties in identifying the first arrival is to calculate V_P from the Rayleigh wave velocity V_R, estimated by means of spectral analysis of surface waves (SASW) [16]. This approach requires an assumed value of ν. Poisson's ratio can, for example, be determined from the ratio between the frequencies of S1-ZGV and A2-ZGV [10] or the ratio between the S1-ZGV frequency and V_R [17]. The latter approach requires a known value of the thickness.

More recent approaches use a combination of a multichannel recording and a multichannel IE analysis [18,19,7]. The specific evaluation procedures differ slightly in their approaches. However, the main concept is to introduce additional information from surface wave analysis, for example, by estimating V_R. Since at least three parameters are accessible, it is possible to incorporate Lamb wave theory. Then, all three plate parameters (V_S, ν, h) can be determined simultaneously. Compared with the traditional IE method, these types of analyses are not affected by the uncertainty of assuming a correct value of β.

A possible source contributing to the uncertainty in f_r is the presence of multiple peaks in the frequency response spectrum [20]. The use of a time frequency analysis has been suggested to enhance the identification of the correct S1-ZGV frequency [21,22]. The use of multichannel recordings is another approach to facilitate the identification of the correct S1-ZGV frequency. Summation of the traces in close vicinity to the point source can be used to make the S1-ZGV frequency more pronounced [18]. A similar approach uses a quantity described as a multicross spectral density [23].

Although several improvements to the IE method have been proposed, a remaining systematic error may result in an underestimated thickness [1,7,2]. This underestimation can occur if the P-wave velocity is underestimated or if the S1-ZGV frequency is overestimated (Eq. (1)). Of these two parameters, a velocity representative of the complete through thickness seems to be the most difficult parameter to measure. Most proposed methods are based on a P-wave and/or Rayleigh wave velocity measurement along the surface. A possible source of underestimated velocities along the surface may be due to near field effects, which in this case are due to the cylindrical spreading of waves from a point source and the interference of different wave modes [24–28]. To the authors' knowledge, the near field effect has not been previously studied in this context of combined IE and velocity measurements.

This study adopts a combined Multichannel Analysis of Surface Waves (MASW) and IE method. In conformance with the IE method, this type of analysis also assumes that the P-wave velocity can be obtained by studying the first arrival wave. The combined MASW/IE method measures the P-wave velocity (V_P), the Rayleigh wave velocity (V_R), and the S1-ZGV frequency (f_{S1-ZGV}). These three parameters are used to estimate the plate parameters V_S, ν, and h. The systematic variations of the measured parameters V_P, V_R, and f_{S1-ZGV} due to near field effects are studied for a plate without a velocity gradient with depth. These types of variations, within a few thickness distances from the source, are not specific for the studied MASW/IE method; in fact, they are present in all evaluations related to surface wave analysis and/or IE analysis. The results are therefore general for many cases. Finally, the influence of the evaluated thickness is further explored with both a synthetic and an experimental field case. The results from the MASW/IE method are also compared with the results obtained using the conventional IE method.

2. Lamb waves

Only two different wave types can exist in an isotropic infinite body, the P-wave and the S-wave [29]. In a laterally infinite plate, an additional boundary condition requires the stress traction to be equal to zero at the surfaces. Thus, it is possible for guided waves or Lamb waves to exist. Lamb waves are created from combinations of P- and S-waves that satisfy the traction-free boundary condition. An infinite number of combinations which satisfy this boundary condition exist. They are, however, governed by the same equation, the so-called Lamb wave equation:

$$\frac{\tan(\beta h/2)}{\tan(\alpha h/2)} = -\left[\frac{4\alpha\beta k^2}{(k^2-\beta^2)^2}\right]^{\pm 1} \tag{2}$$

where

$$\alpha^2 = \frac{\omega^2}{V_P^2} - k^2$$

$$\beta^2 = \frac{\omega^2}{V_S^2} - k^2$$

The Lamb wave equation is based on an assumption of plane wave propagation, and enforces that only certain combinations of wave numbers k and frequencies ω are possible. This is the origin of the dispersive nature of Lamb waves. No simple analytical solutions of the equation exist, and instead, numerical methods must be used [29]. The Lamb wave theory forms the basis for linear elastic wave propagation in plates.

The dispersive nature of Lamb waves can be illustrated in many ways. One possibility is to present dispersion curves in the frequency–phase velocity domain. Fig. 1a shows a selection of the dispersion curves (Lamb modes A0, S0, A1, and S1) for a plate with $\nu = 0.2$. The axes are normalized with the thickness h and the shear wave speed V_S. The curves are thus only dependent on ν. The curves in Fig. 1a are valid for all plates with $\nu = 0.2$.

The dispersion curves contain important information about the plate characteristics. The Rayleigh wave velocity can, for example, be determined by tracking the convergence of the phase velocity for the A0 and the S0 modes. The S1-ZGV point, which is the point of the minimum frequency of the S1-mode, is another quantity which can be determined. As mentioned before in Section 1, this point corresponds to the thickness resonance f_r used in the traditional IE method (Eq. (1)).

An expanded view of the S1-ZGV points for different values of ν is shown in Fig. 1b. The variations of the locations for the S1-ZGV points are only affected by ν. This implies that the value of fh/V_S for the S1-ZGV point is constant for a fixed value of ν, and serves as the theoretical link between the empirical β factor used in the IE method and an analytical expression as a function of ν [9,17]. The constant value of fh/V_S provides a direct way of determining the plate thickness once V_S, ν, and f_{S1-ZGV} are known.

The constant value of fh/V_S also reveals how the estimated thickness is affected by uncertainties in the quantities V_S, ν, or f_{S1-ZGV} (Fig. 1b). An overestimation of f_{S1-ZGV} yields an

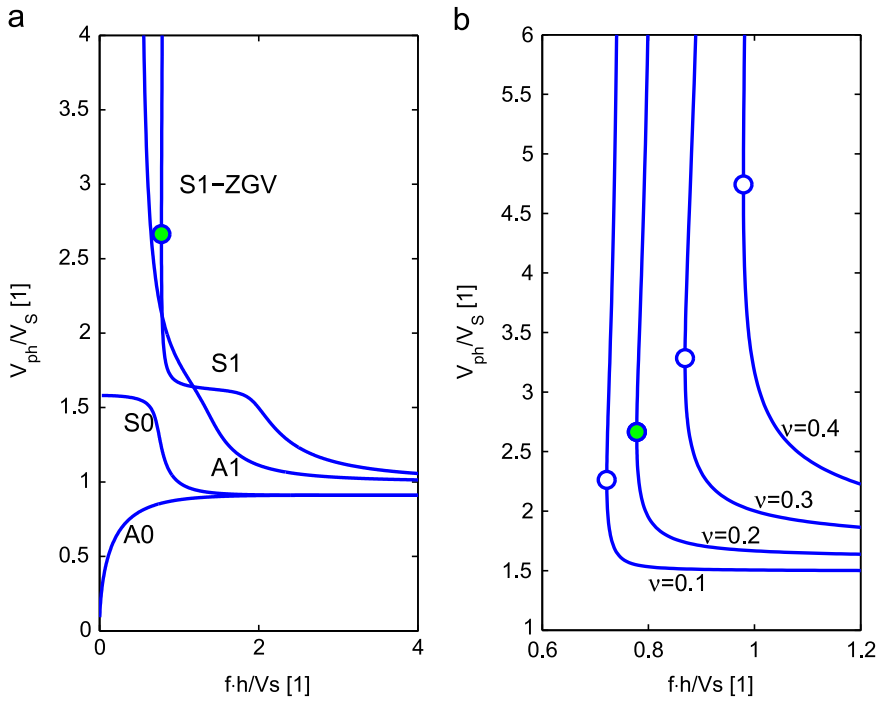

Fig. 1. (a) Lamb wave dispersion curves (A0, S0, A1, and S1 modes). (b) Expanded view around S1-ZGV points (S1 mode).

underestimated thickness, whereas an overestimation of V_S yields an overestimated thickness, assuming that the other two constants are exact. Finally, an overestimation of ν results in an overestimated thickness (Fig. 1b).

In practice, the plate parameters V_S, ν, and h are in most cases not directly accessible. Therefore, they must be determined indirectly using other parameters. One possibility is to measure V_P, V_R, and f_{S1-ZGV}, for example, by means of a combined MASW/IE method [18]. These three quantities provide the necessary information to determine V_S, ν, and h, and this approach was adopted in this study. The accuracy of the thickness estimation, which is of particular interest, is therefore dependent on the accuracy of the indirect parameters V_P, V_R, and f_{S1-ZGV}.

3. Numerical modeling

The presented theory in Section 2 assumes plane wave propagation, which at several wavelength's distance is a good approximation even for waves generated by a point source. As the radial distance of the studied waves decreases, this assumption becomes less valid, and near field effects are present. Furthermore, close to the source several different wave modes (e.g. P-waves, S-waves, Rayleigh waves) interfere with each other. A suitable approach for studying these two factors (i.e. near field effects) and the transition to the far field is to use a numerical model. A synthetic model, by means of Finite Elements (FE), was created in order to investigate the accuracy of the V_P, V_R, and f_{S1-ZGV} estimates determined by a combined MASW/IE technique. The model was created using commercial finite element software, Comsol Multiphysics [30]. A 2D axial symmetric plate was defined using a linear elastic material with Young's modulus of 36.1 MPa and a density of 2197 kg/m^3. The model was calculated using Poisson's ratios of 0.1, 0.2, 0.3, and 0.4, thus, covering a wide range of possible materials.

The thickness was set to 0.261 m and the length of the plate was 25 times longer than the thickness (Fig. 2). A short line load at the top surface was applied to simulate a point source. The load started at the symmetry axis and had a radius of 0.0025 m.

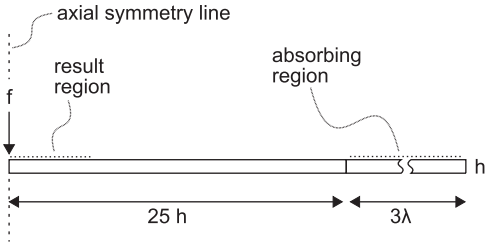

Fig. 2. FE-model sketch.

The plate was studied in the frequency domain, solving for the complex steady state response. A triangular element mesh with quadratic shape functions was used. A fine mesh with a minimum element length of 0.0025 m was used around the source location. In the rest of the model the element mesh was adjusted to have at least 10 elements per wavelength of the A0 mode. The mesh was thus adjusted for the solved frequencies using a coarse mesh for the low frequencies and a finer mesh for the high frequencies [31].

A silent boundary was created by a gradually increasing damping ratio in the absorbing region [32]. This region was added as an extension to the plate (Fig. 2). The length of the absorbing region was adjusted for the solved frequency with a length of 3 times the wavelength of the P-wave. The defined mesh and absorbing parameters were determined by a parametric convergence study of the theoretical Rayleigh wave velocity and S1-ZGV frequency.

In order to simulate the Impact-Echo and surface wave test, three synthetic force pulses were defined. The pulses were based on the Gaussian mono-pulse with different frequency contents (Fig. 3). The Gaussian mono-pulse was chosen to avoid energy at 0 Hz, as this energy can be difficult to handle in frequency domain simulations of a free plate. The pulses can be characterized as a low-frequency, mid-frequency, and high-frequency pulse with regard to the S1-ZGV frequencies (7–9 kHz) of the simulated plates.

The frequency domain responses along the upper surfaces of the plates from the pulses were calculated using the result from

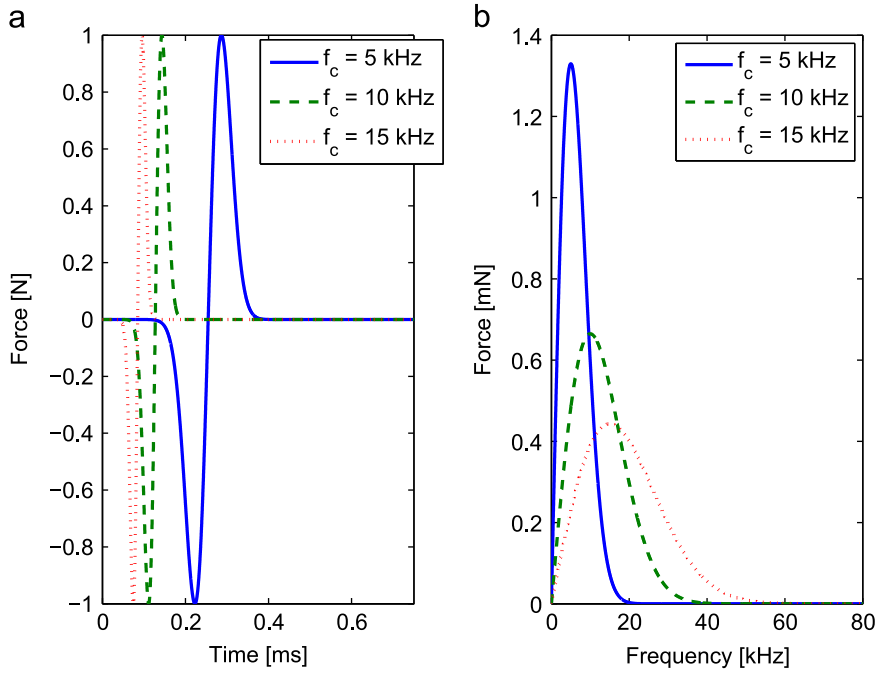

Fig. 3. Force pulses: (a) time domain, (b) frequency domain.

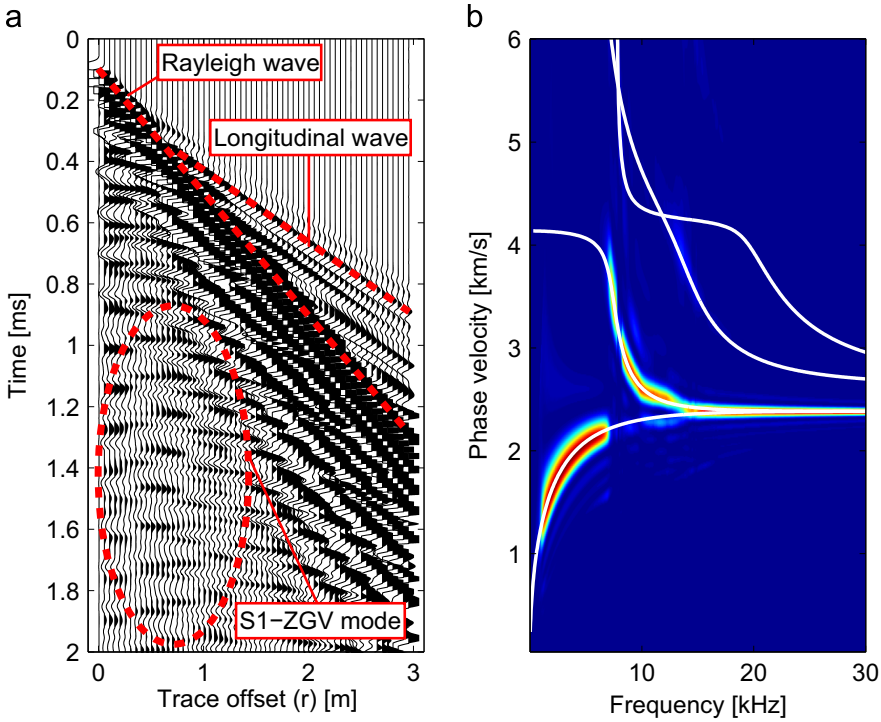

Fig. 4. Dataset: (a) time domain, (b) phase velocity–frequency domain.

the steady state analysis (Fig. 2). Subsequently, an inverse Fourier transform was performed to generate the response for the pulses in the time domain [32]. This concept was used to create synthetic multichannel datasets (Fig. 4a). The datasets were transformed into the phase velocity–frequency domain (Fig. 4b) [33]. It could be seen that the theoretical Lamb wave curves correlated well with the synthetic datasets. A detailed analysis of the difference between the simulated and theoretical values will be studied in the subsequent Results section.

4. Results

Estimates of the first arrival P-wave velocity (V_P), the Rayleigh wave velocity (V_R), and the S1-ZGV frequency (f_{S1-ZGV}) have been studied as a function of distance from the source in order to quantify the influence of the near field. In all the presented result plots the distance from the source has been expressed as radius divided by thickness (r/h). This scale is used to emphasize that results are roughly applicable to any plate thickness although an

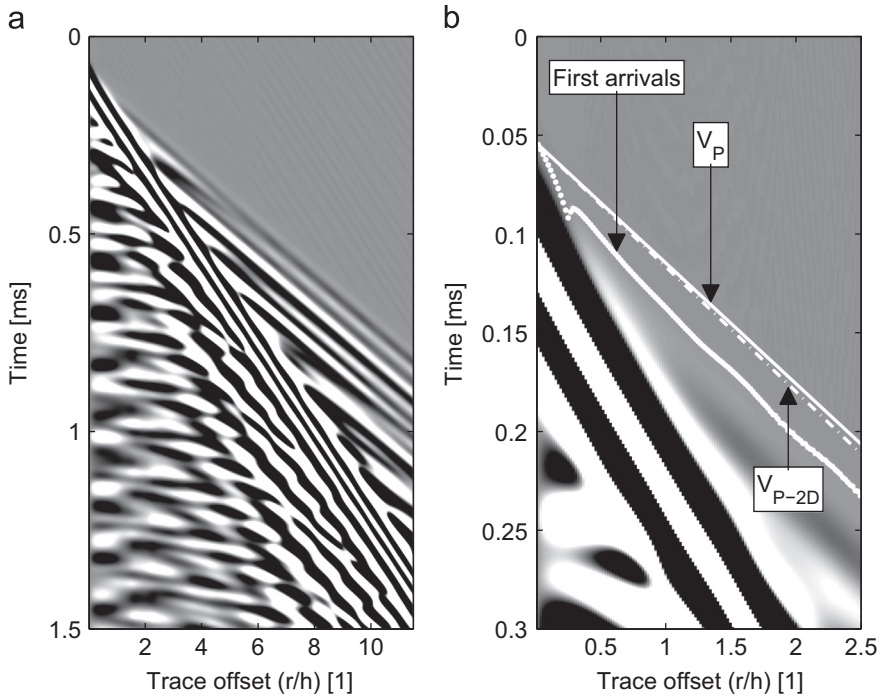

Fig. 5. Dataset $\nu=0.2$, $f_c=10$ kHz: (a) time domain, (b) expanded view, first arrivals.

exact normalization in both time (frequency) and space (wavelength) is not possible.

4.1. P-wave velocity

The variation of the first arrival P-wave velocity as a function of distance was studied for plate models with different values of ν. The models were studied in the time domain using the mid-frequency pulse (see Fig. 3). Fig. 5a shows the surface normal acceleration response to the mid-frequency pulse for the plate with $\nu=0.2$. The surface normal acceleration response was subsequently used to determine the first arrival P-wave.

Signals were gained in order to enhance the picture of the wave field and the first arrivals (Fig. 5b). In this type of commonly used seismic plot, the first arrival velocity close to the impact source appears to be close to the Rayleigh wave velocity. At a distance of about 1/4 of the thickness, there is a jump to a faster first arrival velocity which is closer to the P-wave velocity. The hidden first arrival of the P-wave is a consequence of the huge difference in amplitude of the Rayleigh wave and the P-wave (interference of modes).

First arrivals were picked for each trace at time points corresponding to the first absolute values above a threshold limit (Fig. 5b). The threshold limit was set at 10^{-4} of the maximum absolute value of the amplitude in each individual trace. Consequently, the threshold limit was reduced with an increasing radial distance. Fig. 5b also shows the theoretical first arrival P-wave velocity (V_P) along with the slightly slower quasi-P-wave velocity in plates (V_{P-2D}), marked with dotted lines. V_{P-2D} corresponds to the low frequency asymptotic value of the S0 Lamb mode in plates (Fig. 1a) and is the expected low frequency P-wave velocity in a plate [29]. The theoretical first arrivals were adjusted to intersect with the first arrival of the first trace.

The P-wave velocity was calculated by adjusting a slope to the first arrivals using linear regression. This evaluation was repeated while adding new traces to the array, and thus the length of the array was gradually extended. In all evaluations, the first trace was located at a fixed offset of 0.005 m from the impact center. This type of evaluation corresponds to a typical combined MASW/IE analysis.

In order to simulate the procedure used in the IE standard, the first arrival P-wave velocity was also calculated using two traces only. The first trace was selected at an offset of 0.005 from the impact center, and the second trace was selected at a distance of 0.3 from the first trace. The time difference of the first arrivals and the known distance of 0.3 m between the traces were used to yield the first arrival P-wave velocity. This calculation was repeated for different offset locations of the two traces, while maintaining a fixed internal distance between the traces of 0.3 m. This type of evaluation corresponds to the conventional Impact-Echo procedure when the first transducer is located at an offset of 0.15 m from the impact center [11].

The results from the MASW/IE and the IE type of analysis of the first arrivals are shown in Fig. 6a and b, respectively. The extracted velocities have been normalized with the theoretical P-wave velocity for each Poisson's ratio. In both types of analysis the initial normalized first arrival velocity close to the impact source is lower than the theoretical values. At a greater distance from the source, the normalized first arrival velocity gradually approaches the theoretical value. It can also be noticed that the sign of acceleration response (i.e., the direction) of the first arrivals is not constant and causes a discontinuity in the curve located at an offset of about 1/4 thickness. This shift of sign explains the momentarily high velocities of the IE type of analysis (Fig. 6b).

For Poisson's ratios 0.1 and 0.4, there are also other phase shifts at greater distances from the source. These phase shifts are caused by Lamb wave dispersion and generate extreme velocities in the IE analysis. Therefore, the first arrival P-wave velocity was only tracked until such an event occurred (Fig. 6b). The MASW/IE type of analysis is not affected in the same way, and it presents a more stable trend since it is based on an evaluation using multiple traces. It is also observed that the results for both evaluation methods are dependent on ν.

The above studied methods for determining the first arrival P-wave velocity are time domain evaluations, as are normally performed in practice. This type of analysis does not account for the dispersion which is typical for Lamb waves (Fig. 4b). Therefore, the dependency of frequency needed to be explored further.

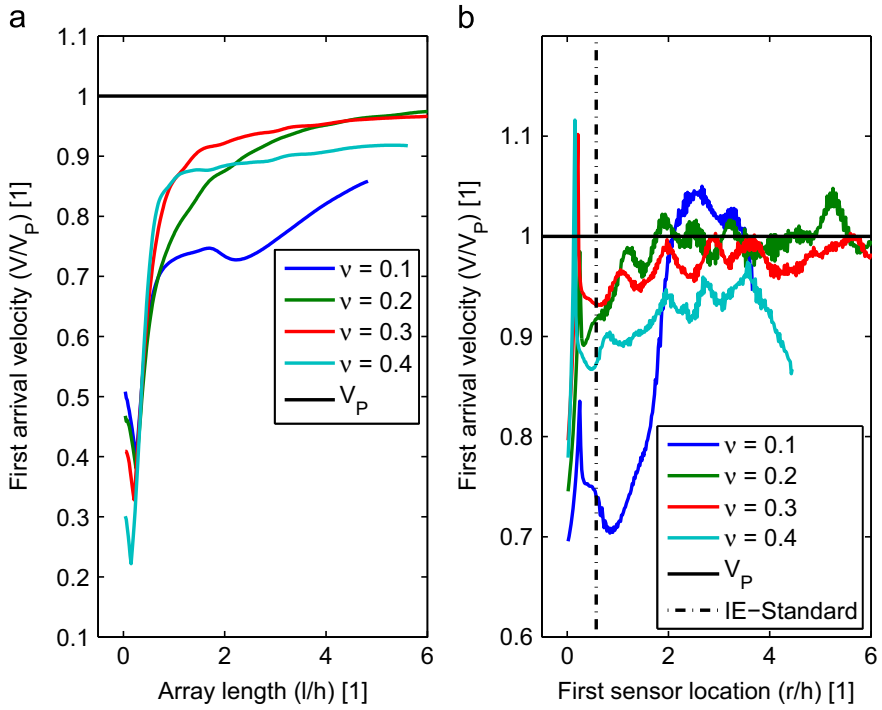

Fig. 6. First arrival velocity: (a) MASW/IE, (b) IE.

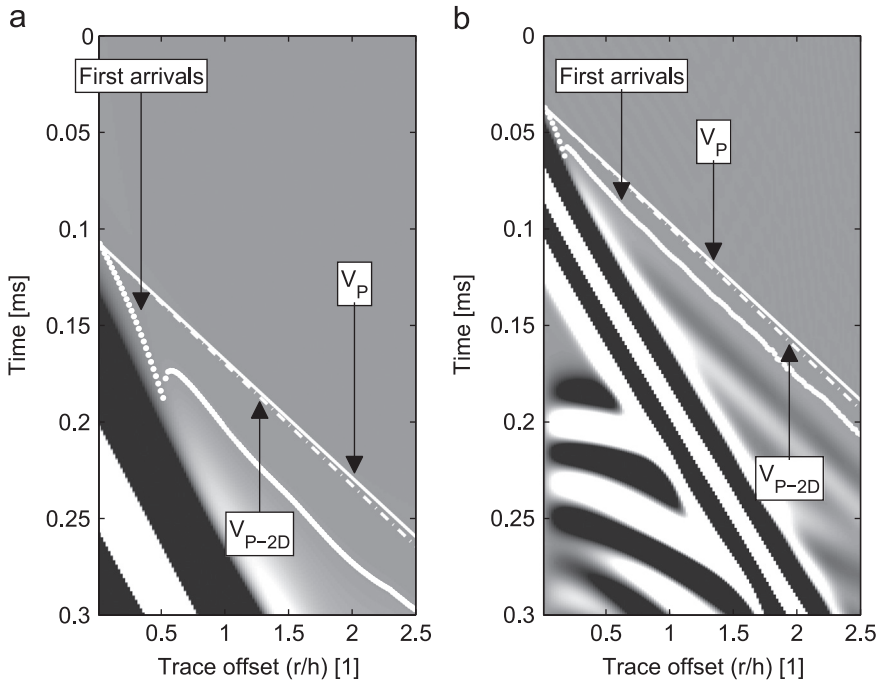

Fig. 7. Dataset, first arrivals: (a) $\nu=0.2$, $f_c=5$ kHz, (b) $\nu=0.2$, $f_c=15$ kHz.

The plate model with $\nu=0.2$ was chosen for a study using different pulses. The variation of the first arrival P-wave velocity as a function of distance was studied for the low, mid-, and high-frequency pulses. The surface normal acceleration responses of the low- and high-frequency pulses are shown in Fig. 7a and b, respectively.

It can be seen that the response of the low-frequency pulse (Fig. 7a) creates a larger zone with a slower first arrival velocity compared to that of the high-frequency pulse (Fig. 7b). This is consistent with the condition that a low-frequency pulse generates a response with a longer wavelength. The same type of evaluations for the first arrival P-wave velocity based on the MASW/IE and IE methods was performed for the different pulses. The results are shown in Fig. 8a and b. It can be noticed that variations in the estimated first arrival P-wave velocities are also dependent on the frequency content of the exciting pulses.

4.2. Rayleigh wave velocity, S1-ZGV frequency

The variation in V_R was studied for the plates with different values of ν. The mid-frequency pulse was used to create the

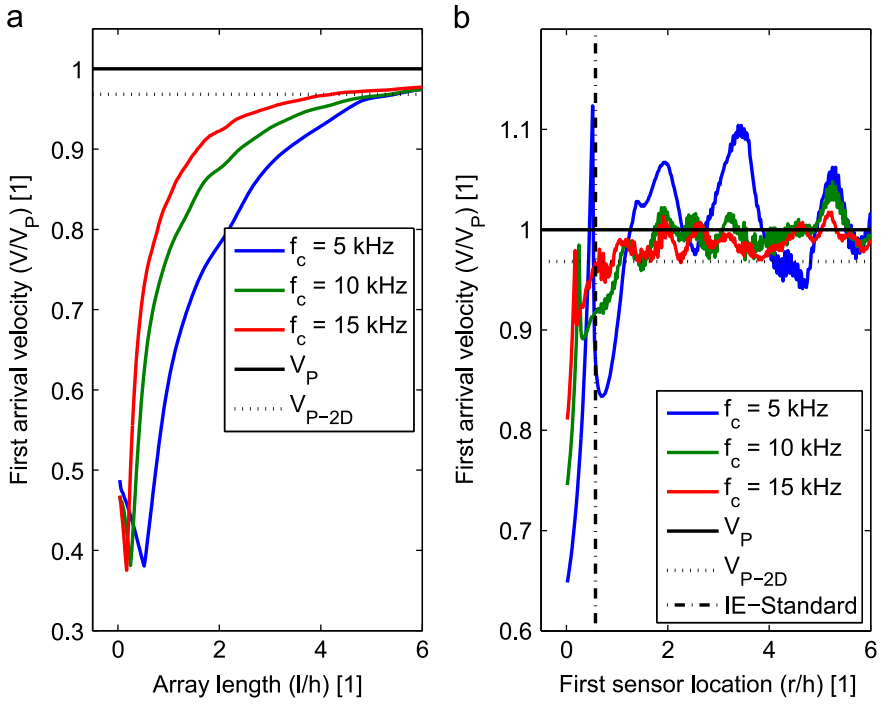

Fig. 8. First arrival velocity: (a) MASW/IE, (b) IE.

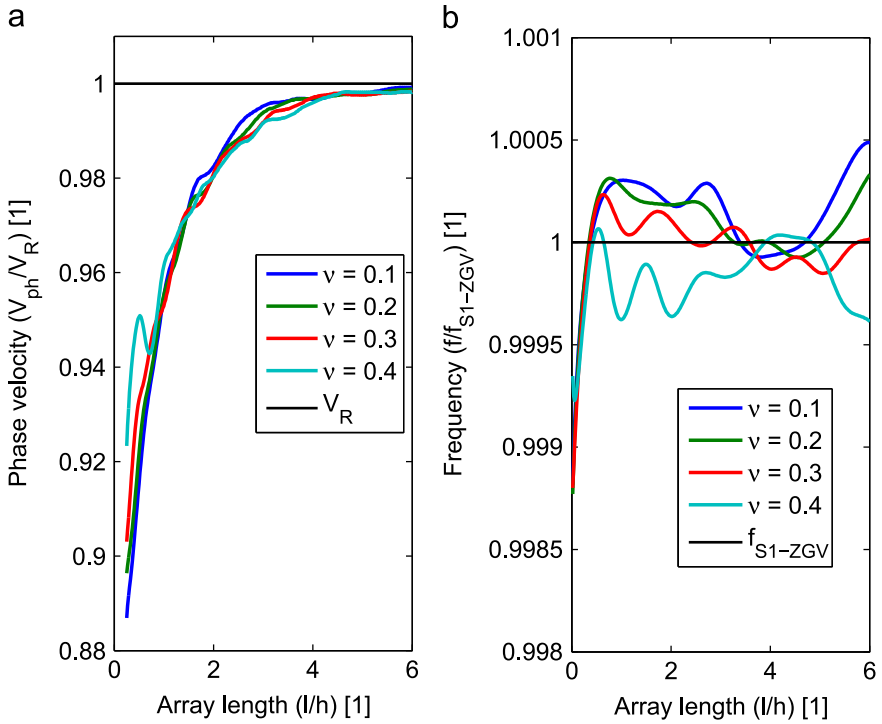

Fig. 9. (a) Rayleigh-wave velocity. (b) S1-ZGV frequency.

datasets. V_R was estimated by tracking the convergence of the A0 and S0 modes of the datasets in the frequency–phase velocity domain. This evaluation was made for different array lengths. The array was extended by adding new traces as with the study of the first arrival P-wave velocity. The extracted velocity is shown in Fig. 9a. It can be observed that V_R is underestimated close to the source, i.e. when the array in the combined MASW/IE method is short. Thereafter, the estimated velocity gradually increases and converges with the theoretical velocity when the array lengthens. The estimated velocity is dependent on ν. However, the main behavior is generally the same for all values of ν. The observed phenomena are in agreement with the results obtained by [26,28] for V_R in a half space. Roesset [26] showed analytically how the phase velocity for the response at the surface increases with the distance from the source in the case of a homogeneous half-space. This slower phase velocity close to the source is related to the variation in the interference between the bulk wave modes. For the studied case shown in Fig. 9a, the near-field effect is likely to

be even more complicated, since the geometry is a plate instead of a half-space. Furthermore, the use of an array as well as the frequency content of the impulse may also add additional complexity to the problem. Therefore, the result shown in Fig. 9a should not be interpreted exactly quantitatively but rather as a general trend partly explaining the observed underestimated thickness.

The S1-ZGV frequency was estimated using an offset summation technique [18]. This technique was used in the combined MASW/IE analysis to enhance the S1-ZGV resonance frequency peak [7]. The evaluation was made for different array lengths in the same manner as with the evaluation of V_R. The results from the S1-ZGV frequency estimations are shown in Fig. 9b. These estimations do not provide a completely constant value; instead, they oscillate slightly. These minor variations were assumed to be associated with uncertainties inherited from the nature of numerical modelling and evaluations. However, in comparison with the estimations of V_P and V_R, the estimations of f_{S1-ZGV} can be considered as accurate.

4.3. Thickness

The above demonstrated variations in the estimations of V_P and V_R indicate that a systematic error is present using the MASW/IE or the IE method. Thus, a systematic error is also present if the thickness is calculated from the estimations of V_P and V_R.

An estimate of the thickness as a function of distance was therefore calculated by combining the results in Figs. 6 and 9 from the mid-frequency source (f_c=10 kHz). These calculations were made using both the MASW/IE and IE techniques. In the MASW/IE analysis, ν was calculated from ratio of the first arrival P-wave velocity and the Rayleigh wave velocity. In this evaluation the first arrival P-wave velocity was assumed to correspond to the theoretical velocity of V_P. Thereafter, the thickness was calculated from the constant value of the quantity fh/V_S, as described in Section 2. The IE analysis used values of the first arrival P-wave velocity from Fig. 6b and a fixed value of the S1-ZGV frequency. This fixed value was extracted from the frequency spectrum of one single trace at a distance of 0.05 m from the source. The thickness was subsequently estimated using Eq. (1) with β=0.96 to mimic a real case evaluation where ν in general is not known beforehand. The estimated thicknesses by the MASW/IE and the IE method are shown in Fig. 10a and b, respectively.

For the MASW/IE analysis, ν was generally underestimated due to the underestimated ratio between the first arrival P-wave velocity and the Rayleigh wave velocity. Therefore, in the case of the model with a ν=0.1, it was not possible to estimate the thickness since the Lamb wave equation only was solved for values of ν from 0.10 to 0.45 (with increments of 0.01). This fixed increment of 0.01 explains the discontinuities in the curves in Fig. 10a. It can be observed that the MASW/IE type of method underestimates the thickness (Fig. 10a). As the estimates of V_P and V_R become more accurate, the estimated thickness subsequently becomes more accurate. Similar results were obtained from datasets with source frequencies f_c=5 kHz and f_c=15 kHz, although they are not plotted here. It should also be noticed that the alternative interpretation of the first arrival P-wave velocity as V_{P-2D} does not improve the results.

The estimated thickness from the IE method shows a more fluctuating result with a higher relative error compared to the MASW/IE analysis (Fig. 10b). The variation in the thickness (Fig. 10b) follows the variation of the estimated value of V_P (Fig. 6b), since the values for β and f_r were given a constant value when Eq. (1) was evaluated. It can be observed that the IE method for the case of this quite unrealistic value of ν=0.4 overestimates the thickness. This is due to the fixed value of β=0.96. A more suitable value would have been around 0.80 [9,17]. However, with real case data, the value of ν typically is not known beforehand. The analysis was therefore made with a fixed value of 0.96 for the β factor.

In the standard IE velocity measurement of the first arrival P-wave the estimated thickness is actually quite close to the true value (within 4%) after $r/h > 2$. With this set-up the problematic near field effect for a homogeneous plate is effectively minimized.

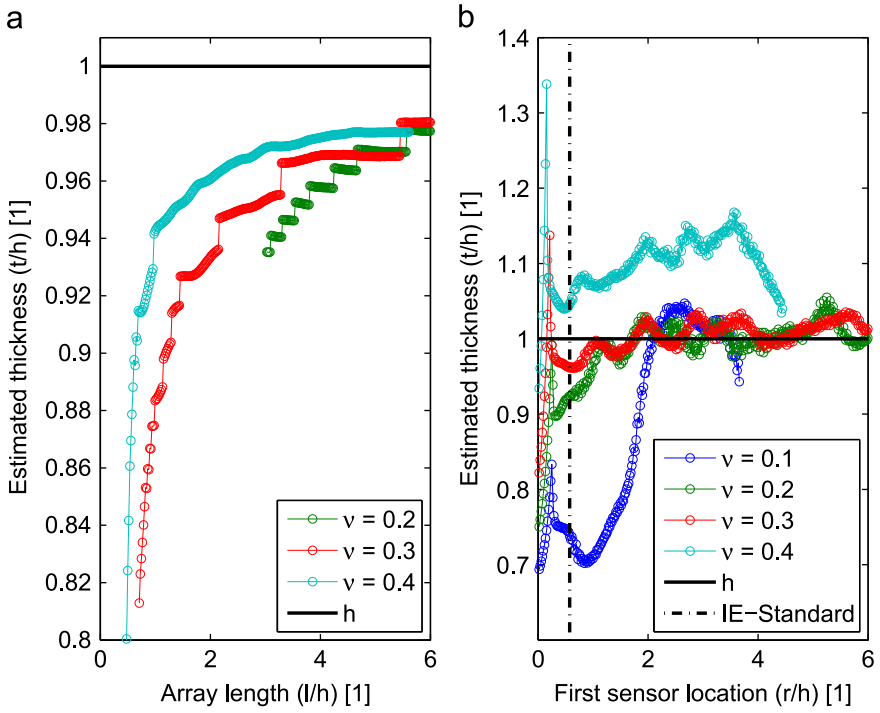

Fig. 10. Estimated thickness: (a) MASW/IE, (b) IE.

For the studied plate and source frequency this result is valid for all Poisson's ratios, except the quite unrealistic value of $\nu = 0.4$ for concrete.

5. Field case

The systematic error presented in Fig. 10 was further explored by studying a real field case. The aim of this field study was to investigate to which extent the near field effects could be observed in a real practical case. Field data was obtained from a Portland concrete cement plate cast on a granular base at The Advanced Transportation Research and Engineering Laboratory (ATREL), University of Illinois at Urbana-Champaign (UIUC). This plate is at the same location as location 5 in [7]. In this point the thickness was underestimated with all tested seismic techniques (4–13%).

Time-synchronized multichannel data were obtained using one accelerometer and a hammer with a trigger connected to a DAQ computer [34]. The accelerometer measured the surface normal component of the acceleration response. Data were collected over a distance of 1 m with an interval distance of 0.02 m between each hammer impact. The data could therefore be used for a MASW/IE and an IE analysis using the same evaluation techniques previously described. A core sample was also extracted from the center of the 1 m long MASW/IE array. The thickness was measured to 0.337 m [7].

A plot of the data in time domain and frequency–phase velocity domain can be seen in Fig. 11a and b, respectively. The locations of the first arrivals are marked with black dots in Fig. 11a. The first arrivals were identified at time points corresponding to the first absolute value exceeding a threshold limit. This threshold limit was set at 2.5×10^{-3} of the maximum absolute value in each individual trace. As in the synthetic case, the threshold limit was reduced with an increasing radial distance.

The indirect plate parameters V_P, V_R, and f_{S1-ZGV} were estimated in the same way as with the synthetic dataset. Estimations of the parameters were repeated using a different number of signals from the dataset, i.e., for different lengths of the measuring array. Thus, it was possible to create plots, similar to those previously presented, for the variation of the parameters with respect to the array length.

5.1. P-wave and Rayleigh wave velocity, S1-ZGV frequency

The variation of the first arrival P-wave velocity for the MASW/IE analysis can be seen in Fig. 12a. Fig. 12b shows the variation of the first arrival P-wave velocity using the IE type of measurement.

It can be observed that the first arrival P-wave velocity increases with the array length or the location of the sensors. This is the same general trend as with the synthetic case. The observed low resolution in Fig. 12b is a consequence of the low sample rate in the field data ($dt = 5$ μs) compared to the synthetic data case ($dt = 0.1$ μs). Ideally, a higher sample rate with lower value than $dt = 5$ μs should therefore be used.

It should be noted that a refracted P-wave can cause a similarly increasing velocity with distance due to an increasing stiffness within the concrete layer. In the analyzed test location, a velocity gradient (V_P=4450 m/s, 4765 m/s, 4828 m/s, from top to bottom) was actually observed by ultrasonic pulse velocity measurements of different sections of the extracted core sample. Assuming a top lower velocity layer with a thickness 0.05 m, a two-layer refraction model analysis can be made. From this, it is possible to estimate the radial distance for an appearance of a refracted P-wave [35]. It was found that a higher velocity from refraction could be predicted at a distance starting from about 1.5 thicknesses. Thus, it can be concluded that the material gradient cannot be the only explanation of the slower velocity close to the source in Fig. 12. Therefore, the consequence of the gradient in this case may act as an additional contribution to an increasing velocity with distance.

The estimations of the Rayleigh wave velocity and the S1-ZGV frequency are shown in Fig. 13a and b, respectively.

It can be seen in Fig. 13a that the Rayleigh wave velocity takes a lower value close to the source. Regarding the S1-ZGV frequency in Fig. 13b, a minor variation of the frequency is found. It was assumed that the S1-ZGV frequency also in this case could be

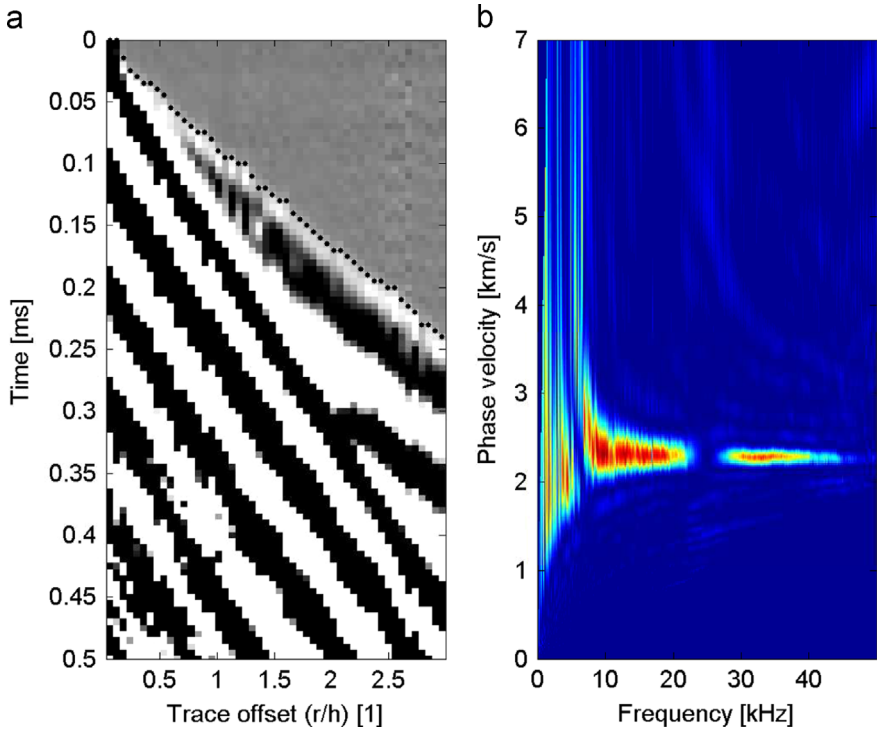

Fig. 11. Field data: (a) time domain, (b) phase velocity–frequency domain.

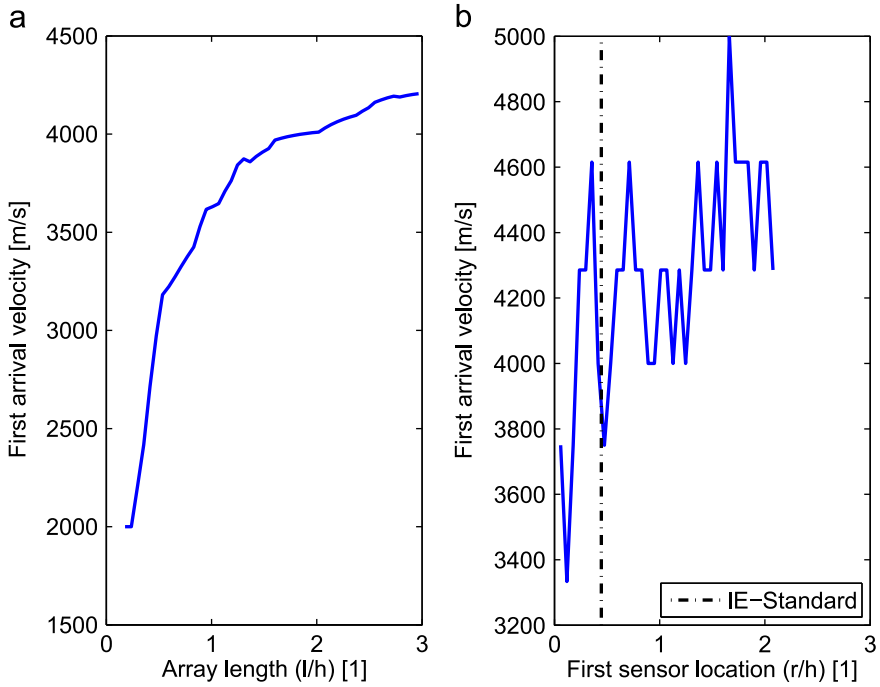

Fig. 12. First arrival velocity: (a) MASW/IE, (b) IE.

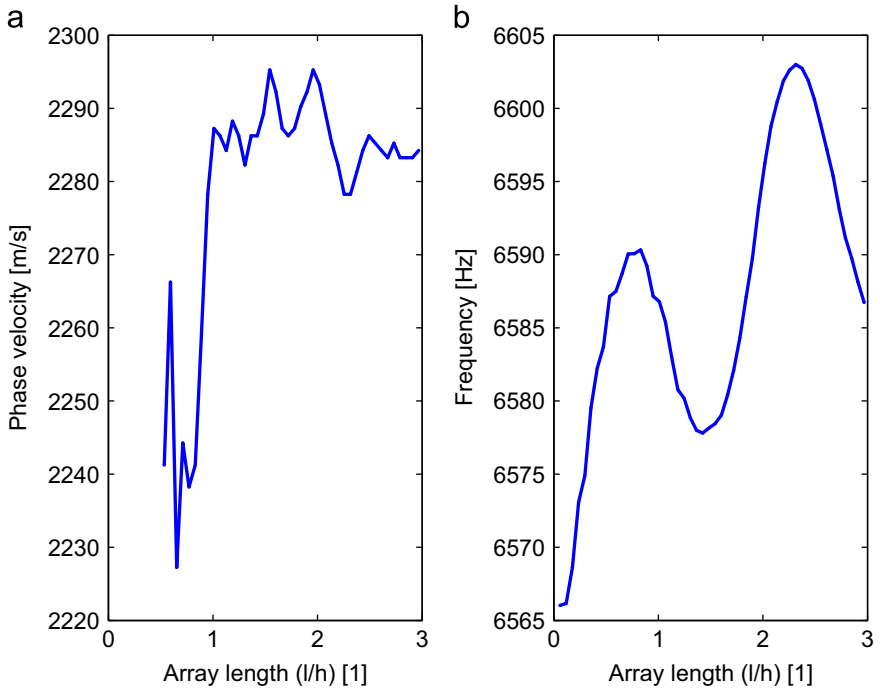

Fig. 13. (a) Rayleigh-wave velocity. (b) S1-ZGV frequency.

estimated with good accuracy. These observations for the Rayleigh wave velocity and S1-ZGV frequency are in agreement with the results obtained from the synthetic case.

Although the variations of the estimated parameters in Figs. 12 and 13 are not identical to the results from the synthetic dataset, it is possible to identify a common general behavior. It can also be observed that the estimated first arrival P-wave velocity shows the largest relative variation of the estimated quantities. The Rayleigh wave velocity shows the second largest relative variation, whereas the estimation of the S1-ZGV frequency only shows a minor relative variation. This result of the relative variation in the estimated parameters is in agreement with the result from the synthetic case.

5.2. Thickness

The estimations of V_P, V_R, and f_{S1-ZGV} were then subsequently used to calculate the variation in the corresponding estimated thickness. This calculation was made for the MASW/IE and IE types of methods, and followed the same procedure as for the synthetic case. The variation of the estimated thickness for the MASW/IE and IE types of methods can be seen in Fig. 14a and b, respectively.

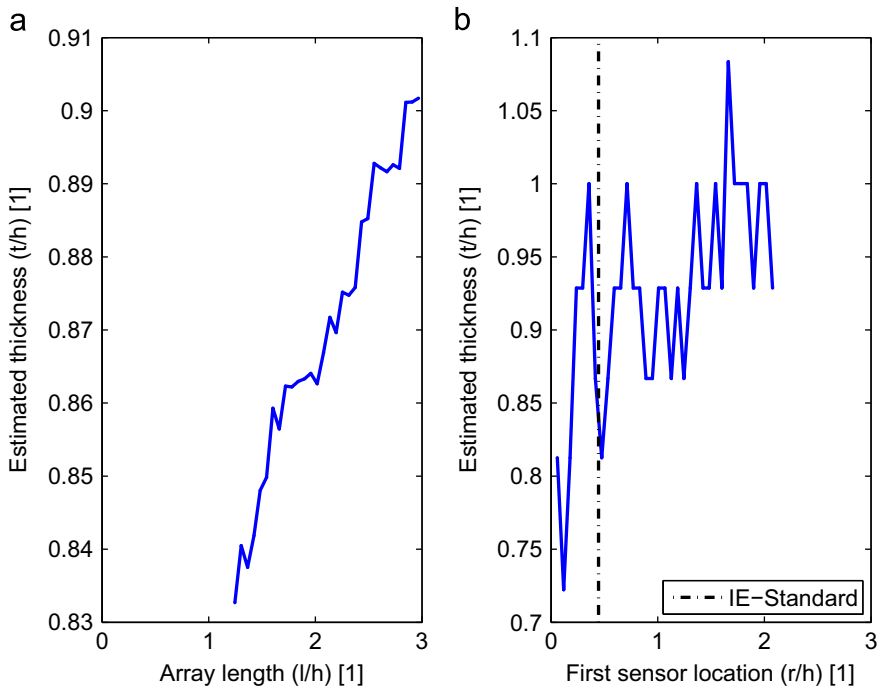

Fig. 14. Estimated thickness: (a) MASW/IE, (b) IE.

Fig. 14a shows that the MASW/IE analysis underestimates the thickness, especially when the array length is short. For the IE method in Fig. 14b, the thickness is underestimated in most cases. The IE method also shows a more fluctuating result due to the variation of V_P. It should be noted that part of this fluctuation originates from the relatively low sample rate. The general trend in Fig. 14 agrees qualitatively with the synthetic data presented in Fig. 10 within a distance of 3 thicknesses. It should be noted that longer array lengths are often unsuitable in practice and not desired since local plate properties are then smeared out. The observed larger underestimation in the field case, compared with the synthetic case, could be caused by the velocity gradient within the layer [1].

6. Conclusions

Numerical results show that near field effects can cause a systematic error in the estimation of thickness using a MASW/IE or a conventional IE method. The major source of error in the thickness estimations is related to the interpretation of the first arrival as a pure P-wave velocity. Detailed numerical analyses close to the point source reveal strong interference between the P-wave and the Rayleigh wave in the near field. This results in a zone where the first arrival velocity cannot be directly linked to the theoretical P-wave velocity. Furthermore, the size of this zone close to the point source is dependent on the plate properties and the source frequency content. This near field effect leads to an underestimated P-wave velocity from the picked first arrivals. These results further verify the inherently difficult and questionable task of estimating the P-wave velocity from first arrivals of dispersive Lamb waves.

The Rayleigh wave is also affected by the near field effect. Close to the point source, a lower value than the theoretical Rayleigh wave velocity is observed.

The S1-ZGV frequency is in general estimated with good accuracy.

The combined errors due to the near field effects create a systematic error which underestimates the thickness. This predicted systematic error of the estimated thickness from the MASW/IE and IE methods is found to be about 5–15% depending on Poisson's ratio, measurement set-up and source pulse. These findings are important for future improvements of non-destructive methods, such as the MASW/IE and IE methods.

Acknowledgments

Professor John S. Popovics is acknowledged for providing the experimental test site at The Advanced Transportation Research and Engineering Laboratory (ATREL), University of Illinois at Urbana-Champaign (UIUC) and for providing additional reference data of core samples. Professor Michael Lowe is acknowledged for valuable comments and discussions during the course of this study. The Development Fund of the Swedish Construction Industry (SBUF, No. 12534) and The Swedish Radiation Safety Authority (SSM, No. SSM2012-890) are acknowledged for financing the study.

References

[1] Popovics J, Cetrangolo G, Jackson N. Experimental investigation of impact-echo method for concrete slab thickness measurement. J Korean Soc Nondestruct Test 2006;26(6):427–39 URL ⟨http://www.dbpia.co.kr/Journal/ArticleDetail/3207698⟩.
[2] Maser KR. Non-destructive measurement of pavement layer thickness. Technical report. California Department of Transportation; 2003.
[3] Deacon JA, Monismith CL, Harvey JT. Pay factors for asphalt-concrete construction: effect of construction quality on agency costs. Technical report. Pavement Research Center, Institute of Transportation Studies, University of California, Berkeley; 1997.
[4] Gibson A. Advances in nondestructive testing of concrete pavements [Ph.d. thesis]. University of Illinois; 2004.
[5] Sansalone M, Streett W. Impact-echo: non-destructive evaluation of concrete and masonry. Jersey Shore: Bullbrier Press; 1997.
[6] Zhu J, Popovics JS. Imaging concrete structures using air-coupled impact-echo. J Eng Mech 2007;133(6):628–40. http://dx.doi.org/10.1061/(ASCE)0733-9399(2007)133:6(628) URL ⟨http://www.scopus.com/inward/record.url?eid=2-s2.0-34249020731&partnerID=tZOtx3y1⟩.
[7] Popovics J, Ryden N, Gibson A. New developments in NDE methods for pavements. Rev Quant Nondestruct Eval 2008;27:1320–7 URL ⟨http://scitation.aip.org/content/aip/proceeding/aipcp/10.1063/1.2902587⟩.

[8] Sansalone M. Impact-echo: the complete story. ACI Struct J 1997;94(6):777–86. http://dx.doi.org/10.14359/9737 URL ⟨http://www.concrete.org/Publications/ACIMaterialsJournal/ACIJournalSearch.aspx?m=details&ID=9737⟩.
[9] Gibson A, Popovics J. Lamb wave basis for impact-echo method analysis. J Eng Mech 2005;1–6. doi: http://dx.doi.org/10.1061/(ASCE)0733-9399(2005)131:4(438). URL ⟨http://ascelibrary.org/doi/abs/10.1061/(ASCE)0733-9399(2005)131:4(438)⟩.
[10] Clorennec D, Prada C, Royer D. Local and noncontact measurements of bulk acoustic wave velocities in thin isotropic plates and shells using zero group velocity Lamb modes. J Appl Phys 2007;101(3):034908. http://dx.doi.org/10.1063/1.2434824 URL ⟨http://link.aip.org/link/JAPIAU/v101/i3/p034908/s1&Agg=doi⟩.
[11] ASTM C 1383, Standard test method for measuring the P-wave speed and the thickness of concrete plates using the impact-echo method, annual book of American society for testing and materials (ASTM) standards.
[12] Popovics J, Song W, Achenbach JD, Lee JH, Andre RF. One-sided stress wave velocity measurement in concrete. J Eng Mech 1998;124(12):1346–53. http://dx.doi.org/10.1061/(ASCE)0733-9399(1998)124:12(1346) URL ⟨http://www.scopus.com/inward/record.url?eid=2-s2.0-0032455153&partnerID=tZOtx3y1http://ascelibrary.org/doi/abs/10.1061/(ASCE)0733-9399(1998)124:12(1346)⟩.
[13] Hu M, Lin Y, Cheng C. Method for determining internal P-wave speed and thickness of concrete plates. ACI Mater J 2006;103(5):327–35. http://dx.doi.org/10.14359/18154 URL ⟨http://www.concrete.org/Publications/ACIMaterialsJournal/ACIJournalSearch.aspx?m=details&ID=18154⟩.
[14] Qixian L, Bungey J. Using compression wave ultrasonic transducers to measure the velocity of surface waves and hence determine dynamic modulus of elasticity for concrete. Constr Build Mater 1996;10(4):237–42. http://dx.doi.org/10.1016/0950-0618(96)00003-7 URL ⟨http://www.sciencedirect.com/science/article/pii/0950061896000037⟩.
[15] Boyd A, Ferraro C. Effect of curing and deterioration on stress wave velocities in concrete. J Mater Civil Eng 2005;(April):153–158. doi:http://dx.doi.org/10.1061/(ASCE)0899-1561(2005)17:2(153). URL ⟨http://ascelibrary.org/doi/abs/10.1061/(ASCE)0899-1561(2005)17:2(153)⟩.
[16] Kim D, Seo W, Lee K. IE–SASW method for nondestructive evaluation of concrete structure. NDT & E Int 2006;39(2):143–54. http://dx.doi.org/10.1016/j.ndteint.2005.06.009 URL ⟨http://linkinghub.elsevier.com/retrieve/pii/S0963869505001003⟩.
[17] Medina R, Bayón A. Elastic constants of a plate from impact-echo resonance and Rayleigh wave velocity. J Sound Vib 2010;329(11):2114–26. http://dx.doi.org/10.1016/j.jsv.2009.12.026 URL ⟨http://linkinghub.elsevier.com/retrieve/pii/S0022460X0901027X⟩.
[18] Ryden N, Park C. A combined multichannel impact echo and surface wave analysis scheme for non-destructive thickness and stiffness evaluation of concrete slabs. In: AS NT, 2006 NDE conference on civil engineering; 2006. p. 247–53. URL ⟨http://scholar.google.com/scholar?hl=en&btnG=Search&q=intitle:A+Combined+Multichannel+Impact+Echo+and+Surface+Wave+Analysis+Scheme+for+Non-destructive+Thickness+and+Stiffness+Evaluation+of+Concrete+Slabs#0⟩.
[19] Barnes CL, Trottier J-F. Hybrid analysis of surface wavefield data from Portland cement and asphalt concrete plates. NDT & E Int 2009;42(2):106–12. http://dx.doi.org/10.1016/j.ndteint.2008.10.003 URL ⟨http://linkinghub.elsevier.com/retrieve/pii/S0963869508001217⟩.
[20] Schubert F, Wiggenhauser H, Lausch R. On the accuracy of thickness measurements in impact-echo testing of finite concrete specimens—numerical and experimental results. Ultrasonics 2004;42(1–9):897–901. http://dx.doi.org/10.1016/j.ultras.2004.01.076 URL ⟨http://www.ncbi.nlm.nih.gov/pubmed/15047403⟩.
[21] Abraham O, Leonard C, Cote P, Piwakowski B. Time frequency analysis of impact-echo signals: numerical modeling and experimental validation. ACI Mater J 2000;97:645–57. http://dx.doi.org/10.14359/9978 URL ⟨http://www.concrete.org/Publications/ACIMaterialsJournal/ACIJournalSearch.aspx?m=details&ID=9978⟩.
[22] Algernon D, Wiggenhauser H. Impact echo data analysis based on Hilbert–Huang transform. Transp Res Rec 2007;2028(1):146–53. http://dx.doi.org/10.3141/2028-16 URL ⟨http://www.scopus.com/inward/record.url?eid=2-s2.0-41549088922&partnerID=tZOtx3y1⟩.
[23] Medina R, Garrido M. Improving impact-echo method by using cross-spectral density. J Sound Vib 2007;304(3–5):769–78. http://dx.doi.org/10.1016/j.jsv.2007.03.019 URL ⟨http://linkinghub.elsevier.com/retrieve/pii/S0022460X07001824⟩.
[24] Zywicki D, Rix G. Mitigation of near-field effects for seismic surface wave velocity estimation with cylindrical beamformers. J Geotech Geoenviron Eng 2005;(August):970–977. doi:http://dx.doi.org/10.1061/(ASCE)1090-0241(2005)131:8(970). URL ⟨http://ascelibrary.org/doi/abs/10.1061/(ASCE)1090-0241(2005)131:8(970)⟩.
[25] Roesset J, Chang D, Stokoe K, Aouad M. Modulus and Thickness of the Pavement Surface Layer from SASW Tests. Transp Res Rec 1990;1260:53–63.
[26] Roesset J. Nondestructive dynamic testing of soils and pavements. Tamkang J Sci Eng 1998;1(2):61–80 URL ⟨http://www.researchgate.net/publication/237809455_Nondestructive_Dynamic_Testing_of_Soils_and_Pavements/file/72e7e52a9e73922ae7.pdf⟩.
[27] Ditri J, Pilarski A. Generation of guided waves in a plate by axisymmetric normal surface loading. In: Review of progress in quantitative nondestructive evaluation, vol. 13. URL ⟨http://books.google.com/books?hl=en&lr=&id=RWulSz94GPAC&oi=fnd&pg=PA133&dq=Generation+of+Guided+waves+in+a+plate+by+axisymnetric+normal+surface+loading&ots=CsnCME1_0P&sig=_5TG40-ePmiFOh187QJ4o5t5WBw⟩.
[28] Bodet L, Abraham O, Clorennec D. Near-offset effects on Rayleigh-wave dispersion measurements: physical modeling. J Appl Geophys 2009;68(1):95–103. http://dx.doi.org/10.1016/j.jappgeo.2009.02.012 URL ⟨http://www.scopus.com/inward/record.url?eid=2-s2.0-67349207134&partnerID=tZOtx3y1⟩.
[29] Achenbach JD. Wave propagation in elastic solids. Amsterdam, London: North-Holland Publishing Company; 1973.
[30] Comsol Inc, Comsol Multiphysics, 2014. URL ⟨http://www.comsol.com⟩.
[31] Ryden N, Castaings M, Thompson DO, Chimenti DE. An adaptive frequency domain finite element model for surface wave testing of pavements. AIP Conf Proc 2009;1096:1481–8. doi:http://dx.doi.org/10.1063/1.3114132. URL ⟨http://link.aip.org/link/APCPCS/v1096/i1/p1481/s1&Agg=doi⟩.
[32] Castaings M, Bacon C, Hosten B, Predoi MV. Finite element predictions for the dynamic response of thermo-viscoelastic material structures. J Acoust Soc Am 2004;115(3):1125. http://dx.doi.org/10.1121/1.1639332 URL ⟨http://www.scopus.com/inward/record.url?eid=2-s2.0-1542376817&partnerID=tZOtx3y1⟩.
[33] Park CB, Miller RD, Xia J. Multichannel analysis of surface waves. Geophysics 1999;64(3):800–8. http://dx.doi.org/10.1190/1.1444590 URL ⟨http://library.seg.org/doi/abs/10.1190/1.1444590⟩.
[34] Ryden N, Park CB, Ulriksen P, Miller RD. Multimodal approach to seismic pavement testing. J Geotech Geoenviron Eng 2004;130(6):636–45. http://dx.doi.org/10.1061/(ASCE)1090-0241(2004)130:6(636) URL ⟨http://www.scopus.com/inward/record.url?eid=2-s2.0-2942608989&partnerID=tZOtx3y1⟩.
[35] Sheriff RE. Encyclopedic dictionary of exploration geophysics, geophysical references series, vol 1. Society of Exploration, Tulsa; 1991.

Appendix B

Paper II

O. Baggens and N. Ryden. 2015.
Poisson's ratio from polarization of acoustic zero-group velocity Lamb mode.
The Journal of the Acoustical Society of America, 138(1):EL88-EL92.
DOI: 10.1121/1.4923015.

Poisson's ratio from polarization of acoustic zero-group velocity Lamb mode

Oskar Baggens[a] **and Nils Ryden**
Division of Engineering Geology, Lund University, P.O. Box 118, SE-22100, Lund, Sweden
oskar.baggens@tg.lth.se, nils.ryden@tg.lth.se

Abstract: Poisson's ratio of an isotropic and free elastic plate is estimated from the polarization of the first symmetric acoustic zero-group velocity Lamb mode. This polarization is interpreted as the ratio of the absolute amplitudes of the surface normal and surface in-plane components of the acoustic mode. Results from the evaluation of simulated datasets indicate that the presented relation, which links the polarization and Poisson's ratio, can be extended to incorporate plates with material damping. Furthermore, the proposed application of the polarization is demonstrated in a practical field case, where an increased accuracy of estimated nominal thickness is obtained.

[JM]
Date Received: March 20, 2015 **Date Accepted:** June 7, 2015

1. Introduction

The fascinating properties of acoustic zero-group velocity (ZGV) Lamb modes[1,2] have been demonstrated to be useful in several applications, such as measurements of acoustic bulk wave velocities and Poisson's ratio,[3] thin-layer thickness,[4] hollow cylinders,[5] interfacial bond stiffness,[6] and possibly air-coupled measurements.[7] In this study, we present a novel application of the amplitude ratio of the surface normal and the surface in-plane components, and demonstrate how it can be used to estimate Poisson's ratio. This investigation was carried out from the perspective of non-destructive testing of concrete structures under one-sided access test conditions, but our observations are also valid for any material and structure for which Lamb wave theory is a representative assumption.

The evaluation of the dynamic response to a transient impact is a common technique for estimation of the thickness and/or mechanical properties of plate-like concrete structures. This type of acoustic measurement technique, often referred to as an impact-echo measurement,[8] employs the ZGV resonance frequency of the first symmetric (S1) Lamb mode.[9] To determine the thickness and/or mechanical properties, the frequency of the S1-ZGV mode must be complemented with two additional parameters, e.g., transverse wave speed and Poisson's ratio.[10] Combined impact-echo and surface wave measurements,[11] where Poisson's ratio typically is determined from the longitudinal wave and the Rayleigh wave velocity,[12] can be used to obtain these two additional parameters. However, systematic errors from near-field effects and velocity variation through the thickness can lead to an uncertain estimation of Poisson's ratio.[11]

Alternative approaches that do not depend on an estimation of the longitudinal wave velocity are therefore important for accurate estimation of Poisson's ratio. One alternative strategy is to use the ratio between the S1-ZGV frequency and the minimum frequency of the second anti-symmetric Lamb mode.[3] This approach has been demonstrated successfully for several thin homogenous metal plates,[3] but only a few measurements have been reported for concrete plates.[13]

To date, there is a lack of techniques that are independent of longitudinal wave velocity and that can accurately determine Poisson's ratio for concrete plates with only one accessible side. An interesting alternative is based on the polarization of Rayleigh waves.[14] Inspired by this idea of using polarization to estimate Poisson's ratio, here we propose and explore a new approach for estimating Poisson's ratio based on the polarization and shape of the S1-ZGV Lamb mode. An advantage of this new approach is that a through-thickness representative estimation of Poisson's ratio is obtained, since the S1-ZGV mode exists through the entire thickness of the plate.

This study is divided into three parts. We first present the theoretical foundation for this approach. We then verify the presented approach using a set of numerical simulations. Finally, we demonstrate the utility of this approach in a realistic field case.

[a]Author to whom correspondence should be addressed.

2. Amplitude polarization of Lamb mode

According to Lamb wave theory, which defines linear elastic wave propagation along isotropic infinite plates, the possible combinations of angular frequencies ω and lateral wave numbers k that can exist in a free plate with a height h is defined by[10]

$$\frac{\tan(\beta h/2)}{\tan(\alpha h/2)} = -\left[\frac{4\alpha\beta k^2}{(k^2-\beta^2)^2}\right]^{\pm 1}, \tag{1}$$

where

$$\alpha^2 = \omega^2/V_L^2 - k^2,$$
$$\beta^2 = \omega^2/V_T^2 - k^2.$$

V_L and V_T are the longitudinal and transversal wave velocities, respectively. The positive sign of the exponent on the right side of Eq. (1) defines symmetric modes, whereas the negative sign defines anti-symmetric modes. The wave number k can be used to determine the displacement field of the plate. The amplitude for the displacement at the free surface for the surface in-plane U and surface normal W directions are given by[10]

$$U = ck\left(\frac{1}{\tanh(qh/2)} - \frac{2qs}{k^2+s^2}\frac{1}{\tanh(sh/2)}\right), \tag{2}$$

$$W = -cq\left(1 - \frac{2k^2}{k^2+s^2}\right), \tag{3}$$

where c is an arbitrary multiplicative constant. The parameters q and s are calculated according to

$$q = \sqrt{k^2 - k_L^2}, \quad s = \sqrt{k^2 - k_T^2},$$

where k_L and k_T are the longitudinal and transversal wave number, respectively.

Equation (1) was used to find the frequencies ω and wave numbers k of the S1-ZGV points corresponding to each value of Poisson's ratio ν in the range 0.1 to 0.4, with increments of 0.01. Variations in $|U|$ and $|W|$ as a function of ν are shown in Fig. 1(a). The arbitrary constant c, in this case the scaling of the curves, is selected to yield an amplitude of 1 for $|W|$ at $\nu = 0.1$. Figure 1(b) displays the variation of the absolute ratio $|W/U|$ as a function of ν. This dimensionless quantity, which can be interpreted as the polarization of the S1-ZGV Lamb mode, is only dependent on ν, thus providing an opportunity to estimate ν if the polarization is measured. This relation is critical to the proposed approach.

3. Numerical modeling

The relation in Fig. 1(b) is calculated without including material damping. However, in many practical applications such as measurements of concrete structures, material damping is present; from a theoretical point of view, true ZGV Lamb modes are in these cases strictly not defined.[15] For this reason, practical measurements were simulated to investigate whether the polarization relation in Fig. 1(b) can be used to estimate ν even though material damping is present. For simplicity, we hereafter use the S1-ZGV abbreviation to refer to the first thickness resonance of the plate, although, as mentioned previously, no true ZGV modes are strictly defined for absorbing plates.

An axially symmetric finite-element model was created with unit values for the thickness $h = 1$ m, Young's modulus $E = 1$ Pa, and density $\rho = 1\,\text{kg/m}^3$. Note that the analysis results of the simulations are independent of the exact values of h, E, ρ. Poisson's ratio was varied from 0.1 to 0.4, with increments of 0.01, and the loss factor

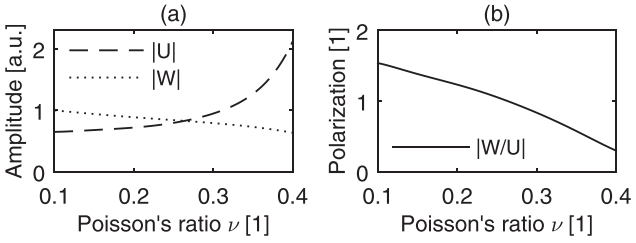

Fig. 1. (a) Absolute values of amplitudes components of S1-ZGV mode. (b) Polarization of S1-ZGV mode.

η was varied from 0 to 0.05, with increments of 0.01. A short line load starting at the axial symmetric axis and with a length of $0.02h$ was applied at the top surface to simulate an applied point load. Since the S1-ZGV frequency is dependent on ν, the center frequency of the load (Gaussian mono pulse) was set equal to the theoretical S1-ZGV frequency for the corresponding plate without material damping. The model was solved in the frequency domain using a frequency-dependent mesh and absorbing region.[16] The time domain response was obtained from the inverse discrete Fourier transform of the frequency domain response.

Synthetic datasets were created for all combinations of varying ν and η. Figure 2(a) contains the dataset for $\nu = 0.1$ and $\eta = 0.01$. In this plot, the normalized time history (y axis) of the surface in-plane acceleration response is shown for various normalized radial offset locations r/h (x axis) at the top accessible surface. Each dataset consisted of ten signals per length h within a radial distance of $4h$ from the axial symmetry axis. Similar to field measurements employing an impact point source, the broad frequency spectrum of the Gaussian mono pulse excites several Lamb modes. To reduce the influence from direct surface waves and enhance low group velocity modes (e.g., S1-ZGV), all signals were individually multiplied with a Tukey window. Figure 2(b) shows the amplitude of the window as function of time. The raw signals along with the windowed signals are shown in Fig. 2(a).

The mode shape at the S1-ZGV frequency was extracted using a temporal discrete Fourier transform of the windowed dataset. Figure 2(c) shows the absolute amplitude of the extracted mode at the S1-ZGV frequency for the surface in-plane and surface normal components as a function of the normalized radial distance r/h for the dataset with $\nu = 0.1$ and $\eta = 0.01$. Since the surface in-plane and surface normal components are not in phase, the polarization cannot be determined from two point-wise amplitudes at a fixed radial offset from Fig. 2(c) in a straightforward fashion. Instead, the spatial periodicity and amplitude for the total mode is used for simplicity and robustness. For straight crested Lamb waves, the spatial periodicity is defined by the exponential function. However, in this case, Hankel functions are used to account for cylindrical spreading from a point source.[17] Accordingly, the analytical expressions for the absolute amplitude of the S1-ZGV mode shape as function of amplitudes U, W, wave number k, and radial distance r take the form

$$A(U,k,r) = |\Re(|U|\mathrm{H}_1^{(1)}(kr)\mathrm{e}^{\mathrm{i}\arg(\mathrm{k})})|, \tag{4}$$

$$B(W,k,r) = |\Re(|W|\mathrm{H}_0^{(1)}(kr))|, \tag{5}$$

where A and B represent the surface in-plane and surface normal components, respectively. $H_1^{(1)}$ and $H_0^{(1)}$ are the first and zeroth-order Hankel functions of the first kind, respectively. We allow k to be complex-valued to account for material damping. The

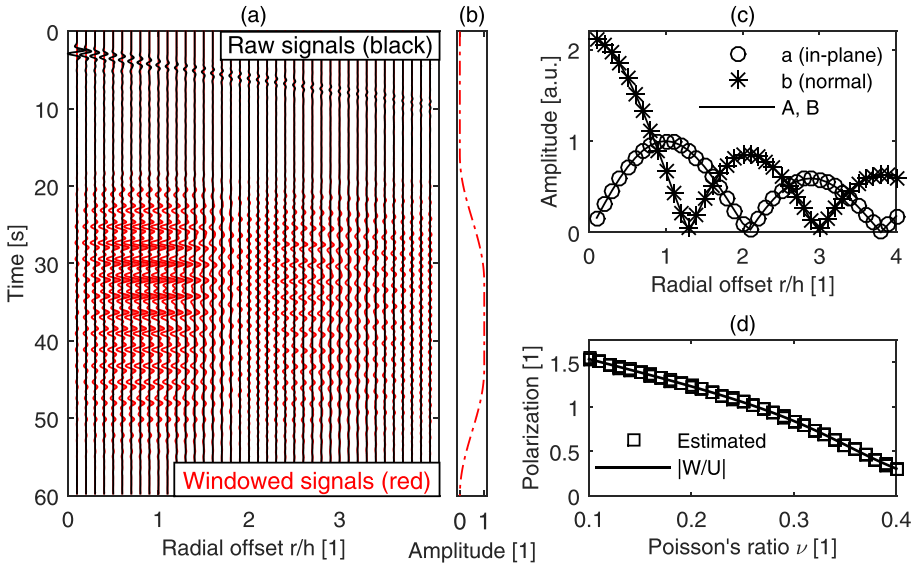

Fig. 2. (Color online) (a) Simulated multichannel dataset (surface in-plane component, $\nu = 0.1$, $\eta = 0.01$). (b) Tukey-window amplitude. (c) Absolute amplitude of extracted S1-ZGV mode (markers) and best solution (lines). (d) Estimated polarization (markers) and theoretical relation for lossless plates (solid line).

exponential term $e^{i\arg(k)}$ in Eq. (4) is introduced to maintain zero displacement at the axial symmetry axis ($r = 0$) when k is complex.

The absolute amplitudes $|U|$, $|W|$ and wave number k for the S1-ZGV mode of the simulated plate were estimated by searching for the best match between the analytic expressions in Eqs. (4) and (5) and the extracted mode shape [markers in Fig. 2(c)]. This search was carried out by minimizing the objective function

$$f(U, W, k, r) = \sum_{i=1}^{N} \left(\frac{(a_i - A_i)^2}{|U|} + \frac{(b_i - B_i)^2}{|W|} \right), \tag{6}$$

where a_i and b_i are the absolute amplitudes of the surface in-plane and surface normal components of the extracted mode, respectively [markers in Fig. 2(c)]. The index $i = 1, 2, \ldots, N$ labels the simulated signals, where $i = 1$ represents the signal nearest the impact point. A_i and B_i represents the functions from Eqs. (4) and (5) calculated at the radial offset $r = r_i$, i.e., $A_i = A(U, k, r = r_i)$ and $B_i = B(W, k, r = r_i)$. The function f was minimized by means of unconstrained nonlinear optimization using the *fmin-search* function available in MATLAB. Good agreement was obtained between the best solution to the minimization problem and the extracted mode [Fig. 2(c)]. The polarization was determined using $|W|$ and $|U|$ from this solution. This analysis, which enables the estimation of polarization, was repeated for each dataset (i.e., the simulated response to an impact pulse for the plate with varying combinations of ν and η). Figure 2(d) contains the estimated values of polarization for all datasets as well as the analytical relation [from Fig. 1(b)] calculated for lossless material. Good agreement exists between the analytical expression for the polarization and the simulated results. Note that the results from simulations that included material damping also match the analytical expression. Hence, the proposed approach is likely applicable to plates with material damping.

4. Field case

The proposed approach was tested on a concrete wall with a nominal thickness of 0.450 m. A three-component accelerometer attached to a fixed position on the wall was used to measure the response from hammer strokes performed at increasing offsets from the accelerometer. The input force from each stroke was also recorded. By using the reciprocity theorem for a linear elastic system, a multichannel dataset was obtained.[11] This dataset is of the same type as the simulated datasets in Sec. 3 and was processed in a similar way: a Tukey window was applied in the time domain, and then the absolute amplitude of the transfer function between the source and the receiver at the S1-ZGV frequency was extracted [Fig. 3(a)]. The objective function f from Eq. (6) was minimized using the same technique as in Sec. 3. Figure 3(a) illustrates the matched functions A and B.

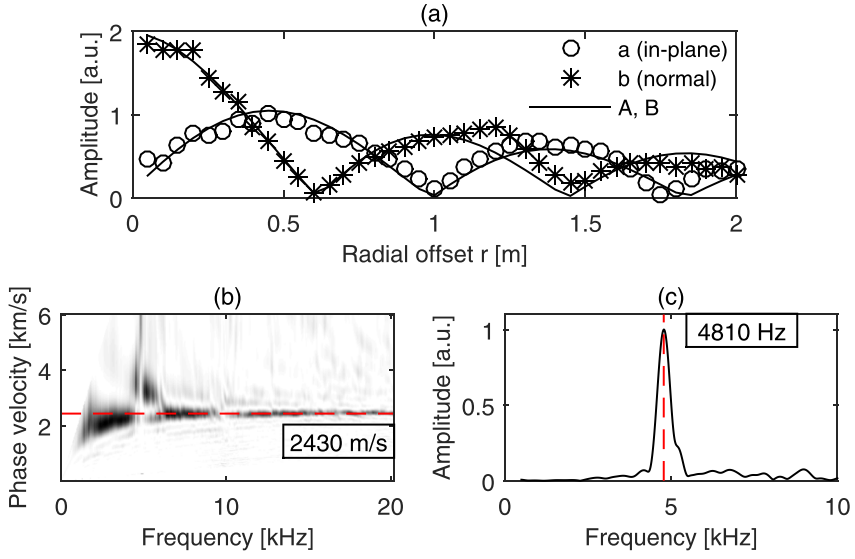

Fig. 3. (Color online) (a) Absolute amplitude of extracted S1-ZGV mode (markers) and best solution (lines). (b) Frequency-phase velocity spectrum, and estimated Rayleigh wave velocity (dashed line). (c) Frequency spectrum of (windowed) surface normal component signal nearest impact point (solid line), and estimated S1-ZGV frequency (dashed line).

The polarization $|W/U|$ was estimated as 1.09, yielding $\nu = 0.24$. Unfortunately, no exact value of ν is accessible for comparison. However, the estimation of ν can be verified indirectly to a certain extent from the nominal thickness of the wall $h = 0.450$ m. Estimation of the Rayleigh wave velocity (2430 m/s) from the raw signals displayed in frequency-phase velocity domain [Fig. 3(b)], the S1-ZGV frequency (4810 Hz) from the frequency spectrum of the windowed signal nearest the impact point [Fig. 3(c)], and Poisson's ratio (0.24) theoretically corresponds to a thickness of 0.447 m, which is within 1% error of the nominal thickness. The traditional approach[11] using the longitudinal wave velocity (4295 m/s) and Rayleigh wave velocity (2430 m/s), i.e., $\nu = 0.18$, theoretically corresponds to a thickness of 0.425, which is within 6% error of the nominal thickness. Thus, in this field case, our proposed approach provides a reasonable estimate of ν and an increased accuracy of the estimated nominal thickness, compared with the traditional approach.

5. Conclusions

Here we have presented a new approach to estimating Poisson's ratio from the amplitude polarization of the S1-ZGV Lamb mode. Numerical simulations demonstrated that this approach is also applicable to plates with material damping. A field-case example illustrated a benefit of this approach: a through-thickness representative value for Poisson's ratio is obtained via this strategy, thereby improving the overall estimation of plate parameters under one-sided access test conditions.

Acknowledgments

The Development Fund of the Swedish Construction Industry (SBUF, No. 12534) and The Swedish Radiation Safety Authority (SSM, No. SSM2012-890) are acknowledged for financing the study.

References and links

[1]E. Kausel, "Number and location of zero-group-velocity modes," J. Acoust. Soc. Am. **131**(5), 3601–3610 (2012).
[2]C. Prada, D. Clorennec, and D. Royer, "Local vibration of an elastic plate and zero-group velocity Lamb modes," J. Acoust. Soc. Am. **124**(1), 203–212 (2008).
[3]D. Clorennec, C. Prada, and D. Royer, "Local and noncontact measurements of bulk acoustic wave velocities in thin isotropic plates and shells using zero group velocity Lamb modes," J. Appl. Phys. **101**(3), 034908 (2007).
[4]M. Cès, D. Clorennec, D. Royer, and C. Prada, "Thin layer thickness measurements by zero group velocity Lamb mode resonances," Rev. Sci. Instrum. **82**(11), 114902 (2011).
[5]M. Cès, D. Royer, and C. Prada, "Characterization of mechanical properties of a hollow cylinder with zero group velocity Lamb modes," J. Acoust. Soc. Am. **132**(1), 180–185 (2012).
[6]S. Mezil, J. Laurent, D. Royer, and C. Prada, "Non contact probing of interfacial stiffnesses between two plates by zero-group velocity Lamb modes," Appl. Phys. Lett. **105**(2), 021605 (2014).
[7]S. D. Holland and D. E. Chimenti, "Air-coupled acoustic imaging with zero-group-velocity Lamb modes," Appl. Phys. Lett. **83**(13), 2704–2706 (2003).
[8]M. J. Sansalone and W. B. Streett, *Impact-Echo: Non-Destructive Evaluation of Concrete and Masonry* (Bullbrier Press, Jersey Shore, PA, 1997).
[9]A. Gibson and J. S. Popovics, "Lamb wave basis for impact-echo method analysis," J. Eng. Mech. **131**, 438–443 (2005).
[10]I. A. Viktorov, *Rayleigh and Lamb Waves Physical Theory and Applications* (Plenum Press, New York, 1967).
[11]O. Baggens and N. Ryden, "Systematic errors in Impact-Echo thickness estimation due to near field effects," NDT & E Int. **69**, 16–27 (2015).
[12]T. T. Wu, J. S. Fang, G. Y. Liu, and M. K. Kuo, "Determination of elastic constants of a concrete specimen using transient elastic waves," J. Acoust. Soc. Am. **98**(4), 2142–2148 (1995).
[13]A. Gibson, "Advances in nondestructive testing of concrete pavements," Ph.D. thesis, University of Illinois, Urbana-Champaign, 2004.
[14]A. Bayon, F. Gascon, and F. J. Nieves, "Estimation of dynamic elastic constants from the amplitude and velocity of Rayleigh waves," J. Acoust. Soc. Am. **117**(6), 3469–3477 (2005).
[15]F. Simonetti and M. J. S. Lowe, "On the meaning of Lamb mode nonpropagating branches," J. Acoust. Soc. Am. **118**(1), 186–192 (2005).
[16]M. Castaings, C. Bacon, B. Hosten, and M. V. Predoi, "Finite element predictions for the dynamic response of thermo-viscoelastic material structures," J. Acoust. Soc. Am. **115**(3), 1125–1133 (2004).
[17]J. J. Ditri, A. Pilarski, B. Pavlakovic, and J. L. Rose, "Generation of guided waves in a plate by axisymmetric normal surface loading," in *Review of Progress in Quantitative Nondestructive Evaluation* (Plenum Press, New York, 1994), Vol. 13A.

Appendix C

Paper III

O. Tofeldt and N. Ryden. 2017.
Lamb wave phase velocity imaging of concrete plates with 2D-arrays. Under review, Journal of Nondestructive Evaluation.

Lamb wave phase velocity imaging of concrete plates with 2D arrays

Oskar Tofeldt*, oskar.tofeldt@tg.lth.se, Tel. +46 (0)46 222 0000
Nils Ryden, nils.ryden@tg.lth.se

(Affiliation and address for both authors)
Division of Engineering Geology, Lund University
P.O. Box 118, SE-22100, Lund, Sweden

*Corresponding author

Abstract

In the nondestructive evaluation of concrete structures, ultrasonic techniques are considered to be more capable than low-frequency techniques such as the impact-echo method. This is especially true with the recent development of ultrasonic transducers, synthetic apertures, and results in an image form, and because low-frequency techniques are usually limited in their evaluation to the frequency of one single resonant mode. With the aim of reducing this gap in capabilities, we present a 2D array and wide-frequency bandwidth technique for Lamb wave phase velocity imaging. The presentation involves a measurement on a newly cast concrete plate using a hammer and an accelerometer as an example. The key concept of the technique is the use of 2D arrays that record a full wave field response over a limited surface subdomain within the complete measurement domain. Through a discrete Fourier transform, a spectral estimate is obtained for the 2D array in the frequency-phase velocity domain. The variation of the phase velocity is then mapped using a stepwise movement of the 2D array within the complete measurement domain. With two different types of 2D arrays, the variation of the phase velocity for the A0 Lamb mode is mapped and displayed in a polar and image plot, and low variation is observed for both cases. This result verifies the expected condition of a homogenous material and plate thickness and, more importantly, highlights the potential of wide-frequency bandwidth techniques based on full wave field data.

Keywords: Lamb waves; imaging; 2D arrays; concrete; impact-echo; full wave field data

1. Introduction

Nondestructive evaluation (NDE) techniques used on concrete structures can facilitate structural inspections, improve quality control, and support the sustainable use of resources [1]. Measurements based on vibrations and acoustic waves are frequently used to assess the mechanical properties in these structures. Such measurements are typically categorized based on their operating frequency, with ultrasonic methods as a major group. As a complement to the predominant use of ultrasonic reflection imaging approaches, we present a Lamb wave phase velocity imaging technique based on a full wave field response. Compared to ultrasonic approaches, this technique operates in a lower frequency regime and with a wider frequency content.

Ultrasonic testing allows the interior of a concrete construction element to be examined and visualized in the form of an reflection image [2, 3]. In this process, internal objects and anomalies such as defects appear as points or regions with deviating color. Techniques such as synthetic aperture focusing have made ultrasonic testing an effective, widely used, and powerful NDE approach for concrete structures. Recent progress has been made with this type of testing. One example is the development of wireless apertures that enable flexible data acquisition over larger areas compared to handheld devices [4]. However, for structures with heavy reinforcement or coarse aggregates, scattering and attenuation are challenges that may hinder the evaluation and reduce the ability to create a reflection image [3–6]. Since scattering and attenuation are related to the wavelength and number of cycles along the path of the ultrasonic pulse, this may particularly be a problem for high frequencies or thick structures [5].

To reduce the influence from scattering and attenuation, an alternative approach is to operate at a lower frequency regime, which leads to the usage of a longer spatial wavelength. This can, for instance, be achieved using a mechanical impactor as an input pulse source instead of an ultrasonic transducer. Based on this concept, the impact-echo (IE) method is a common and established technique for testing concrete structures [7]. In this method, an impact is applied to the surface using, for example, a hammer or a steel ball to generate a transient pulse with broadband frequency content. Ideally, the structural response to this transient excitation is dominated by a reverberating mode with a distinct frequency dependent on the material properties and geometry; i.e., the procedure corresponds to a general resonance test. Faults and anomalies can be detected by analyzing and monitoring the relative variation of the response along the surface. This procedure can be further extended with automatic data acquisition [8] and air-coupled sensors [9, 10] to generate a frequency image showing the relative variation of the response over a surface [8, 9].

There has been an improved understanding of the mechanism in IE testing over time. Whereas early studies interpreted the resonance mode as a discrete pulse with multiple reflections between the structural interfaces [7], more recent studies link the reverberating mode to the general theory of Lamb waves [11]. By showing that the resonance mode in IE testing corresponds to the first symmetric zero-group velocity (S1-ZGV) Lamb mode [11, 12], an important relationship to Lamb waves can be established. With this relationship determined at the outset and using the theoretical basis of Lamb wave theory, ongoing developments have advanced techniques that combine evaluation of the S1-ZGV Lamb mode frequency with propagating surface waves [13–17]. Such techniques, which use both propagating and nonpropagating modes with an analysis based on Lamb wave theory, enable a direct quantitative estimation of plate thickness and material velocity in absolute values; this differs from the original IE method that requires either a calibration sample or correction factor to provide the corresponding result [17]. In addition to quantitative estimations, the Lamb wave interpretation also facilitates the improved detectability and accuracy of the S1-ZGV frequency [18, 19] and enables an evaluation of Poisson's ratio [20] from the characteristics of the S1-ZGV Lamb mode shape.

Clearly, the results in the literature demonstrate the potential for using Lamb waves in the nondestructive evaluation of plate-like concrete structures. At present, these techniques are still mainly based on an evaluation at multiple discrete points [7, 8] or, in some cases, along line arrays with equidistant impact (signal) spacing [15]. Naturally, there is no prerequisite or limitation that only these two types of geometrical domains (point and line) can be used; other layouts have been observed in related applications such as geophysical investigations with surface waves [21] and Lamb wave testing of aluminum plates [22]. Thus, to improve the verification of the spatial distribution of results in the testing of plate-like concrete structures, a prospective methodology is to perform a

Lamb wave analysis with a two-dimensional (2D) surface considered in both the data collection and the data evaluation. To the authors' best knowledge, no examples of such an analysis with Lamb waves in the testing of plate-like concrete structures have been reported in the literature. This highlights the need for further investigations and serves as the motivation for the present study.

In this study, we demonstrate and describe a new technique for Lamb wave phase velocity imaging analysis of plate-like concrete structures. The technique is based on a full wave field dataset collected over a surface using an impact hammer and an accelerometer. In contrast to previous studies of concrete plates, which measured stationary modes at multiple discrete points over a surface, the novel aspect of this technique is that it evaluates propagating waves in multiple 2D subdomains (2D arrays). Flexibility in terms of operating frequency is obtained since the impact source creates a response with wide-frequency bandwidth. As a result, further developments of the presented technique have potential for the evaluation of large structures in which scattering and attenuation may present issues when using ultrasonic approaches.

The paper is organized as follows. In Section 2, we present a practical measurement as an illustrating example for the presented technique. Data processing and implementation of the technique are presented and explained in Section 3. First, data from a line array are processed in a conventional analysis of surface waves; this analysis is based on a 2D Fourier transform for which a discrete implementation is explained. Then, a transformation technique that converts data to a radial-offset domain is presented. The transformation allows the analysis of the data from the 2D arrays; as example, we analyze the phase velocity for the A0 Lamb mode and present the results in a polar and image plot. Finally, concluding remarks are provided in Section 4.

2. Method and measurement

We perform a measurement on a newly cast concrete slab that serves as the foundation and ground for a future school building. The entire slab (building) is approximately rectangular in shape with length 60 m and width 17 m. No joints appear within the extent of these outer boundaries; i.e., the slab is cast in a continuous assembly. The slab has a uniform nominal thickness of 0.12 m, except along the walls and bases of columns the thickness is increased to enhance the load-carrying capacity. More specifically, the measurement data in this study are acquired inside a rectangle with length 4 m and width 1.8 m. This rectangle is shown and highlighted in green in Fig. *1*(a). In turn, this rectangle is located in the center of a room with length 8.1 m and width 6 m, shown in Fig. *1*(a). The nominal thickness of the slab in the room follows the uniform standard value of 0.12 m, except along the top, left, and bottom edges of the room (gray color in Fig. *1*(a)) where the thickness is increased to 0.32 m to support the load from the inner walls. Along the right edge of the room, which also is at the edge of the slab (gold color in Fig. *1*(a)) and the outer wall, the nominal thickness is increased to 0.5 m. Except at this right edge of the room (slab edge), the distances to the outside edges of the slab are a minimum of 9 m. Thus, the location of the measurement ensures low influence from reflections caused by free slab edges. Moreover, since a newly cast plate is studied, it is expected that the slab will have uniform material properties and thickness and will be free of anomalies and defects. The measurement location is selected in order to create a controlled and reliable test environment that facilitates the development of new processing techniques without introducing excessive uncertainties.

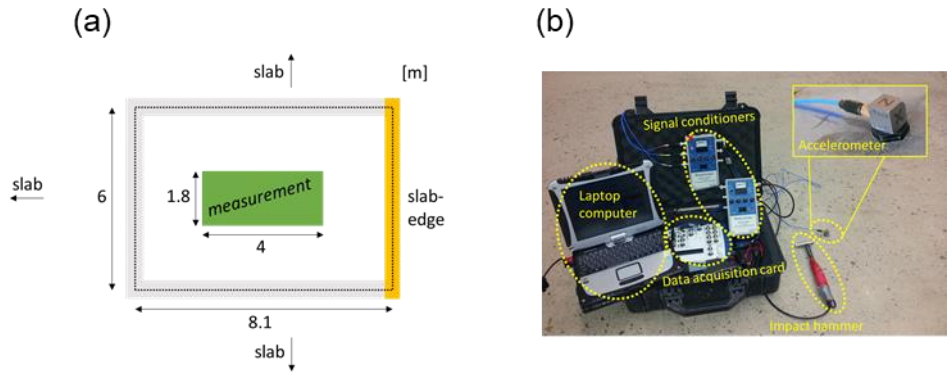

Fig. 1 (a) Sketch of measurement domain and (b) overview of measurement equipment

Measurement data are collected with portable equipment consisting of a three-component accelerometer (PCB model 356A15), impact hammer (PCB model 086C03), signal conditioners (PCB model 480b21), data acquisition card (NI USB-6251 BNC), and laptop computer. An overview of the equipment is shown in Fig. *1*(b). The collected data are composed of the vibration responses recorded by the accelerometer due to impacts made with the hammer. Responses from 1040 impacts are recorded at positions shown in Fig. *2*(a) as black dots. The accelerometer remains at a fixed position during the measurement, and it is marked with a red cross in the center of the measurement domain shown by the green rectangle in Fig. *2*(a) and (b). Fig. *2*(a) and (b) also show the orientation of the xyz-domain assigned to the measurement. For the direction parallel to the x-axis, the impact points appear at x-coordinates from +-0.05 m to +-2 m with offset intervals of 0.05 m between the points; note that no impact points appear along the line x = 0. For the direction parallel to the y-axis, impact points appear at y-coordinates from -0.9 m to +0.9 m with offset intervals of 0.15 m between the points. Fig. *2*(b) shows a photograph of the slab taken during the measurement. This figure depicts the rectangle (green color), the accelerometer (red cross), the coordinate system (yellow dotted lines), and the edge of the rectangular domain (yellow solid lines). For brevity, the 1040 impact points are not highlighted in Fig. *2*(b).

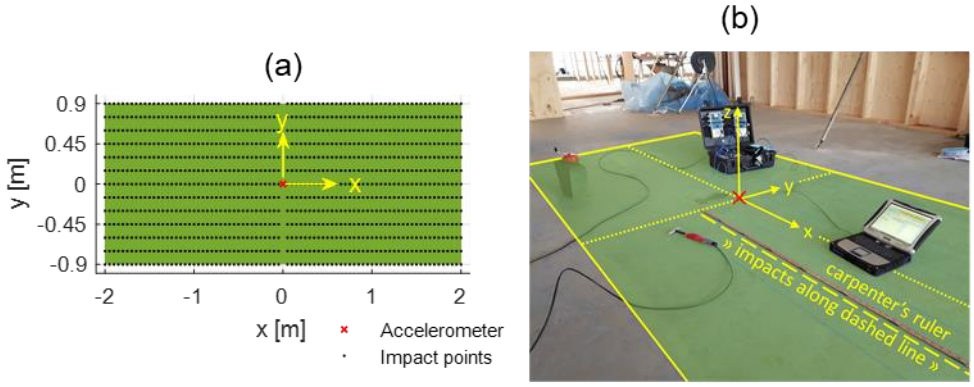

Fig. 2 (a) Measurement domain and associated coordinate system and (b) photograph from measurement with illustration of coordinate system and practical execution

Planning and organization are important in the collection of a large number of impact responses. In our case, we divide the 1040 points into 26 lines, each containing 40 impact points. Fig. *2*(b) shows an example of a line that is illustrated with yellow dashed markings. Along the line, 40 impacts are performed from left to right, covering a distance of $40 \cdot 0.05 = 2$ m. This corresponds to half of the rectangular domain length of 4 m. The 0.05 m offset distance between each point along the x-direction is maintained with guidance from the carpenter's ruler placed adjacent to the line; see Fig.

2(b). The process is then continued by marking a new line, for instance with a chalk line as used here, and thereafter collecting of a new set of 40 impacts. The described procedure is repeated 26 times in total, thus producing the 1040 impact points. Accordingly, it can be observed that the overall process corresponds to a series of measurements that are similar to those used in a multichannel analysis of surface waves (MASW) [23]. In the current measurement, each line requires approximately 5 minutes working time to mark the line and perform the impacts. Thus, 2–3 hours of effective working time are required to collect the complete dataset of 1040 impacts. It should be mentioned that a major part of this effective working time is spent on marking the appropriate location of the lines; typically, the impacts themselves are easily performed in a short amount of time.

For studies of vibrating systems, the coupling condition of the accelerometer is a crucial issue. In this study, the accelerometer is mounted with glue at the center of the rectangular domain (Fig. *2*(a) and (b), red cross) and it is kept in this position throughout the entire course of the measurement. This ensures a consistent coupling condition at the receiving end of the measurement system for all 1040 impacts, and it means that measurement uncertainty, except for electrical noise, is mainly generated at the sending end due to the potential variation in the coupling condition of the hammer impacts. In addition to generating the vibrations in the plate, the impact hammer also works as a triggering device; thus, reciprocity can be used. In more detail, reciprocity generally states that the response of a linear elastic system measured by an accelerometer at location A due to an impact applied at location B is equal to the response measured from the reciprocal arrangement, with the impact applied at location A and the accelerometer at location B. As a result, we are able to obtain a dataset containing the full wave field response from a transient point source excitation at the position of the accelerometer (Fig. *2*(a) and (b), red cross) recorded with 1040 sensors located at the impact points (Fig. *2*(a), black dots). In the following, this dataset is further studied and analyzed.

3. Data processing and results

The data acquisition card operates at the sampling frequency $f_s = 200$ kHz and a recording length of 20 ms, i.e., a recording length of 4000 samples. With the use of reciprocity, the collected dataset represents the full wave field response due to a point source excitation recorded with an array consisting of 1040 sensors. In the following, the aim is to demonstrate potential processing schemes relevant for this dataset by providing an explanation and details regarding the implementation of these schemes. The 1040 sensors are analyzed by dividing them into subsets of smaller groups. Accordingly, the groups can be interpreted as synthetic sensor arrays created by the geometrical shape that defines the group.

For this measurement, since a three-component accelerometer is used, each sensor records three individual signals: the acceleration response in the x-, y-, and z-directions. Thus, the dataset contains 3120 signals in total. In the following analysis, both the surface normal response (z-direction) and the surface in-plane responses (x- and y-directions) are considered. However, note that the presented analysis is not dependent on all components being measured; the adopted methodology is also applicable for data recorded with a conventional single-component accelerometer, which typically measures the surface normal component (z-direction).

3.1 Line array

An array defined by a line enables the study of a wave field in both space and time. In geophysical applications, this is often referred to as multichannel analysis of surface waves (MASW) [23], and similar approaches using this very general type of array are also used to test metal plates [24] and plate-like concrete structures [15]. Typically, for most applications, the arrays are characterized by uniform spatial sensor spacing along a line. In the case of this study, we create the array by selecting

sensors along the positive x-axis; see Fig. *3*(a) in which the blue diamond markers indicate the positions of the sensors and the red cross indicates the location of the transient point source excitation (from reciprocity). The array shown in Fig. *3*(a) consists of 40 sensors located every 0.05 m along the positive x-axis over the range $x = 0.05$ m to $x = 2$ m. For this line array case, we consider the signals containing the surface in-plane (x-direction) acceleration response and the surface normal (z-direction) acceleration response. Thus, the signals containing the acceleration response in the y-direction (transversal surface in-plane response) are ignored and not considered in the following analysis.

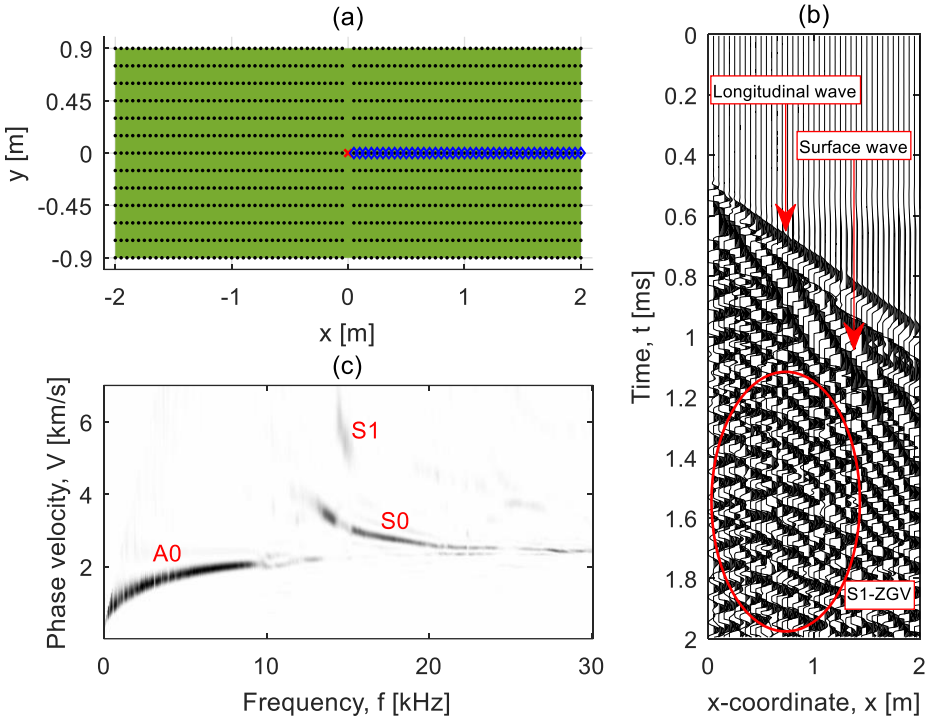

Fig. 3 (a) Measurement domain and line array shown with blue diamond markers, (b) time-domain low-pass filtered surface in-plane acceleration response and wave mode labels, (c) frequency-phase velocity correlation image and Lamb mode labels

Data corresponding to the surface in-plane (x-direction) acceleration response recorded with the array in Fig. *3*(a) are shown in Fig. *3*(b). For improved readability, the presented time domain data are low-pass filtered to reduce the frequency content above 30 kHz. Fig. *3*(b) shows the time history, up to 2 ms, of the signals that represent the surface in-plane acceleration response for all sensors in the array as a function of the x-coordinate of the sensors. This type of plot, sometimes referred to as a wiggle plot or seismic record, allows an initial analysis of the data in both time and space. In Fig. *3*(b), the longitudinal wave can be identified (see marking with arrow). After a time of approximately 1 ms, a stationary mode is observed. This mode corresponds to the S1-ZGV Lamb mode (see marking with ellipse), i.e., the reverberating mode typically analyzed in IE measurements of plates. Between the longitudinal wave and the S1-ZGV Lamb mode, a propagating surface wave can also be noticed (see marking with arrow).

Although the visualization of the data in Fig. *3*(b) possibly allows estimations of both velocity (slope in Fig. *3*(b)) and frequency (periodicity in Fig. *3*(b)), these estimations may be challenging since the recorded wave field consists of multimodal and dispersive Lamb waves that are present simultaneously over a wide frequency range. For this reason, estimations that are more robust are

generally obtained by transforming the data to the frequency domain in both time and space. This can be achieved using a 2D Fourier transform, as given by [25]:

$$S(k,f) = \int_{-\infty}^{+\infty} \int_{-\infty}^{+\infty} s(x,t)\, e^{-2\pi i(ft-kx)} dx\, dt \qquad \text{Eq. 1}$$

where S is the measured response as a function of spatial frequency (wave number) k and temporal frequency f, and s is the recorded vibration as a function of space x and time t. By using a discrete implementation (see Section X) of this transform and the relation $V = f/k$, where V is the phase velocity, the surface in-plane acceleration response is transformed to the frequency-phase velocity domain. The same transformation is also performed for the surface normal acceleration response. Then, a superposition of the transformed surface in-plane and surface normal responses is created and shown in Fig. *3*(c). Basically, Fig. *3*(c) shows the correlation for different combinations of frequencies f and phase velocities V for the data recorded by the array. The dark color indicates strong correlation, whereas the light color indicates weak correlation. In Fig. *3*(c), the two fundamental Lamb modes A0 and S0 can be identified (see markings). In addition, the part of the S1 Lamb mode curve related to the S1-ZGV Lamb mode can also be observed. This type of correlation image can be used to track the dispersive properties of the measured wave field. In other words, a Lamb wave dispersion analysis can be performed and used to evaluate the elastic properties and thickness of the plate [24]. Note that this type of analysis is independent of a priori information about the structure; compared with, for instance, the conventional IE technique [7], no empirical correction factors or calibration values are required [17].

3.2 Two-dimensional discrete Fourier transform

Since no analytical expressions exist for the measured response, the expression in Eq. 1 must be numerically evaluated to create the correlation image in Fig. *3*(c). The literature provides examples of implementing such evaluations [23, 25–29]. Although the format of implementation varies in the literature, the aim of estimating the spectral content in time and space is common. In this study, we adopt a discrete implementation described in a matrix format, since the matrix format is easily modified for arrays with nonuniform sensor spacing. Moreover, this format can be directly implemented in codes such as MATLAB. Here, the line array given by the blue diamond markers in Fig. *3*(a) is used as an illustrating example. However, it is emphasized that the implementation is general and applicable to other line arrays as well.

Let $\boldsymbol{s}[n]$ be a row vector containing the signal recorded by a sensor:

$$\boldsymbol{s}[n] = [s[1] \quad s[2] \quad \cdots \quad s[N]] \qquad \text{Eq. 2}$$

The index $n = 1, 2, \ldots N$ refers to each discrete sample of the signal in time. In this case, the vector $\boldsymbol{s}[n]$ contains $N = 4000$ discrete samples s recorded at time intervals $1/f_s$, where $f_s = 200$ kHz is the temporal sampling frequency. The spatial array consists of sensors that are numbered with index $m = 1, 2, \ldots M$. For the array studied here (blue diamond markers in Fig. *3*(a)), the number of sensors is $M = 40$. The sensors are located at the coordinates given by $x_m = m \cdot 0.05$, where 0.05 is the spatial sampling interval along the x-axis. The y-coordinates are for all sensors $y_m = 0$. An M-by-N matrix $\boldsymbol{S}$ containing the signals $\boldsymbol{s}_m$ for all sensors $m = 1, 2, \ldots M$ in the array is defined by

$$\boldsymbol{S} = \begin{bmatrix} \boldsymbol{s}_1 \\ \boldsymbol{s}_2 \\ \vdots \\ \boldsymbol{s}_M \end{bmatrix} \quad \text{Eq. 3}$$

In this case, the signal $\boldsymbol{s}_1$ corresponds to the sensor located closest to the point source location (red cross at $x = y = 0$ in Fig. *3*(a)), and $\boldsymbol{s}_M = \boldsymbol{s}_{40}$ corresponds to the sensor located farthest away from the point source. That is, the sensor signals in matrix $\boldsymbol{S}$ are sorted according to ascending distance from the point source according to ascending x-coordinates.

For the discrete Fourier transform in the time domain, a complex and discrete test function is defined by

$$\theta_f[n] = e^{-2\pi i\, f_{test}\, n/f_s} \quad \text{Eq. 4}$$

The test function θ_f describes a complex harmonic oscillation with frequency f_{test}. The subscript f indicates that the function is associated with frequency in the time domain. The term n/f_s can be interpreted as the time variable along which the function is periodic. By calculating the test function for $n = 1, 2, \ldots N$, i.e., for the same length and time as the signals $\boldsymbol{s}_m$, a test vector is created by

$$\boldsymbol{\theta}_f = \begin{bmatrix} \theta_f[1] \\ \theta_f[2] \\ \vdots \\ \theta_f[N] \end{bmatrix} \quad \text{Eq. 5}$$

Then, the discrete Fourier transform in the time domain is formulated as

$$\boldsymbol{s}_f = \boldsymbol{S}\boldsymbol{\theta}_f \quad \text{Eq. 6}$$

The resulting column vector $\boldsymbol{s}_f$ with length M contains complex numbers that are related to both the amplitude and phase of the spectral content for each sensor signal $\boldsymbol{s}_m$ at the test frequency f_{test}.

For the discrete Fourier transform in the space domain, a new complex and discrete test function is defined as

$$\theta_{f-V}[x_m] = e^{2\pi i\, f_{test}/V_{test}\, x_m} \quad \text{Eq. 7}$$

The test function θ_{f-V} describes a complex harmonic oscillation defined by the test frequency f_{test} and the test phase velocity V_{test}. The subscript $f - V$ indicates that the function is associated with frequency in time and the phase velocity. As a result, the function is defined by frequency in the space domain given by a test wave number $k_{test} = f_{test}/V_{test}$. This means that the function θ_{f-V} is periodic along the spatial x-axis of the array. The test function is calculated for the x-coordinates of each sensor to create a new test vector:

$$\boldsymbol{\theta}_{f-V} = \begin{bmatrix} \theta_{f-V}[x_1] \\ \theta_{f-V}[x_2] \\ \vdots \\ \theta_{f-V}[x_M] \end{bmatrix} \quad \text{Eq. 8}$$

The discrete Fourier transform in space domain is then given by

$$s_{f-V} = (\boldsymbol{s}_f \oslash \mathrm{abs}(\boldsymbol{s}_f))^{\boldsymbol{T}} \boldsymbol{\theta}_{f-V} \quad \text{Eq. 9}$$

where ⊘ is an element-wise division (Hadamard division) and $\mathrm{abs}(\boldsymbol{s}_f)$ is the absolute value of each element in the vector $\boldsymbol{s}_f$. Here, the element-wise division with the absolute values of the elements in $\boldsymbol{s}_f$ is used as a normalizing operation that removes the dependency on the amplitude of the wave field. Thus, this discrete Fourier transform in the space domain corresponds to an analysis of the phase angles of the complex elements in vector $\boldsymbol{s}_f$. This means that the magnitude of the resulting transformation given by s_{f-V} represents a measure of the correlation showing the extent to which a wave mode with frequency f_{test} and phase velocity V_{test} exists in the recorded wave field. The subscript $f-V$ is used to symbolize the association with both frequency f and phase velocity V. In the implementation presented here, s_{f-V} represents a complex scalar value. Thus, for the creation of a correlation image as presented in Fig. *3*(c), the above steps may be repeated over a range of combinations of test frequencies f_{test} and test phase velocities V_{test}.

In this example, the correlation image in Fig. *3*(c) is created by calculating s_{f-V} for both the surface in-plane (x-direction) and the surface normal (z-direction) responses. The transformed responses are then combined in the correlation image to $(|s_{f-V,\mathrm{in-plane}}|+|s_{f-V,\mathrm{normal}}|)^2$. The parenthesis is squared to facilitate the contrast of the correlation image, i.e., the power of the parenthesis acts as a modulating gain. Here, note that although the surface in-plane component and the surface normal component of Lamb modes in general are different in both phase and magnitude along the propagation axis, the frequency and phase velocity of a Lamb mode is the same for both components. For this example, an improved correlation image quality is obtained by the usage of two components instead of one component.

3.3 Radial offset domain transformation

By assuming cylindrical spreading of the wave field due to a point source, the processing scheme for a line array can be extended to include 2D arrays created by groups of sensors defined by a surface. Practically, this can be realized by transforming the recorded data to a radial offset domain. In the radial offset domain, the locations of the sensors are defined by a spatial radial coordinate r that measures the distance from the sensor to the source location (red cross in Fig. *2*(a) and (b)). Naturally, the radial coordinate r_m for a sensor m is given by

$$r_m = \sqrt{x_m^2 + y_m^2} \qquad \text{Eq. 10}$$

where x_m and y_m are the coordinates for the sensor m in the xy-plane. In other words, the radial offset domain represents a polar domain with a radial axis r directed outward from the center of the domain located at $x = y = 0$ (the location of the transient source from reciprocity).

In the radial offset domain, two acceleration responses are used: the surface normal response (z-direction) and the surface in-plane response (r-direction). Note that the z-axis in the radial offset domain is the same as the z-axis in the initial xyz-domain displayed in Fig. *2*. For this reason, no action is needed for the signals containing the surface normal response (z-direction); this response is only dependent on one physical channel of the accelerometer. However, to obtain the surface in-plane response (r-direction) in the radial offset domain, a simple transformation of the initially recorded data is required since this response is dependent on two physical channels (components) of the accelerometer. Accordingly, the surface in-plane acceleration response (r-direction) signal $\boldsymbol{s}_{m,in-plane}$ for a sensor m can be obtained by

$$\boldsymbol{s}_{m,in-plane} = (\boldsymbol{s}_{m,x} x_m + \boldsymbol{s}_{m,y} y_m)/r_m \qquad \text{Eq. 11}$$

where $\boldsymbol{s}_{m,x}$ and $\boldsymbol{s}_{m,y}$ are the signals containing the surface in-plane acceleration response in the x- and y-directions for the sensor m, respectively. That is, $\boldsymbol{s}_{m,in-plane}$ is obtained by projecting the acceleration response in the x- and y-direction onto the polar radial r-direction.

To proceed and further develop the study, the described transformation technique is applied to the collected dataset. An example of the output from this transformation is presented in Fig. 4, which shows the normalized surface in-plane (r-direction) acceleration response (Fig. 4(b)) and the normalized surface normal (z-direction) acceleration response (Fig. 4(c)) for the sensors marked with blue diamonds (Fig. 4(a)). For improved readability, the presented time-domain data are low-pass filtered to reduce the frequency content above 30 kHz. The selected sensors in Fig. 4(a) represent 14 sensors located at the radial offset distance $\mathrm{r} = 1.7 \pm 0.01$ m, i.e., at approximately the same radial offset distance r from the point source (red cross in Fig. 4(a)). In both Fig. 4(b) and (c), the signals from the 14 sensors show similar behavior. The consistency among the signals, showing the first arrival of the longitudinal wave around 0.9 ms and a surface wave around 1.2 ms, indicates that the plate under investigation is homogenous. Moreover, this consistency also implies a reliable and robust triggering in the time domain for each sensor. After around 1.7 ms, the signals are no longer consistent. This is related to the exposure of the sensors to different amounts of scattering and reflections; thus, we anticipate the reduced consistency as a function of time, as observed here.

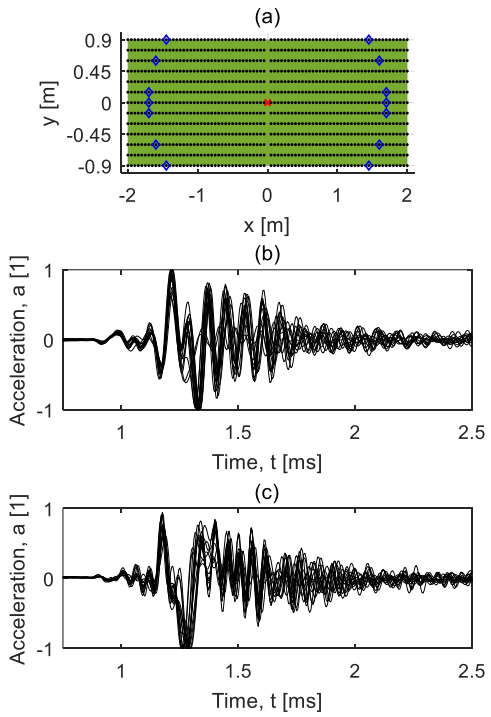

Fig. 4 (a) Measurement domain and sensors shown with blue diamonds, (b) corresponding time-domain low-pass filtered acceleration response for surface in-plane direction and (c) surface normal direction

3.4 2D array

By assuming a relatively constant material and plate thickness within a limited surface region, a 2D array defined by a group of sensors can be evaluated as a line array in the radial offset domain using a similar approach to that described in Section 3.2. This is done by adopting the transformation technique described in Section 3.3. One example of this evaluation is illustrated with the 2D array shown as blue markers in Fig. *5*(a). This 2D array is defined by the surface of a rectangle with a width

of 0.3 m and a slope of 25° (Fig. *5*(a)). The 2D array contains 85 sensors, and the data collected by these sensors are further studied in the radial offset domain. The surface in-plane acceleration response (r-direction) as function of time and space is shown in Fig. *5*(b). For improved readability, the presented time-domain data are low-pass filtered to reduce the frequency content above 30 kHz. In Fig. *5*(b), the longitudinal wave and the S1-ZGV Lamb mode can be observed; the data show major similarities with Fig. *3*(b).

The data are transformed to the frequency-phase velocity domain, and the results from this transformation are displayed in Fig. *5*(c). The processing technique required to create this correlation image is principally the same as that described in Section 3.2. However, since the data are analyzed in the radial offset domain, the coordinate variable x_m is replaced with the radial coordinate variable r_m. As a result, the test function for the discrete Fourier transform in the space domain takes a slightly different form, according to

$$\theta_{f-V}[r_m] = e^{2\pi i\, f_{test}/V_{test}\, r_m} \qquad \text{Eq. 12}$$

The corresponding test vector is created by

$$\boldsymbol{\theta}_{f-V} = \begin{bmatrix} \theta_{f-V}[r_1] \\ \theta_{f-V}[r_2] \\ \vdots \\ \theta_{f-V}[r_M] \end{bmatrix} \qquad \text{Eq. 13}$$

where r_m are the radial coordinates for the sensors. This means that the test vector $\boldsymbol{\theta}_{f-V}$ now represents a complex harmonic vector that is periodic along the radial axis r. Both the surface in-plane response (r-direction) and the surface normal response (z-direction) are calculated and used to create the correlation image in Fig. *5*(c) according to $(|s_{f-V,\mathrm{in-plane}}|+|s_{f-V,\mathrm{normal}}|)^2$. Major similarity between the correlation image for this 2D array (Fig. *5*(c)) and the correlation image for the line array (Fig. *3*(c)) is observed. This similarity ensures validity and strengthens the feasibility of using 2D arrays in evaluations performed in the radial offset domain. The similarity also verifies, to some extent, that the plate is homogenous within the measurement domain. This result is expected since a newly cast plate is studied; the test location is intentionally selected to ensure an environment with few uncertainties.

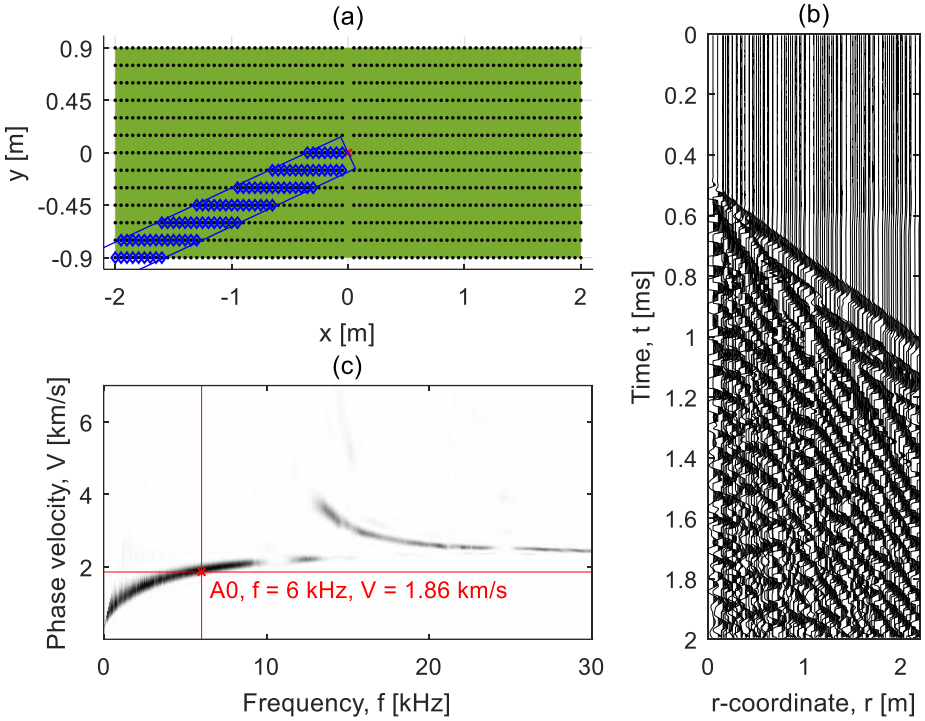

Fig. 5 (a) Measurement domain and rectangular 2D array shown with blue diamond markers, (b) time-domain low-pass filtered surface in-plane acceleration response, (c) frequency-phase velocity correlation image and estimated velocity for A0 Lamb mode at 6 kHz

3.5 Variation of phase velocity: polar angle and 2D imaging

The dispersive properties of Lamb modes in a plate are defined by the material properties and thickness. If a variation in the material or thickness is present in the lateral plane of the plate, then a variation in the dispersion is also present. The homogeneity of a plate can be assessed by measuring the phase velocity of Lamb modes at different locations on the plate. For a complete assessment, the analysis may be focused on the full frequency range of the dispersive wave field. However, this may be an elaborate task, at least for an initial assessment of a measurement object. It is therefore reasonable to select one or a few modes at a narrow range of frequencies for the initial analysis of homogeneity. As such example, in the following part of this study, we select the A0 Lamb mode at the frequency 6 kHz; see the marking with a red cross in Fig. *5*(c). This Lamb mode is selected since its mode shape is present through the entire thickness of the plate. The phase velocity of the mode is therefore dependent on both the material properties along the complete cross-sectional thickness as well as on the dimension of the thickness itself; i.e., the mode is not sensitive to potential local surface material inhomogeneities.

Using the test phase velocity that maximizes the correlation image amplitude at 6 kHz in Fig. *5*(c), the phase velocity for the A0 Lamb mode is estimated to be 1.86 km/s; see the marking with a red cross in Fig. *5*(c). The corresponding wavelength is therefore $\lambda = V/f \approx 0.3$ m. Thus, considering the nominal plate thickness of 0.12 m, this mode can be considered as a robust selection suitable for an initial assessment of the general homogeneity of the plate. The estimated phase velocity is representative of the surface region covered by the 2D array displayed with blue diamond markers in Fig. *5*(a). That is, the estimate represents a type of spatial average of the phase velocity for the mode within the surface region given by the 2D array; the 2D array can be interpreted as a spatial averaging operator dependent on the surface size and shape in relation to the wavelength of the mode.

Fig. 6(a) shows the estimated phase velocity for the A0 Lamb mode at 6 kHz as a function of the polar angle of the 2D array in steps of 5°. This result is obtained by a stepwise rotation of the 2D array in Fig. *5*(a) around the measurement and a corresponding estimation of the phase velocity at each step. Results show little variation in the estimated phase velocity; the minimum, mean, and maximum phase velocities are 1793 m/s, 1849 m/s, and 1911 m/s, respectively. That is, the variation is typically within $\pm 3\%$ of the mean phase velocity, and an almost consistent phase velocity for the A0 Lamb mode is observed. Thus, results from this initial assessment show that the plate is essentially homogenous within the measurement domain. This is expected since a newly cast plate is studied.

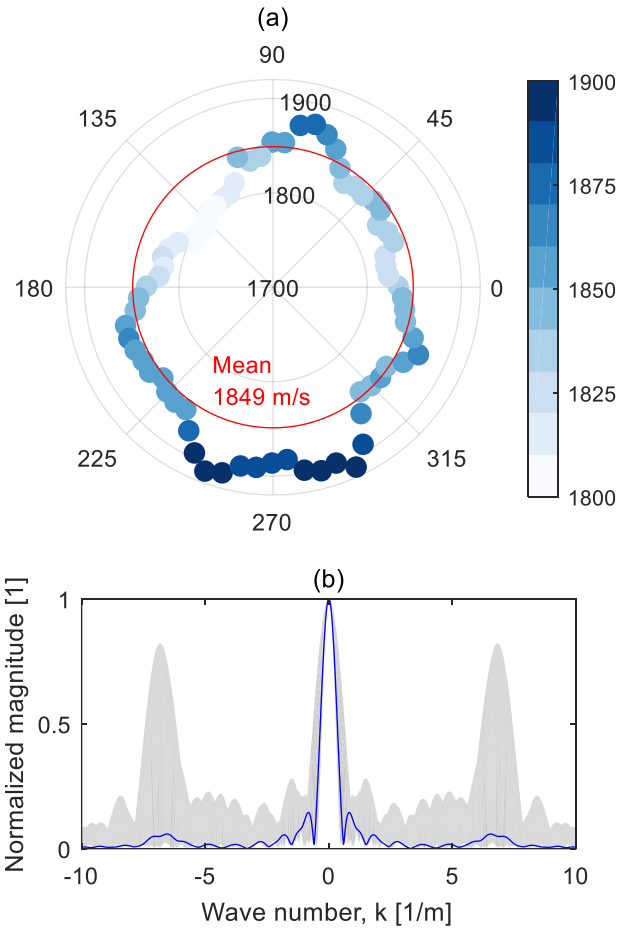

Fig. 6 (a) Estimated phase velocity for the A0 Lamb mode at 6 kHz as a function of polar angle for the rectangular 2D array; (b) envelope for normalized absolute values of the array window functions in frequency (wave number) domain shown as gray shading; blue line corresponds to rectangular 2D array in Fig. 5(a)

When performing a frequency analysis with discrete Fourier transforms, the topic of sampling is an important matter. In this example, where the phase velocity is estimated as a function of the angle of the 2D array, constant and uniform sampling is used in the time domain. However, this is not the case for sampling in the space domain, since each angle (step of 5°) is associated with one particular 2D array and set of sensors. This means that the number of sensors, as well as their interrelating locations in the radial offset (space) domain, will vary among the different 2D arrays (angles). For this reason, it is of interest to evaluate the influence from the characteristics of each 2D array (angle).

From a signal-processing point of view, a general array corresponds to a spatial window function that is used to sample the wave field [30]. The sampling in the radial offset (space) domain represents a

multiplication of the spatial array window function and the physical wave field. According to the convolution theorem, multiplication in the space domain corresponds to convolution in the frequency (wave number) domain. Thus, the measurement (sampling) corresponds to a convolution between the discrete Fourier transform of the array window function and the true wave field in the frequency domain. Owing to this, the resolution of the estimated phase velocity (wave number) is dependent on the discrete Fourier transform of the array window function. In this example, the array window is defined by a discrete rectangular function with unit value at the locations of the sensor positions and zero value elsewhere. This means that the spatial discrete Fourier transform of the array window function, at a test wave number $k_{test} = f_{test}/V_{test}$, is obtained by a summation of the complex components in the test vector $\boldsymbol{\theta}_{f-V}$ [26]. By repeating this calculation for a range of test wave numbers k_{test}, the spatial Fourier transform of the array window function is obtained.

For the 2D array shown with blue diamond markers in Fig. *5*(a), the absolute value of the spatial Fourier transform for the array window function is shown in Fig. *6*(b) with a blue solid line. The gray shading in Fig. *6*(b) represents the envelope corresponding to all 2D arrays that are used to create Fig. *6*(a). Note that the magnitude of the window functions are normalized in Fig. *6*(b). In the evaluation of the spatial Fourier transforms of window functions, two aspects are considered. The first aspect concerns the width of the main lobe at the wave number $k = 0$, which determines the resolution of the estimated frequency (wave number). A narrowing of this width increases the resolution and a broadening reduces the resolution. In Fig. *6*(b), the envelope exhibits some spread. From a manual inspection (not shown here) of the data analysis of the 2D arrays with the greatest main lobe width, we can see that reliable estimations of the phase velocity are obtained even for these 2D arrays. In particular, we verify that we can obtain correlation images (as in Fig. *5*(c)) with sufficient resolution and similarity compared with those created from the other 2D arrays with a narrower main lobe width. The second aspect concerns the locations of the highest side lobes, at $k = \pm 7$ in Fig. *6*(b), which provide information about potential aliasing. For the mean phase velocity of $V = 1849\ m/s$ at the frequency $f = 6\ kHz$, the corresponding wave number is $k = f/V = 3.2\ m^{-1}$. This means that the side lobes appear at $k = 3.2 \pm 7\ m^{-1}$. For the phase velocity, this corresponds to approximately $V = -1600\ m/s$ and $V = 600\ m/s$. Consequently, since the A0 Lamb mode is a single dominating mode at the investigation frequency (6 kHz), the effect from aliasing from these side lobes does not represent an issue in this example. To summarize, by considering these two aspects, we verify that the result presented in Fig. *6*(a) is based on a reliable sampling in space. This type of verification is central in all types of frequency analyses, but is especially important for the cases, as here, where nonuniform sampling is used.

The study of the variation in phase velocity in Fig. *6*(a) is made by rotating a 2D array with a rectangular shape. However, the rectangular shape represents only one among many possible shapes. For instance, a possible alternative is a 2D array defined by a circular surface. Fig. *7*(a) shows an example of a 2D array defined by a circle with radius 0.45 m, and this type of 2D array is further explored in the following. Compared with the rectangular 2D array in Fig. *5*(a), with one end fixed at the source location, Fig. *7*(a) shows that the position of a 2D array with a circular shape can be changed more freely within the measurement domain given by the green rectangle. Here, we sweep the circular 2D array within a rectangular grid space defined by 40 points along the x-axis and 20 points along the y-axis. Following the same principle as previously described, an estimation of the phase velocity for the A0 Lamb mode at 6 kHz is made at each grid point. Accordingly, this provides an estimate of the phase velocity over a 2D grid surface. The result from this evaluation is shown in Fig. *7*(c) as a phase velocity image with color corresponding to the estimated phase velocity. Note that the color of each pixel is representative of the estimated phase velocity within the complete surface covered by the corresponding 2D array. In other words, the pixel color does not represent a

pointwise phase velocity estimation, since the 2D array has an averaging (smoothing) influence. The minimum, mean, and maximum phase velocities are 1771 m/s, 1840 m/s, and 1910 m/s, respectively. Thus, also for this evaluation, an almost consistent phase velocity for the A0 Lamb mode is observed in the phase velocity image. Similar to the result in Fig. *6*(a), the phase velocity image in Fig. *7*(c) further confirms that a condition of material homogeneity and plate thickness is present in the measurement domain. Again, this result is expected since a newly cast and ideally homogenous plate is studied.

Similar to the evaluation based on a rotating 2D array, this evaluation is also associated with nonuniform sampling in the space domain. For the circular 2D array shown in Fig. *7*(a), the spatial Fourier transform of the corresponding array window function is shown with a solid blue line in Fig. *7*(b). The gray shading corresponds to the envelope of the spatial Fourier transforms of all array window functions. As previously, we verify the robustness of the estimation by monitoring the correlation image quality for the 2D arrays with the greatest main lobe. Again, since the A0 Lamb mode is a single dominating mode, the effect from aliasing due to side lobes does not present an issue in this case. Yet, for detailed and further investigations of an object, the implementation of a sampling criterion that discards estimates obtained from arrays with insufficient spectral resolution and performance may provide an approach for handling the sampling and ensuring consistent reliability of the results.

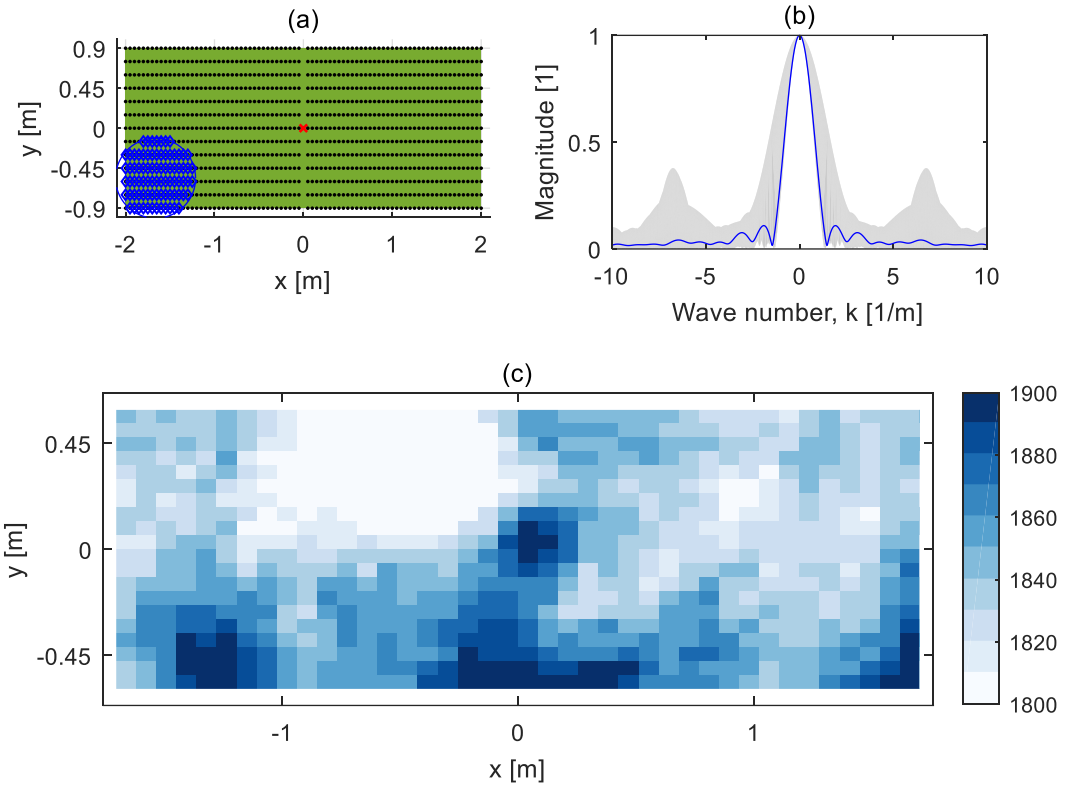

Fig. 7 (a) Measurement domain and circular 2D array shown with blue diamond markers; (b) envelope for normalized absolute values of the array window functions in frequency (wave number) domain shown as gray shading; blue line corresponds to circular 2D array in the top-left subfigure; (c) estimated phase velocity for the A0 Lamb mode at 6 kHz as function of 2D array center coordinate

4. Concluding remarks

With a full wave field dataset as the basis, we demonstrate and describe the implementation of a processing technique that enables a Lamb wave analysis in the frequency-phase velocity domain. Through the transformation of data into the radial offset domain, the initial technique is extended to include 2D arrays defined by 2D surfaces such as rectangles or circles. An analysis of the phase velocity as a function of polar angle is performed for 2D arrays with a rectangular shape, and a 2D phase velocity imaging analysis is performed for the 2D array with a circular shape. Naturally, other 2D array layouts are possible although they are not discussed here.

Results from the analysis of the phase velocity variation for the A0 Lamb mode at 6 kHz show a consistent phase velocity with little variation and a mean value around 1850 m/s. This means that the investigated plate is, as expected, essentially homogenous with little variation in the material properties and thickness within the measurement domain. Thus, this type of analysis is an example of an initial assessment of material condition and plate thickness for an unknown testing object. For most 2D arrays in this study, we used nonuniform sampling in the space domain. It is shown that a spectral estimation can also be performed under this sampling condition. Nevertheless, to ensure reliable results, the effect from the sampling condition should be evaluated.

The presented technique is demonstrated on one specific plate. Naturally, for further developments, it is important to investigate the application on other test objects as well as to understand its sensitivity to defects and anomalies. It is reasonable that the literature on guided wave applications in other fields may be useful for this task. Concerning the practicality of the measurements, it is expected that, with modern developments in fields such as wireless protocols, positioning systems, digital image processing, and augmented reality, the effort of collecting a full wave field dataset over a measurement domain, as in this study, can be minimized.

To summarize, from a general viewpoint we are able to show that a Lamb wave phase velocity imaging analysis of concrete plates can be performed with essentially the same simple equipment as that used for the IE method [7]. This highlights the very general characteristic of the utilized full wave field response, that a substantial number of evaluation methodologies are likely possible. Compared to ultrasonic transducers, transient impact sources are not limited to a narrow band of operating frequency; on the contrary, energy over a wide range of frequencies is generated and fed into a full wave field response. For this reason, techniques based on transient impact sources (full wave field) are important in cases where scattering and attenuation issues limit the use of ultrasonic techniques. In view of the need to inspect infrastructure constructions of large dimensions with potentially heavily reinforcement and coarse aggregates, we believe full wave field approaches, such as the one presented, represent a valuable and qualified complement to ultrasonic techniques. Here, it is emphasized that full wave field approaches operating in the frequency range below ultrasonic techniques, say 10–20 kHz, do not provide a substitute for ultrasonic techniques; our opinion is that optimal nondestructive evaluation is obtained by combining information from several techniques. That said, we hope that future full wave field approaches are considered equally qualified as ultrasonic techniques, and that this study provides a step toward a more developed and unified evaluation approach for concrete structures that utilize as many techniques (carriers of information) as reasonably possible.

Acknowledgements

The Development Fund of the Swedish Construction Industry (SBUF, No. 13104) and The Swedish Radiation Safety Authority (SSM, No. SSM2017-956) are acknowledged for financial support of the

study. The staff at PEAB in Trollhättan are acknowledged for generously providing access to the construction (test) site.

References

1. Bungey JH, Millard SG, Grantham MG (2006) Testing of Concrete in Structures, 4th ed. Taylor & Francis, Abingdon

2. Pla-Rucki GF, Eberhard MO (1995) Imaging of Reinforced Concrete: State-of-the-Art Review. J Infrastruct Syst 1:134–141. doi: 10.1061/(ASCE)1076-0342(1995)1:2(134)

3. Schickert M, Krause M, Müller W (2003) Ultrasonic Imaging of Concrete Elements Using Reconstruction by Synthetic Aperture Focusing Technique. J Mater Civ Eng 15:235–246. doi: 10.1061/(ASCE)0899-1561(2003)15:3(235)

4. Wiggenhauser H, Samokrutov A, Mayer K, et al (2016) Large Aperture Ultrasonic System for Testing Thick Concrete Structures. J Infrastruct Syst 23:B4016004. doi: 10.1061/(ASCE)IS.1943-555X.0000314

5. Almansouri H, Johnson C, Clayton D, et al (2017) Progress implementing a model-based iterative reconstruction algorithm for ultrasound imaging of thick concrete. AIP Conf Proc. doi: 10.1063/1.4974557

6. Schickert M, Krause M (2010) Ultrasonic techniques for evaluation of reinforced concrete structures. In: Non-Destructive Eval. Reinf. Concr. Struct. Elsevier, pp 490–530

7. Sansalone MJ, Streett WB (1997) Impact-echo: Non-destructive Evaluation of Concrete and Masonry. Bullbrier Press

8. Schubert F, Köhler B (2008) Ten Lectures on Impact-Echo. J Nondestruct Eval 27:5–21. doi: 10.1007/s10921-008-0036-2

9. Zhu J, Popovics JS (2007) Imaging Concrete Structures Using Air-Coupled Impact-Echo. J Eng Mech 133:628–640. doi: 10.1061/(ASCE)0733-9399(2007)133:6(628)

10. Dai X, Zhu J, Haberman MR (2013) A focused electric spark source for non-contact stress wave excitation in solids. J Acoust Soc Am 134:EL513-EL519. doi: 10.1121/1.4826913

11. Gibson A, Popovics JS (2005) Lamb Wave Basis for Impact-Echo Method Analysis. J Eng Mech 131:438–443. doi: 10.1061/(ASCE)0733-9399(2005)131:4(438)

12. Prada C, Clorennec D, Royer D (2008) Local vibration of an elastic plate and zero-group velocity Lamb modes. J Acoust Soc Am 124:203–212. doi: 10.1121/1.2918543

13. Kim DS, Seo WS, Lee KM (2006) IE-SASW method for nondestructive evaluation of concrete structure. NDT E Int 39:143–154. doi: 10.1016/j.ndteint.2005.06.009

14. Medina R, Bayón A (2010) Elastic constants of a plate from impact-echo resonance and Rayleigh wave velocity. J Sound Vib 329:2114–2126. doi: 10.1016/j.jsv.2009.12.026

15. Ryden N, Park CB (2006) A combined multichannel impact echo and surface wave analysis scheme for non-destructive thickness and stiffness evaluation of concrete slabs. AS NT, 2006 NDE Conf Civ Eng 247–253.

16. Barnes CL, Trottier J-F (2009) Hybrid analysis of surface wavefield data from Portland cement and asphalt concrete plates. NDT E Int 42:106–112. doi: 10.1016/j.ndteint.2008.10.003

17. Baggens O, Ryden N (2015) Systematic errors in Impact-Echo thickness estimation due to near

field effects. NDT E Int 69:16–27. doi: 10.1016/j.ndteint.2014.09.003

18. Medina R, Garrido M (2007) Improving impact-echo method by using cross-spectral density. J Sound Vib 304:769–778. doi: 10.1016/j.jsv.2007.03.019

19. Ryden N (2016) Enhanced impact echo frequency peak by time domain summation of signals with different source receiver spacing. Smart Struct Syst 17:59–72. doi: 10.12989/sss.2016.17.1.059

20. Baggens O, Ryden N (2015) Poisson's ratio from polarization of acoustic zero-group velocity Lamb mode. J Acoust Soc Am 138:EL88-EL92. doi: 10.1121/1.4923015

21. Boiero D, Bergamo P, Rege RB, Socco LV (2012) Estimating surface-wave dispersion curves from 3D seismic acquisition schemes : Part 1 — 1D models. Geophysics 76:G85–G93. doi: 10.1190/geo2011-0124.1

22. Harley JB, Moura JMF (2013) Sparse recovery of the multimodal and dispersive characteristics of Lamb waves. J Acoust Soc Am 133:2732–2745. doi: 10.1121/1.4799805

23. Park CB, Miller RD, Xia J (1999) Multichannel analysis of surface waves. Geophysics 64:800–808. doi: 10.1190/1.1444590

24. Gao W, Glorieux C, Thoen J (2003) Laser ultrasonic study of Lamb waves: Determination of the thickness and velocities of a thin plate. Int J Eng Sci 41:219–228. doi: 10.1016/S0020-7225(02)00150-7

25. Alleyne D, Cawley P (1991) A two-dimensional Fourier transform method for the measurement of propagating multimode signals. J Acoust Soc Am 89:1159–1168. doi: 10.1121/1.400530

26. Zywicki D, Rix G (2005) Mitigation of near-field effects for seismic surface wave velocity estimation with cylindrical beamformers. J Geotech Geoenvironmental … 970–977. doi: 10.1061/(ASCE)1090-0241(2005)131:8(970)

27. McMechan GA, Yedlin MJ (1981) Analysis of dispersive waves by wave field transformation. Geophysics 46:869–874. doi: 10.1190/1.1441225

28. Park CB, Miller RD, Xia J, Survey KG (1998) Imaging dispersion curves of surface waves on multichannel record. In: 68th Ann. Internat. Mtg., Soc. Expl. Geophys. Expand. Abstr. pp 1377–1380

29. Ambrozinski L, Piwakowski B, Stepinski T, Uhl T (2014) Evaluation of dispersion characteristics of multimodal guided waves using slant stack transform. NDT E Int 68:88–97. doi: 10.1016/j.ndteint.2014.08.006

30. Brandt A (2011) Noise and Vibration Analysis. doi: 10.1002/9780470978160

Appendix D

Paper IV

O. Tofeldt and N. Ryden. 2017.
Zero-group velocity modes in plates with continuous material variation through the thickness. The Journal of the Acoustical Society of America, 141(5):3302-3311.
DOI: 10.1121/1.4983296

Zero-group velocity modes in plates with continuous material variation through the thickness

Oskar Tofeldt[a] and Nils Ryden
Division of Engineering Geology, Lund University, P.O. Box 118, SE-22100, Lund, Sweden

(Received 29 December 2016; revised 27 April 2017; accepted 28 April 2017; published online 17 May 2017)

Lamb modes with zero group velocity at nonzero wave numbers correspond to local and stationary resonances in isotropic plates. Lamb modes can be utilized for nondestructive evaluation of the elastic properties and thickness. One example of an application is the testing of plate-like concrete structures. In this example, continuous variation in the material velocity through the thickness may occur. This is usually not accounted for in analyses, and with this as starting point, two inhomogeneous and nonsymmetric cases with continuous material variations are investigated using a semi-analytical finite element technique and a simulated measurement application. In a numerical study limited to the lowest zero-group velocity mode, results show that these modes for the inhomogeneous cases are generated with similar behavior and the same detectability as in the case of an isotropic plate. However, a complex relationship between mode frequency and material velocity exists for the inhomogeneous cases. This hinders the evaluation and interpretation of representative estimations such as those for a cross-sectional mean value of the plate properties. This may lead to errors or uncertainties in practical applications. © *2017 Acoustical Society of America*.
[http://dx.doi.org/10.1121/1.4983296]

[JFL] Pages: 3302–3311

I. INTRODUCTION

An interesting and fascinating type of Lamb mode is the so-called zero-group velocity (ZGV) mode.[1,2] These Lamb modes possess the extraordinary property of a vanishing group velocity combined with a nonzero wave number. More specifically, the vanishing group velocity is due to the interference of two modes, defined at the same frequency, that have the same mode shape propagating with equal absolute phase velocities (wave numbers) but with opposite signs (directions). In this case, a stationary mode is obtained that materializes as a local ringing resonance of the plate structure with a sharp and distinct frequency peak in the response spectrum. Since the characteristics of ZGV Lamb modes are defined by the elastic properties and thickness of the plate,[3] this type of resonance may be utilized for nondestructive evaluation. Because of its stationary and nonpropagating nature, a local estimation of the elastic properties and thickness is obtained.[1,4] This feature is particularly useful in situations where constant material or thickness is not ensured in the lateral plane of the plate and in cases where a free and accessible surface for analyzing propagating waves is limited.

In the literature, Tolstoy and Usdin[5] predicted in 1957 the existence of a sharp ringing resonance related to a vanishing group velocity in an elastic plate. More recently, the topic has received new attention in studies that demonstrate both generation and detection of such sharp ringing resonances[4,6] and explicitly link this phenomena to ZGV Lamb modes. The topic of ZGV Lamb modes is currently active within ongoing nondestructive evaluation studies. Topics include isotropic plates,[1,7,8] anisotropic plates,[9] hollow cylinders,[10,11] the interfacial stiffness of layered media,[12,13] thin-layer measurements,[14] and glass materials.[15] Studies also examine air-coupled measurements,[4,16–18] wave focusing,[19,20] and enhanced ZGV Lamb mode generation in laser ultrasonic applications.[21–23]

Clearly, the results presented in the literature demonstrate the potential of using ZGV Lamb modes, and several evaluation techniques and applications have evolved. One example, which is the focus of the present work, is the testing of plate-like concrete structures. Early studies reported on the usage of a longitudinal thickness resonance,[24] which is linked to the first symmetric ZGV Lamb mode[25] and subsequently combined with surface wave measurements.[26] More recently, this work has been extended with techniques that use the ZGV Lamb mode shape to estimate the temporal frequency[27–29] and Poisson's ratio.[7] Indeed, this example of progression confirms and strengthens the importance of a thorough understanding of the behavior of ZGV Lamb modes for improved further development.

Although the literature concerning ZGV Lamb modes is rather extensive, to the authors' best knowledge, only a few studies consider the topic of continuously varying material through the plate thickness.[30] In contrast to structures formed by discrete layers and well-defined interfaces such as laminates, some plate-like concrete structures may have continuously varying material properties through the plate thickness.[31–37] Such continuous material variations, resulting in varying acoustic bulk wave velocities, may originate from the uneven settlement of aggregates during casting, uneven moisture distribution, material degradation or corrosion of internal steel reinforcement, or other mechanisms.[38] Even so, potential variations in the material properties are

[a]Electronic mail: oskar.tofeldt@tg.lth.se

 0001-4966/2017/141(5)/3302/10/$30.00

generally not considered in measurements of plate-like concrete structures with ZGV Lamb modes;[25,39] on the contrary, isotropy based on constant material properties through the plate thickness is usually implicitly assumed. To better understand the limitations and robustness of this type of application and to support further development, there is a need for improved knowledge of ZGV Lamb modes in plates with continuous material variations through the thickness. Improved understanding also contributes to the overall aim of increased knowledge within the general field of ZGV Lamb modes.

This study investigates the behavior of ZGV modes in two synthetic cases defined by two plates with inhomogeneous and nonsymmetric continuous variation of the acoustic bulk wave velocities. Results are also compared with a corresponding isotropic case. Since only a few prior studies used higher ZGV modes in the testing of plate-like concrete structures,[40,41] the present work is limited to a study of the lowest ZGV mode. For isotropic plates with Poisson's ratio $\nu < 0.45$, the lowest ZGV mode is linked to the first symmetric (S1) Lamb mode,[1] typically referred to as the S1-ZGV Lamb mode. The study is organized in sections as follows: Sec. II defines the material variation cases, Sec. III describes the investigation into the cases using a semi-analytical finite element (SAFE) technique, and Sec. IV further explores the cases in a simulated nondestructive testing application. Although the study originates from a perspective of thick concrete structures, the results hold for other inhomogeneous cases as well under the condition of guided wave propagation in plate-like structures through the general assumption of linear elastic wave propagation.

II. MATERIAL VARIATION CASES

This study investigates two inhomogeneous cases, referred to as case 1 and case 2, defined by two infinite plates with continuous material variation throughout the thickness. These two cases (plates) are also compared with a homogeneous, isotropic reference case defined by an isotropic and infinite plate with constant material properties throughout its thickness. Although the unbounded (infinite) domain of the cases represent a theoretical and idealized condition, results for the lowest ZGV Lamb mode derived under this assumption can be generalized and extended to real plates of finite dimensions at distances greater than one thickness from the plate-edge.[42] From the perspective of thick plate-like concrete structures that may have continuous material variations, cases 1 and 2 are characterized by a continuous inclusion of material with a high and low acoustic wave velocity, respectively. A more detailed description of both cases and their relation to the isotropic reference case is provided below.

Both cases are modifications of the isotropic reference case, which is represented by a linear elastic isotropic plate with thickness axis parallel to the vertical z axis, infinite lateral dimensions in the horizontal xy plane, a midplane coincident with the horizontal xy plane ($z = 0$), and a thickness $t = 1$ m. The homogeneous material in the isotropic reference case is defined by a longitudinal wave velocity $V_L = 4303$ m/s, a transversal wave velocity $V_T = 2635$ m/s (Poisson's ratio $\nu = 0.2$), and density $\rho = 2400\,\mathrm{kg/m^3}$. Starting from this isotropic reference case as a common basis, case 1 and case 2 are generated by adjusting the values of the acoustic bulk wave velocities ($V_L = 4303$ m/s and $V_T = 2635$ m/s) according to a scaling function with spatially varying amplitude along the plate thickness coordinate z.

In total, two scaling functions are used in the study with one function assigned to each case. The scaling functions for case 1 and case 2 are shown in Figs. 1(a) and 1(b), respectively. The two functions are defined similarly, with one term given by a single cycle of a sinusoidal function

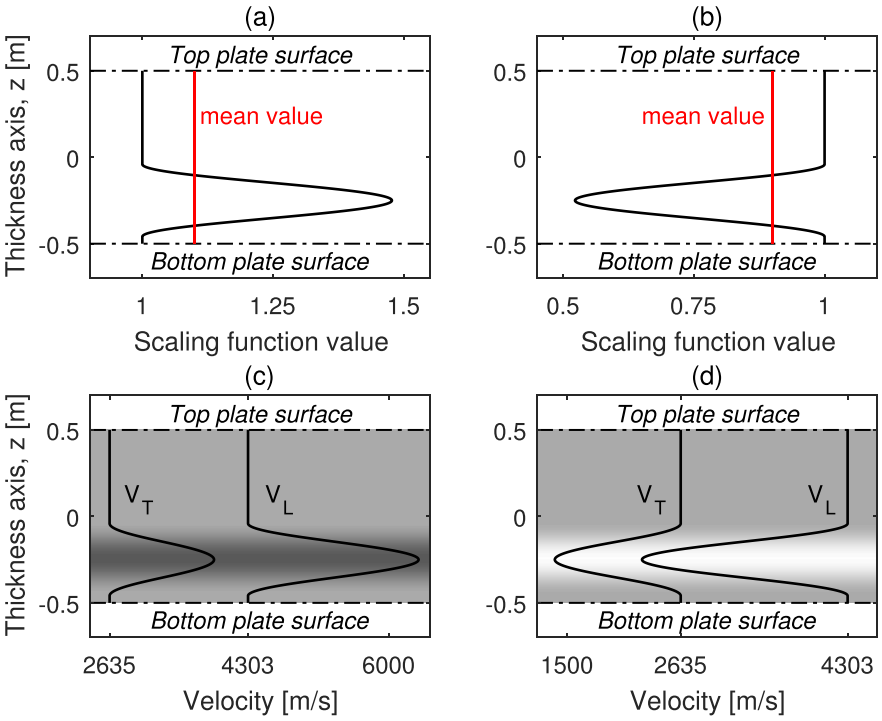

FIG. 1. (Color online) Scaling function for (a) case 1 and (b) case 2. Variation of acoustic bulk wave velocities for (c) case 1 and (d) case 2.

(crest to crest) as well as a second constant term of unity. For both cases, the wave cycle has the same frequency and spatial location but it differs in magnitude and sign. The corresponding variations in the longitudinal and transversal wave velocities as function of the thickness coordinate for cases 1 and 2 are shown in Figs. 1(c) and 1(d), respectively. To highlight the continuous variation of the material, the darkness of the background colors of Figs. 1(c) and 1(d) increase with increasing velocity. It is emphasized that, since the longitudinal and transversal wave velocities vary with the same shape and relative magnitude, a uniform value of the Poisson's ratio ($\nu = 0.2$) is maintained throughout the entire thickness of the plate in both cases. It can also be noted that, for both cases, the material at the top and bottom plate surfaces is unaffected by the scaling function and accordingly remains the same.

Figure 1 shows that cases 1 and 2 represent an increase and decrease in the magnitude of the acoustic bulk wave velocities, respectively. For both cases, this shift appears in a region below the midplane of the plate ($z < 0$) and is symmetric around a peak value located at $z = -0.25$. At this peak value, cases 1 and 2 exhibit an increase and decrease, respectively, of the acoustic bulk wave velocities with a maximum absolute relative change of approximately 50%. More precisely, the specific amplitudes of the sinusoidal wave cycles for both cases are adjusted to result in a relative shift of 10% of the spatial mean acoustic bulk wave velocities throughout the plate thickness, compared to the initial values defined by the isotropic reference case ($V_L = 4303$ m/s and $V_T = 2635$ m/s). This relative shift is highlighted in Figs. 1(a) and 1(b) by the cross-sectional mean value of the scaling functions (0.9 and 1.1) for case 1 and case 2, respectively.

Considering the above detailed descriptions of the two cases, it should be noted that these two cases represent just one selection from the countless candidate material variation cases. In fact, an infinite number of material variation cases exist. With the necessity to limit these cases, the present work focuses on two cases that enable a study of ZGV modes in plates with a continuous inclusion of material with either high or low acoustic bulk wave velocities. Moreover, the inclusion is located in a position that creates a nonsymmetric inhomogeneous material condition with respect to the midplane of the plate. Although the motive for this selection develops from the perspective of thick concrete structures, it should be noted that the cases are not representative of a particular concrete structure or of a universal material variation case. However, given the high magnitude of variation in the acoustic bulk wave velocities, it is anticipated that most concrete structures fall within the boundary limits formed by the case definitions. As a result, the observed qualitative and quantitative results can be considered valuable and relevant for plate-like concrete structures in general as well as for other ZGV Lamb mode applications in view of the general validity of linear elastic wave propagation.

III. SEMI-ANALYTICAL FINITE ELEMENT ANALYSIS

A. Method

Under the assumption of a linear elastic, isotropic, and infinite plate located in the horizontal xy plane, the vertically (z axis) polarized wave field is defined by the Rayleigh-Lamb equation;[3,43,44] the corresponding solutions in terms of wave modes are usually referred to as Lamb modes. Although the Rayleigh-Lamb equation appears in a deceivingly simple and compact form, the task of obtaining a full wave field solution usually requires extensive processing. As anticipated, the case of layered structures is more complex than the case of isotropic plates. For most layered structures, closed form equations like the Rayleigh-Lamb equation do not exist. Instead, global matrix formulations based on discrete isotropic layers joined by common interfaces may be adopted.[45] Typically, these approaches, often referred to as matrix methods, are used for systems described by a handful of layers.

In the study of mechanical waves in plates with continuous material variations, such as with cases 1 and 2, conventional finite element (FE) simulations can be used to predict the dynamic response behavior. However, data from such simulations simultaneously include all existing wave modes within the investigated frequency range; thus, extensive processing is usually required to resolve the dispersive relations within the wave field solution. An alternative approach is to adopt a SAFE technique,[46] which is a compromise between a fully numerical method and a strictly analytical method. Briefly, the SAFE technique assumes harmonic wave mode propagation along the path of a uniform waveguide defined by an arbitrary, but constant, cross section in the lateral direction. A reduced system is obtained in which only the waveguide cross section must be discretized by finite elements. The wave field solution of the system can then be determined by solving the associated eigenvalue problem of temporal and spatial frequency using standard numerical routines. On that account, the SAFE technique is one possible candidate approach for obtaining the wave field solution of cases 1 and 2; therefore, it is adopted in the present work.

From the implementation of a SAFE model in a commercial FE code,[47] as described by Predoi *et al.*,[48] the wave field solutions for cases 1 and 2 are determined and further analyzed. These wave field solutions, strictly speaking, are determined from a model composed of a finite number of discrete material layers (elements). However, by including a sufficient number of material layers (elements) and with a careful monitoring of the model solution convergence, the obtained wave field solutions approach the continuous nature of cases 1 and 2. The wave field solution for the isotropic reference case is also determined. For all three cases (1, 2, and the isotropic reference), no material damping is taken into account.

B. Results and analysis

The resulting wave number-frequency dispersion curves for cases 1 and 2 obtained from the SAFE model are shown in Figs. 2(a) and 2(b), respectively. The dispersion curves in Fig. 2 show the four lowest propagating modes (real wave number k) polarized in the plane defined by the thickness axis (z) and the lateral propagation axis; no shear horizontal modes are displayed. These four modes are denoted M1, M2, M3, and M4 for both cases (see Fig. 2). The dispersion

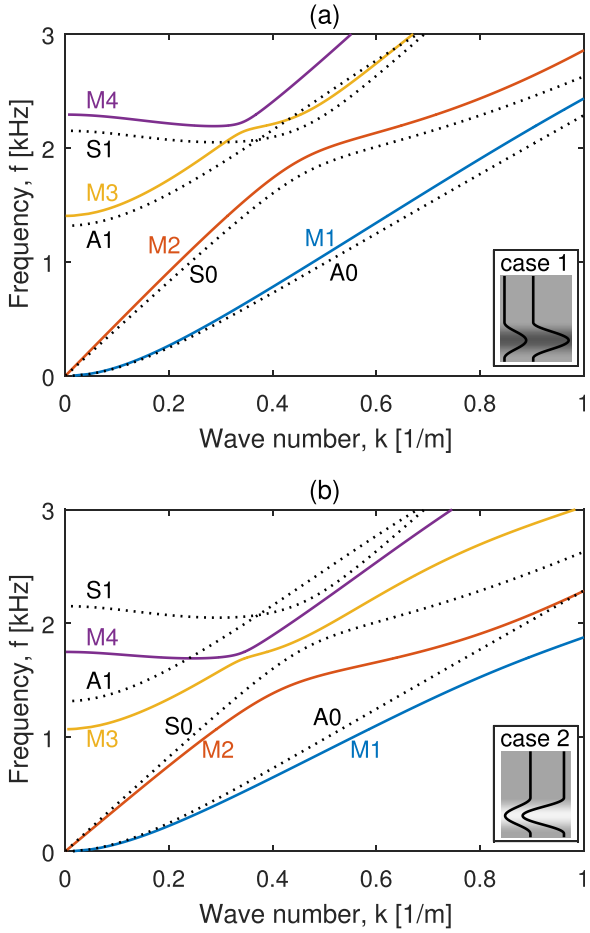

FIG. 2. (Color online) Wave number frequency solution for (a) case 1 and (b) case 2. Dotted lines show the isotropic reference case.

curves for the four lowest Lamb modes for the isotropic reference plate, A0, S0, A1, and S1, are displayed for comparison (dotted lines). For both cases, Fig. 2 shows that the overall pattern exhibited by the M1–M4 modes is similar to the pattern exhibited by the A0, S0, A1, and S1 Lamb modes for the isotropic reference plate. Moreover, it can be observed that, in general, the M1–M4 modes for case 1 [Fig. 2(a)] display a higher temporal frequency f at a given wave number k compared to the corresponding Lamb modes for the isotropic reference case at the same wave number k. This increase in frequency is equivalent to an increase in phase velocity $V_{\mathrm{ph}} = f/k$ and is due to the increase in the mean acoustic bulk wave velocities as defined by the scaling function associated with the case. As shown in Fig. 2(b), the opposite situation, with decreased frequency and phase velocity due to a decrease in the mean acoustic bulk wave velocities, holds for case 2.

Although both case 1 and case 2 exhibit similarities with the isotropic reference case, one difference between cases 1 and 2 and the isotropic reference case is that the M3 and M4 modes do not cross each other whereas the A1 and S1 Lamb modes do cross.[49,50] This important difference occurs because the wave field solution of an isotropic plate is divided into two families consisting of symmetric and antisymmetric modes with respect to the midplane of the plate. These two types of mode families are uncoupled through two separate governing equations.[3] However, for both case 1 and case 2, no such symmetry plane exists; i.e., no strict separation into symmetric or antisymmetric modes can be made and, therefore, crossings between the modes Mn within cases 1 and 2 are not allowed due to mode repulsion.[51] This lack of separation into symmetric or antisymmetric modes provides the motivation for the naming convention of the modes in cases 1 and 2 (M1, M2, …, Mn); i.e., no strict classification according to symmetry is made.

To facilitate the study of the first ZGV mode, an expanded view within a narrower range of wave numbers and frequencies is created (Fig. 3). Figure 3 shows the M4 mode wave number-frequency dispersion curves for cases 1 and 2 as well as the corresponding S1 Lamb mode curve for the isotropic reference plate. For both case 1 and case 2, it can be observed that the M4 dispersion curves, similar to the S1 dispersion curve, exhibit minimum points at a nonzero wave number. These minimum points, marked with asterisks in Fig. 3, represent modes at which the group velocity vanishes $V_g = df/dk = 0$; i.e., they are ZGV modes. For this reason, they are referred to as M4-ZGV and S1-ZGV (Fig. 3).

The frequencies f of the M4-ZGV mode for case 1 and case 2 are 2192 and 1694 Hz, respectively. Comparing with the frequency $f = 2051$ Hz for the S1-ZGV Lamb mode for the isotropic reference case, two observations are made. First, the shift in frequency is not linearly proportional to the change in the cross-sectional mean value of the acoustic bulk wave velocities ($+-10\%$). Second, the frequency f increases by 7% and decreases by 17% for case 1 and case 2, respectively, which indicates that the magnitude of the relative shift differs between the cases.

Regarding the first observation, this result is different for an isotropic plate where a relative shift in the acoustic bulk wave velocities is reflected as the same relative shift in frequency under the condition of a constant Poisson's ratio. Because of this, the explanation and description of the S1-ZGV Lamb mode frequency for isotropic plates is occasionally simplified to the empirical equation

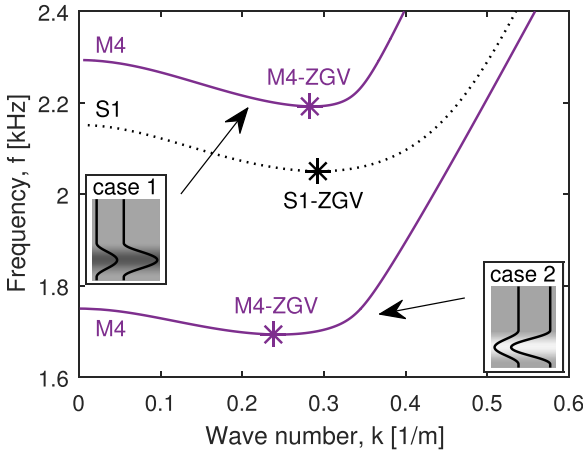

FIG. 3. (Color online) Expanded view of wave number frequency solution for the M4 mode (both case 1 and case 2) and S1 Lamb mode (isotropic reference case, dotted line). ZGV points marked with asterisks.

$$f = \frac{\beta V_L}{2h}, \tag{1}$$

where β is a correctional factor only dependent on the Poisson's ratio[25] and $V_L/(2h)$ represents the frequency of a cutoff mode created by a reverberating longitudinal wave. In more detail, Eq. (1) may be ascribed to the simplified and empirical interpretation[24] of the S1-ZGV Lamb mode as a reverberating longitudinal wave with a frequency shifted by the factor β. Although Eq. (1) produces the correct value of the S1-ZGV Lamb mode frequency, note that this interpretation is rather deceptive since Lamb waves, except at the mode cutoff, by definition are always created from the interference of both longitudinal and transversal waves. This explains the need for the correctional β factor, which in any event requires that the original Lamb wave problem is solved. Moreover, for plates with a Poisson's ratio $\nu > 1/3$, the cutoff S1 Lamb mode is created by a transversal wave as opposed to a longitudinal wave. In view of that, the meaning of Eq. (1) becomes somewhat ambiguous.

Regarding the second observation, a simplified and partial explanation for the difference in the relative shift of frequency (7% vs 17%) may be determined from the time of flight required for a high-frequency pulse with finite duration in time and space to travel between the top and bottom plate surface.[24] By comparing this time of flight for cases 1 and 2 with the corresponding value for the isotropic reference case, it can be shown that case 1 exhibits less relative change than case 2. Although this agrees with the result of the relative shift of the M4-ZGV frequency, note that this simplified analysis does not provide a consistent quantitative estimate of the frequency shift of the M4-ZGV mode compared with the S1-ZGV Lamb mode.

Certainly, due to the inhomogeneous variation of the acoustic bulk wave velocities in cases 1 and 2, no simple empirical expression like Eq. (1) exists; for both case 1 and case 2, there is a complex relation between mode frequency and acoustic material velocity. Indirect consequences of this additional complexity compared to the isotropic reference case may appear in nondestructive evaluations of the plate properties. For instance, if an isotropic Lamb wave model is assumed under the actual condition of case 1 or 2, then the estimated acoustic material velocity or plate thickness[39] from the M4-ZGV mode will be difficult to interpret since it cannot be directly translated to a representative mean value or other similar established quantitative measure. A similar argument holds for the shift in wave number or wavelength for the M4-ZGV mode.

Figure 4 shows the displacement mode shapes of the M4-ZGV mode (asterisks in Fig. 3) for case 1 and case 2 as a function of the plate thickness coordinate z. The profiles of the vertical and horizontal displacements are shown in Figs. 4(a) and 4(b), respectively. The corresponding displacement profiles of the S1-ZGV Lamb mode for the isotropic reference case are also shown for comparison (black dots). The amplitude of the profiles is normalized to produce the same maximum magnitude for all profiles. For both case 1 and case 2, Fig. 4 shows slightly distorted mode shapes—in contrast to the isotropic reference case—as there

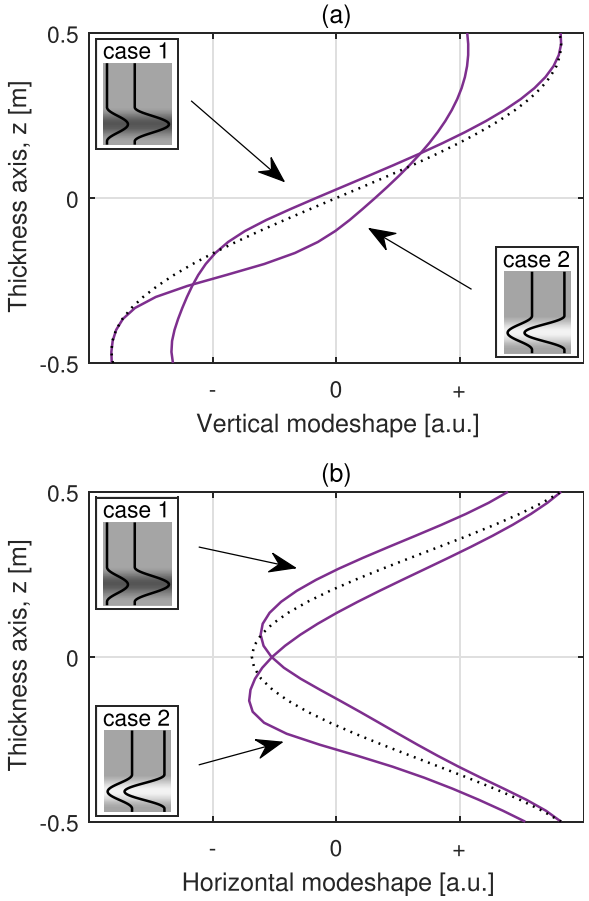

FIG. 4. (Color online) Displacement mode shape of the M4-ZGV mode for case 1 and case 2 (a) in the vertical direction and (b) in the horizontal direction. Dotted lines show S1-ZGV from the isotropic reference case.

is no strict symmetry around the midplane of the plate. The location of the neutral planes, in this case interpreted as the coordinate in the cross section with zero displacement magnitude, is also different for the two cases. For cases 1 and 2, the neutral planes are shifted toward the top surface ($z = h/2$) and bottom surface ($z = -h/2$) of the plate, respectively. Nonetheless, it can be concluded that the overall characteristic is roughly the same for the M4-ZGV mode as for the S1-ZGV Lamb mode, and loosely speaking, the M4-ZGV mode shape for both cases may be approximately symmetric. To summarize, for both cases, the M4-ZGV mode and the S1-ZGV Lamb mode both have a mode shape that persists throughout the entire plate thickness. This means that the mode may represent the entire thickness, in contrast to Rayleigh type of waves that only reflect the localized properties of the surface. In addition, the stationary nature of ZGV modes imply that estimations are locally representative in the lateral plane of the plate, since they are not influenced by any lateral propagation path.

Although the general pattern of the dispersion curves for case 1 and 2 and the isotropic reference case have apparent similarities, the behavior of an isotropic plate cannot always be extrapolated to cases such as case 1 and 2. For instance, by studying the M4 mode shape for increasing wave number k in a region close to the M4-ZGV point, it can be observed

that the M4 mode shape characteristic for both cases 1 and 2 changes from approximately symmetric to approximately antisymmetric close to the M4-ZGV mode frequency. The opposite holds for the M3 mode, which evolves from approximately antisymmetric to approximately symmetric for both cases 1 and 2. In other words, an interchange in characteristic mode shape between the M3 and M4 modes occurs in a region close to the M4-ZGV point. This type of interchange in mode behavior, sometimes referred to as mode kissing, is for both cases caused by the lack of symmetry around the midplane of the plate due to inhomogeneous material variation.

Traditionally, the group velocity of a wave mode is defined as the slope of the dispersion curve, i.e., $V_g = df/dk$. However, obtaining a stable continuous differentiation of the dispersion curves with respect to wave number may occasionally become difficult due to the discrete nature of the numerical solution. An alternative approach, adopted in this study, is to calculate the so-called energy velocity of the wave mode, since these two quantities are coincident for plates without material attenuation.[52] Using this approach, the group velocity (energy velocity) is determined from $V_e = P/E_{\text{tot}}$, where P is the one-period time and cross-section-averaged Poynting vector component in the propagation direction of the mode, and E_{tot} is the one-period time and cross-section-averaged total (kinetic and potential) energy of the wave mode.[46] Figures 5(a) and 5(b) show the group velocity (energy velocity) of the M1–M4 modes for case 1 and case 2, respectively. The group velocity (energy velocity) of the four lowest Lamb modes for the isotropic references case is also shown for comparison. For both case 1 and case 2, the M4-ZGV mode materializes in a similar manner as for the isotropic case. The shift in frequency for the M4-ZGV mode, in terms of a horizontal translation of the M4 curve compared to the isotropic reference case, is also clearly visible for both cases.

The excitability of the four lowest M1–M4 modes for case 1 and case 2 is displayed in Figs. 6(a) and 6(b), respectively. The excitability of the four lowest Lamb modes for the isotropic reference case is shown for reference. Similar to that in Fig. 5, a general shift in frequency, revealed as a horizontal translation of the M4 excitability curve, can be observed in Fig. 6 for both cases. Here, note that the excitability is interpreted as the displacement magnitude at the top surface of the plate in the surface normal direction, caused by a unit point load applied at the same point and direction. More specifically, excitability is calculated according to $E = i\omega|U|^2/(4P)$, where ω is the angular frequency, U is the surface normal displacement at the top surface of the plate, and P is the one-period time and cross-section-averaged Poynting vector component in the propagation direction of the mode.[53] Figure 6 shows that the M4 curves for both case 1 and case 2 exhibit high values of excitability around the M4-ZGV mode frequency. Accordingly, these results suggest that high displacement amplitudes, in the form of a local resonance of the plate, are to be expected at the top plate surface even in these two cases subjected to continuous inhomogeneous material variations. For this reason, the robustness and detectability

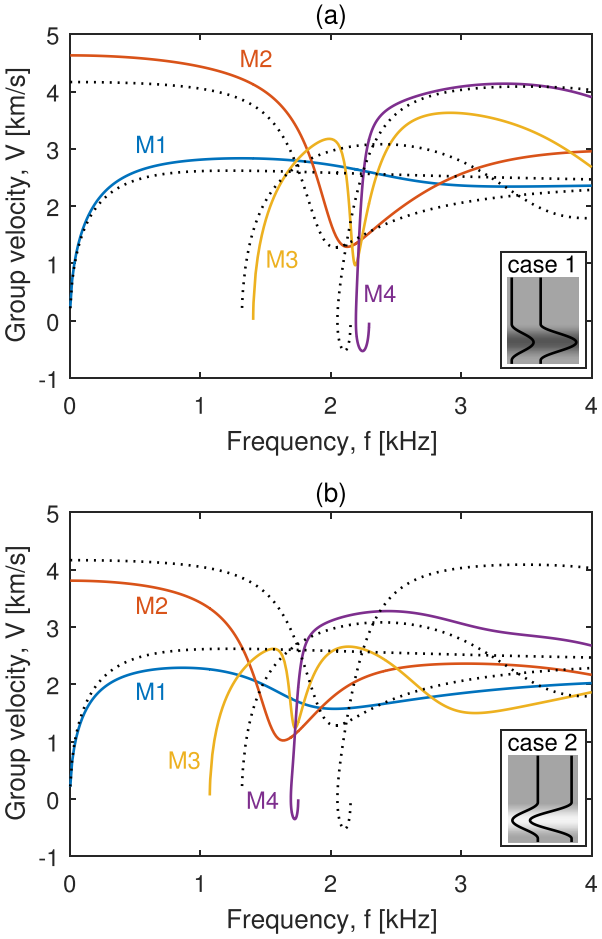

FIG. 5. (Color online) Group velocity for (a) case 1 and (b) case 2. Dotted lines show isotropic reference case.

of the M4-ZGV mode frequency in a nondestructive application is studied using a simulation, as discussed in Sec. IV.

IV. SIMULATION OF MEASUREMENT APPLICATION

A. Description of application

Similar to the S1-ZGV Lamb mode for the isotropic reference case, results from the SAFE analysis in Sec. III suggest that high displacement amplitudes at the top plate surface are expected at the M4-ZGV mode frequency for case 1 and case 2. This predicted behavior is simulated in an application corresponding to a nondestructive measurement and evaluation technique; furthermore, simulation results can be used to verify the results from the SAFE analysis. Considering the original motive for case 1 and case 2, the application is selected to represent a measurement of plate-like concrete structures.[26,39] In this type of measurement, an accelerometer is attached to the top plate surface. Then, the vibration response from hammer impacts, performed at an increasing offset distance from the accelerometer, is recorded. Since the hammer also works as a triggering device, reciprocity is used to create a multi-signal recording of a full wave field response from a single-point source excitation. In fact, such a multi-signal recording representing a

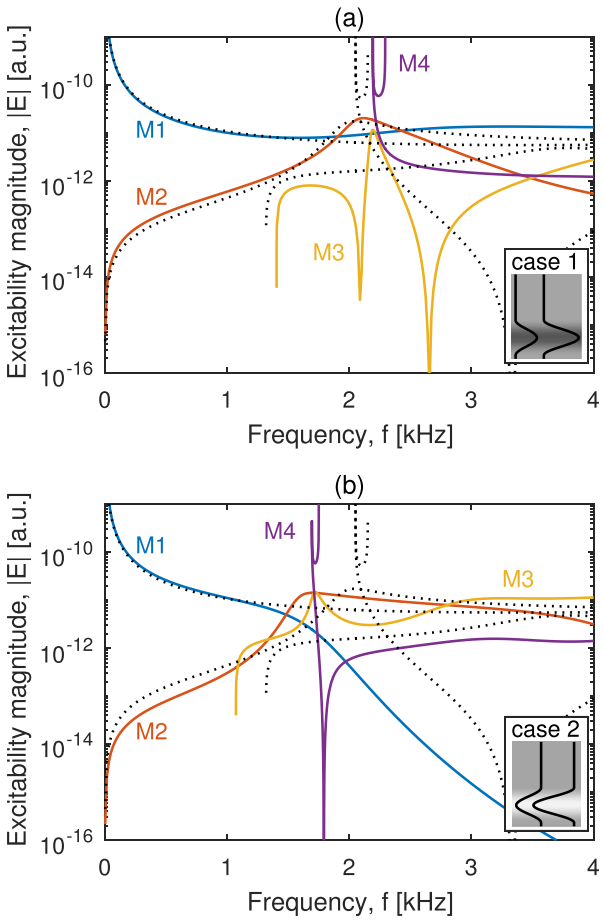

FIG. 6. (Color online) Excitability for (a) case 1 and (b) case 2. Dotted lines show isotropic reference case.

very general type of data set can be found in a number of applications.

B. Model and analysis

A two dimensional (2D) conventional FE model created in a commercial code[47] is used to study cases 1 and 2 and the isotropic reference case. The cases are modeled as a 10 m long plate with an axial symmetry condition that enables a point source excitation from a hammer impact. At the farther end of the plate, away from the axial symmetry axis and point source excitation, an absorbing region is added to reduce reflections from the plate end boundary.[54] This allows a finite approximation of the infinite lateral (radial) dimension according to the case definition to be obtained. In addition to the absorbing region and the geometrical damping caused by the axial symmetry condition, material damping is also introduced by a loss factor $\eta = 0.02$. The point source excitation is applied as a Gaussian mono-pulse with a center frequency corresponding to the S1-ZGV Lamb mode frequency; a broadband excitation, similar to that from a hammer impact, is obtained. Then, synthetic data sets represented by the time-domain acceleration response of the top plate surface are determined from the inverse Fourier transform of the model response in frequency domain.[55]

The acceleration response as function of time at different radial offset distances to the hammer impact for cases 1 and 2 are shown in Figs. 7(a) and 7(c), respectively. These figures show an expanded view of the data sets within a time range 0–5 ms and a radial offset distance range 0–2 m for cases 1 and 2, respectively. Here, the radial coordinate $r = 0$ m corresponds to the impact location. To estimate the wave number-

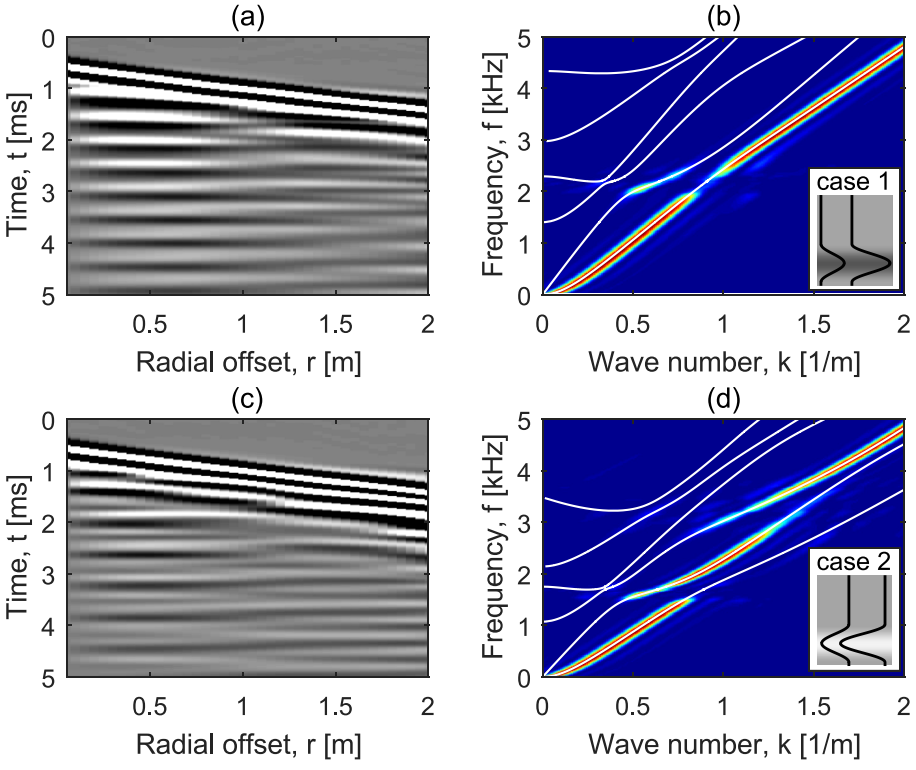

FIG. 7. (Color online) Data sets for (a) case 1 and (c) case 2. Estimation of wave number-frequency content for (b) case 1 and (d) case 2 and superimposed dispersion curves (solid lines) from SAFE analysis.

frequency content of the simulated response, a 2D discrete Fourier transform (DFT)[56] is performed with results for cases 1 and 2 displayed in Figs. 7(b) and 7(d), respectively. Here, it should be noted that the full range of the data sets is used to construct the DFT image; the full data set covers the time range 0–40 ms and radial range 0–10 m. In addition to the wave number-frequency estimation, the dispersion curves from the SAFE analysis in Sec. III are superimposed and shown in Figs. 7(b) and 7(d). For both cases, good agreement between the dispersion curves and the data set is observed; this result further verifies the correctness of the dispersion curves from the SAFE analysis. By comparing case 1 in Fig. 7(b) with case 2 in Fig. 7(d), a differentiation of surface wave mode at high frequency is observed: the surface wave is related to the M1 mode for case 1 and to the M3 mode for case 2. This result, due to the regions near the top and bottom surfaces being exposed to different mechanical properties, can also be observed by studying the mode excitability in Fig. 6. Naturally, in investigations of an unknown system, such behavior may—if not considered—lead to uncertainty and error in data evaluation.

To facilitate identification of the M4-ZGV mode frequency, the response signals within a radial distance of 1 m from the point source are summed.[29] As a result, the influence from the propagating modes is reduced, which is useful for improved detection of the ZGV frequency in practical testing. Note that other summation regions (radial distances) can be used as well; the radial distance may, for instance, be adjusted depending on plate thickness or anticipated ZGV wave length. A discrete Fourier transform of the summed signal is calculated and shown with absolute values in Fig. 8. For reference, the ZGV frequencies from the SAFE analysis are marked with vertical lines. Good agreement can be observed for all cases.

As predicted from the SAFE analysis, the M4-ZGV mode materializes as a resonance with high amplitude and distinct frequency, similar to the S1-ZGV Lamb mode. However, the acceleration amplitudes of the peaks differ slightly between the cases. This is related to at least two different effects. First, for a constant absolute displacement amplitude $|C|$ in frequency domain, the corresponding absolute acceleration amplitude is given by a quadratic parabola $|C|f^2$, see Fig. 8. This effect, which occurs because acceleration is given by a second temporal derivative of displacement, causes increased acceleration amplitudes at high frequencies and decreased amplitudes at low frequencies for a constant displacement amplitude in frequency domain. Second, the amplitude of the M4-ZGV mode shape is different between the top and bottom surfaces (Fig. 4). For case 1, the M4-ZGV mode has a vertical displacement amplitude at the top surface that is higher than that at the bottom surface, whereas the opposite holds for case 2. Nevertheless, it is concluded that the frequency of the peaks corresponding to the M4-ZGV mode is detected with the same robustness and accuracy as for the S1-ZGV Lamb mode in the studied nondestructive application. That is, a practical nondestructive evaluation using ZGV modes can be used even for cases 1 and 2. It is reasonable to assume that this result can be further extended and generalized to other inhomogeneous plates that are within the boundary limits or similar to cases 1 and 2. However, due to the increased complexity of the relation between mode frequency and material properties in inhomogeneous cases, the evaluation and interpretation of the observed frequency may be difficult. This emphasizes the need for a secondary and independent investigation to assess any potential influence from varying material properties.

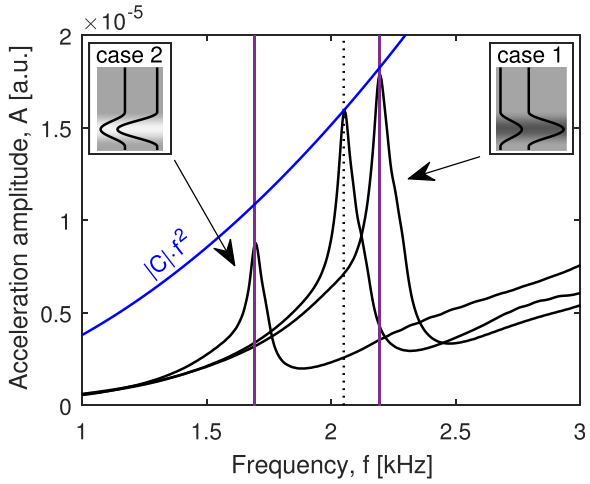

FIG. 8. (Color online) Discrete Fourier transform of summed acceleration response signals within 1 m distance from the impact source for case 1, case 2, and the isotropic reference case. Observed peaks correspond to the M4-ZGV mode (left and right peaks) and the S1-ZGV mode (middle peak). Vertical lines mark the ZGV frequencies from SAFE analysis. Parabola shows acceleration amplitude values corresponding to a constant absolute displacement amplitude $|C|$ at different frequencies.

V. CONCLUSION

Results from the SAFE analysis show that the M4 mode for both cases 1 and 2 exhibit a ZGV mode (M4-ZGV) that is similar to the S1 Lamb mode (S1-ZGV) for the isotropic reference case. Some differences in mode shape between M4-ZGV and S1-ZGV are observed, although it can be concluded that the overall characteristic of the M4-ZGV mode shape is common and similar to the S1-ZGV mode shape. No strict symmetric or antisymmetric modes exist for case 1 and case 2; however, one may loosely describe the M4-ZGV mode as approximately symmetric.

The SAFE analysis shows high mode excitability associated with the M4-ZGV mode. This is further verified in the simulation of a measurement application, as the M4-ZGV mode frequency is detected with the same accuracy and robustness as the S1-ZGV Lamb mode frequency. However, since a complex relation between mode frequency and material properties exists, the mode frequency cannot easily be translated to a representative mean value or other similarly established quantitative measure; thus, uncertainties or errors may arise in practical measurement applications.

A challenge with inhomogeneous material variation cases is the presence of a more complex wave field system. For cases 1 and 2, this can be observed, for instance, by the interchange of mode behavior, i.e., the so-called mode-kissing, as well as by the difference in the propagating surface wave mode at high frequency. For these cases, it is evident

that an assumption of homogeneous isotropy material (Lamb waves) is not feasible and cannot be considered as a robust mean value operator; an estimation using a Lamb wave model will not provide representative cross-sectional mean values for the plate in cases 1 and 2. Although this reasoning derives from a study of two synthetic cases, depending on the magnitude of the potential material variation, the same reasoning will hold for other inhomogeneous structures and applications as well.

To enable reliable evaluation procedures in practical nondestructive applications, results from this study highlight the general need for knowledge and understanding of the investigated system as well for assessment of the potential influence from varying material properties. The results also provide increased knowledge of ZGV modes and pave the way toward further improvements of nondestructive applications of plates, such as thick plate-like concrete structures in which material variations may occur.

ACKNOWLEDGMENTS

The Development Fund of the Swedish Construction Industry (SBUF, No. 13104) and The Swedish Radiation Safety Authority (SSM, No. SSM2017-956) are acknowledged for financial support of the study.

[1]C. Prada, D. Clorennec, and D. Royer, "Local vibration of an elastic plate and zero-group velocity Lamb modes," J. Acoust. Soc. Am. **124**(1), 203–212 (2008).
[2]E. Kausel, "Number and location of zero-group-velocity modes," J. Acoust. Soc. Am. **131**(5), 3601–3610 (2012).
[3]B. A. Auld, *Acoustic Fields and Waves in Solids, Vol. II*, 2nd ed. (Robert E. Krieger Publishing Company, Malabar, Florida, 1990).
[4]S. D. Holland and D. E. Chimenti, "Air-coupled acoustic imaging with zero-group-velocity Lamb modes," Appl. Phys. Lett. **83**(13), 2704–2706 (2003).
[5]I. Tolstoy and E. Usdin, "Wave propagation in elastic plates: Low and high mode dispersion," J. Acoust. Soc. Am. **29**(1), 37–42 (1957).
[6]C. Prada, O. Balogun, and T. W. Murray, "Laser-based ultrasonic generation and detection of zero-group velocity Lamb waves in thin plates," Appl. Phys. Lett. **87**(19), 194109 (2005).
[7]O. Baggens and N. Ryden, "Poisson's ratio from polarization of acoustic zero-group velocity Lamb mode," J. Acoust. Soc. Am. **138**(1), EL88–EL92 (2015).
[8]D. Clorennec, C. Prada, and D. Royer, "Local and noncontact measurements of bulk acoustic wave velocities in thin isotropic plates and shells using zero group velocity Lamb modes," J. Appl. Phys. **101**(3), 034908 (2007).
[9]C. Prada, D. Clorennec, T. W. Murray, and D. Royer, "Influence of the anisotropy on zero-group velocity Lamb modes," J. Acoust. Soc. Am. **126**(2), 620–625 (2009).
[10]M. Cès, D. Royer, and C. Prada, "Characterization of mechanical properties of a hollow cylinder with zero group velocity Lamb modes," J. Acoust. Soc. Am. **132**(1), 180–185 (2012).
[11]J. Laurent, D. Royer, T. Hussain, F. Ahmad, and C. Prada, "Laser induced zero-group velocity resonances in transversely isotropic cylinder," J. Acoust. Soc. Am. **137**(6), 3325–3334 (2015).
[12]S. Mezil, F. Bruno, S. Raetz, J. Laurent, D. Royer, and C. Prada, "Investigation of interfacial stiffnesses of a tri-layer using zero-group velocity Lamb modes," J. Acoust. Soc. Am. **138**(5), 3202–3209 (2015).
[13]S. Mezil, J. Laurent, D. Royer, and C. Prada, "Non contact probing of interfacial stiffnesses between two plates by zero-group velocity Lamb modes," Appl. Phys, Lett. **105**(2), 021605 (2014).
[14]M. Cès, D. Clorennec, D. Royer, and C. Prada, "Thin layer thickness measurements by zero group velocity Lamb mode resonances," Rev. Sci. Instrum. **82**(11), 114902 (2011).
[15]S. Raetz, J. Laurent, T. Dehoux, D. Royer, B. Audoin, and C. Prada, "Effect of refracted light distribution on the photoelastic generation of zero-group velocity Lamb modes in optically low-absorbing plates," J. Acoust. Soc. Am. **138**(6), 3522–3530 (2015).
[16]H. Bjurström and N. Ryden, "Detecting the thickness mode frequency in a concrete plate using backward wave propagation," J. Acoust. Soc. Am. **139**(2), 649–657 (2016).
[17]X. Dai, J. Zhu, Y.-T. Tsai, and M. R. Haberman, "Use of parabolic reflector to amplify in-air signals generated during impact-echo testing," J. Acoust. Soc. Am. **130**(4), EL167–EL172 (2011).
[18]J. Zhu and J. S. Popovics, "Imaging concrete structures using air-coupled impact-echo," J. Eng. Mechan. **133**(6), 628–640 (2007).
[19]B. Gérardin, J. Laurent, C. Prada, and A. Aubry, "Negative reflection of Lamb waves at a free edge: Tunable focusing and mimicking phase conjugation," J. Acoust. Soc. Am. **140**(1), 591–600 (2016).
[20]I. A. Veres, C. Grünsteidl, D. M. Stobbe, and T. W. Murray, "Broad-angle negative reflection and focusing of elastic waves from a plate edge," Phys. Rev. B **93**(17), 174304 (2016).
[21]F. Bruno, J. Laurent, P. Jehanno, D. Royer, and C. Prada, "Laser beam shaping for enhanced zero-group velocity Lamb modes generation," J. Acoust. Soc. Am. **140**(4), 2829–2838 (2016).
[22]F. Faëse, S. Raetz, N. Chigarev, C. Mechri, J. Blondeau, B. Campagne, V. E. Gusev, and V. Tournat, "Beam shaping to enhance zero group velocity Lamb mode generation in a composite plate and nondestructive testing application," NDT & E Int. **85**, 13–19 (2017).
[23]C. M. Grünsteidl, I. A. Veres, and T. W. Murray, "Experimental and numerical study of the excitability of zero group velocity Lamb waves by laser-ultrasound," J. Acoust. Soc. Am. **138**(1), 242–250 (2015).
[24]M. J. Sansalone and W. B. Streett, *Impact-echo: Non-destructive Evaluation of Concrete and Masonry* (Bullbrier Press, Ithaca, New York, 1997).
[25]A. Gibson and J. S. Popovics, "Lamb wave basis for impact-echo method analysis," J. Eng. Mech. **131**(4), 438–443 (2005).
[26]N. Ryden and C. B. Park, "A combined multichannel impact echo and surface wave analysis scheme for non-destructive thickness and stiffness evaluation of concrete slabs," *AS NT, 2006 NDE Conference on Civil Engineering* (2006), St. Louis, MO, pp. 247–253.
[27]R. Groschup and C. Grosse, "Mems microphone array sensor for air-coupled impact-echo," Sensors **15**(7), 14932–14945 (2015).
[28]R. Medina and M. Garrido, "Improving impact-echo method by using cross-spectral density," J. Sound Vib. **304**(3-5), 769–778 (2007).
[29]N. Ryden, "Enhanced impact echo frequency peak by time domain summation of signals with different source receiver spacing," Smart Struct. Syst. **17**(1), 59–72 (2016).
[30]M. S. Bouhdima, M. Zagrouba, and M. H. Ben Ghozlen, "The power series technique and detection of zero-group velocity Lamb waves in a functionally graded material plate," Can. J. Phys. **164**(2), 159–164 (2012).
[31]O. Abraham, B. Piwakowski, G. Villain, and O. Durand, "Non-contact, automated surface wave measurements for the mechanical characterisation of concrete," Constr. Build. Mater. **37**, 904–915 (2012).
[32]A. J. Boyd and C. C. Ferraro, "Effect of curing and deterioration on stress wave velocities in concrete," J. Mater. Civ. Eng. **April**, 153–158 (2005).
[33]J. S. Popovics, G. P. Cetrangolo, and N. D. Jackson, "Experimental investigation of impact-echo method for concrete slab thickness measurement," J. Kor. Soc. Nondestruct. Test. **26**(6), 427–439 (2006).
[34]J. S. Popovics, W. Song, J. D. Achenbach, J. H. Lee, and R. F. Andre, "One-sided stress wave velocity measurement in concrete," J. Eng. Mech. **124**(12), 1346–1353 (1998).
[35]S. Popovics, "Effects of uneven moisture distribution on the strength of and wave velocity in concrete," Ultrasonics **43**(6), 429–434 (2005).
[36]L. Qixian and J. H. Bungey, "Using compression wave ultrasonic transducers to measure the velocity of surface waves and hence determine dynamic modulus of elasticity for concrete," Constr. Build. Mater. **10**(4), 237–242 (1996).
[37]P. Turgut and O. F. Kucuk, "Comparative relationships of direct, indirect, and semi-direct ultrasonic pulse velocity measurements in concrete," Russ. J. Nondestr. Test. **42**(11), 745–751 (2006).
[38]A. M. Neville and J. J. Brooks, *Concrete Technology*, 2nd ed. (Prentice-Hall, Harlow, England), pp. 1–442 (2010).
[39]O. Baggens and N. Ryden, "Systematic errors in impact-echo thickness estimation due to near field effects," NDT & E Int. **69**, 16–27 (2015).
[40]O. Baggens and N. Ryden, "Near field effects and estimation of Poisson's ratio in impact-echo thickness testing," 41st Annu. Rev. Progr. Quantitative Nondestr. Eval. **1650**, 1415–1422 (2015).
[41]Alexander Gibson, "Advances in nondestructive testing of concrete pavements," Ph.D. thesis, University of Illinois, 2004.

[42]M. Cees, D. Clorennec, D. Royer, and C. Prada, "Edge resonance and zero group velocity Lamb modes in a free elastic plate," J. Acoust. Soc. Am. **130**(2), 689–694 (2011).
[43]H. Lamb, "On the flexure of an elastic plate," Proc. London Math. Soc. **s1-21**(1), 70–91 (1889).
[44]L. Rayleigh, "On the free vibrations of an infinite plate of homogeneous isotropic elastic matter," Proc. London Math. Soc. **20**(357), 225–234 (1889).
[45]M. J. S. Lowe, "Matrix techniques for modeling ultrasonic waves in multilayered media," IEEE Trans. Ultrason., Ferroelectr. Freq. Control **42**(4), 525–542 (1995).
[46]I. Bartoli, A. Marzani, F. L. di Scalea, and E. Viola, "Modeling wave propagation in damped waveguides of arbitrary cross-section," J. Sound Vib. **295**(3–5), 685–707 (2006).
[47]COMSOL Inc. Comsol multiphysics (r), 2016, URL http://www.comsol.-com (Date last viewed 2016-12-20).
[48]M. V. Predoi, M. Castaings, B. Hosten, and C. Bacon, "Wave propagation along transversely periodic structures," J. Acoust. Soc. Am. **121**, 1935–1944 (2007). ISSN 00014966.
[49]Q. Zhu and W. G. Mayer, "On the crossing points of Lamb wave velocity dispersion curves," J. Acoust. Soc. Am. **93**(4), 1893–1895 (1993).
[50]A. G. Every, "Intersections of the Lamb mode dispersion curves of free isotropic plates," J. Acoust. Soc. Am. **139**(4), 1793–1798 (2016).
[51]H. Uberall, B. Hosten, and M. Deschamps, "Repulsion of phase-velocity dispersion curves and the nature of plate vibrations," J. Acoust. Soc. Am. **96**(2), 908–917 (1994).
[52]M. Biot, "General theorems on the equivalence of group velocity and energy transport," Phys. Rev. **105**(4), 1129–1137 (1957).
[53]F. Treyssède and L. Laguerre, "Numerical and analytical calculation of modal excitability for elastic wave generation in lossy waveguides," J. Acoust. Soc. Am. **133**, 3827–3837 (2013).
[54]W. Ke, M. Castaings, and C. Bacon, "3d finite element simulations of an air-coupled ultrasonic NDT system," NDT & E Int. **42**(6), 524–533 (2009).
[55]M. Castaings, C. Bacon, B. Hosten, and M. V. Predoi, "Finite element predictions for the dynamic response of thermo-viscoelastic material structures," J. Acoust. Soc. Am. **115**(3), 1125–1133 (2004).
[56]C. B. Park, R. D. Miller, and J. Xia, "Multichannel analysis of surface waves," Geophysics **64**(3), 800–808 (1999).

Build version ☼2017-08-30 ◷13.12.45
(end of document)